Fabrication and transport properties of graphene-based nanostructures

Submitted by Roman V. Gorbachev to the University of Exeter as a thesis for the degree of Doctor of Philosophy in Physics
June, 2009

This thesis is available for Library use on the understanding that it is copyright material and that no quotation from the thesis may be published without proper acknowledgement.

I certify that all material in this thesis which is not my own work has been identified and that no material has previously been submitted and approved for the award of a degree by this or any other University.

Roman V. Gorbachev
June, 2009

Abstract

In this work fabrication and studies of transistor structures based on an atomic sheet of graphite, graphene, are described. Since graphene technology is in its early stages, the development and optimisation of the fabrication process are very important. In this work the impact of various fabrication conditions on the quality of graphene devices is investigated, in particular the effects on the carrier mobility of the details of the mechanical exfoliation procedure, such as environmental conditions and humidity, source of graphite and wafer cleaning procedure. In addition, a comparison is made between the conventional e-beam lithorgaphy and lithography-free fabrication of samples. It was also demonstrated that water and other environmental species play an important role in graphene-to-substrate adhesion and can also contribute to the carrier scattering in graphene.

A technique for creating suspended metal gates was developed for the fabrication of graphene p-n-p structures, and charge transport has been studied in such top-gated graphene devices. Depending on the relation between the carrier mean free path and the length of the top-gate we have realized three distinct transport regimes through the p-n-p structure: a) diffusive across the structure; b) ballistic in the regions of p-n junctions but diffusive in the n-region; c) ballistic across the whole p-n-p structure. The second regime has revealed the chiral nature of carriers in graphene. This was demonstrated by comparing the experimental resistance of a single p-n junction with results of electrostatic modeling in the diffusive model. In the third regime we have observed oscillations of the device resistance as a function of carrier concentration in the n-region, which are also dependent on magnetic field. These oscillations have been demonstrated to be a direct consequence of a Fabri-Perot-like interference effect in the graphene p-n-p structures.

Acknowledgements

I would like to express my gratitude to many people who helped me during the period of my PhD studies.

First of all, I am very grateful to my supervisor Prof. Alex Savchenko for his encouragement and support throughout these years. Special thanks goes to Andrew Kretinin and Dave Horsell for sharing their knowledge and experimental experience. It was priceless and much appreciated.

I would like to thank other PhD students: Fedor Tikhonenko and Sasha Mayorov for the assistance they provided at all levels of the research, Adam Price for helping me to improve my English skills, Alexey Kaverzin and Alexey Kozikov to whom I was lucky to work with.

I must also acknowledge all the technical support in the Physics Department. Some things would never have been possible without the help of Paul Wilkins, Stephen Tuckett, Kevin White, Peter Cann, Matthew Wears and Phil Slade. Dave Manning and Adam Woodgate did a great job making sure the supply of liquid helium never stopped. The Stores never ceased to be a treasury full of useful things thanks to John Meakin. I would also like to thank the office staff for all the times their assistance helped me along the way.

Separate thanks to Massimo Gludini for sharing his knowledge of SPM, Kostya Novoselov (Manchester University) for very useful discussions about graphene, Geb Jones and David Anderson (Cavendish Laboratory) for the communication concerning e-beam lithography.

My PhD studies would not have been possible without the financial assistance of the Overseas Research Student Award Scheme and the University of Exeter, and I express my gratitude to them.

I would like to thank my friends George Zorinyants and Tatyana Voronina, Fedor and Natasha Ogrin, Alexander Beloglazov, Andrey Kondratyuk, Olga Mihal'chenko, Sergey Levin and, especially, Julia Lalina for supporting me and having fun together.

And last but not least, I would also like to thank my family for the opportunity to have a good education and support they provided me through all the years of my study.

Contents

Abstract **2**

Acknowledgements **3**

Contents **4**

List of Figures **8**

List of Tables **15**

Introduction **16**

1 Basic theoretical concepts of graphene **18**

1.1 Graphene dispersion relation. Tight binding approximation 18

1.2 Low energy approximation. Dirac Hamiltonian. Berry phase 22

1.3 Chirality, DOS 26

1.4 Transistor structure: graphene on n-Si/SiO_2 28

1.5 Carrier scattering in graphene on SiO_2 29

1.6 Conclusion 31

2 Experimental methods of graphene fabrication **32**

2.1 Introduction 32

2.2 Wafers for graphene deposition 34

2.2.1 General information 34

2.2.2 Cleaning methods 35

2.2.3 Surface topography 36

2.2.4 Water on SiO_2 37

2.3 Graphite 39

2.3.1 General information 39
2.3.2 Adhesion to graphite surface 41
2.4 Conventional graphene deposition 43
2.5 Environmental graphene deposition 44
2.6 Thin flakes search and identification 46
2.7 AFM study of graphene and its environment 47
2.7.1 Introduction 47
2.7.2 Step height measurements 48
2.7.3 Morphology of graphene on silica 50
2.7.4 Effect of high electric field on SiO_2 wafers 51
2.7.5 Contamination induced by electric field 53
2.7.6 Contamination after fabrication and annealing 54
2.8 Conclusion 57

3 Device Fabrication 58

3.1 Introduction 58
3.2 Electron Beam Lithography 59
3.3 Elphy quantum. Exposure logistics 61
3.4 Spatial energy distribution. Proximity effect. 63
3.5 E-beam resists 65
3.6 Multilayer resist. Development 68
3.7 Metalization. Undercut profile. Lift-off 69
3.8 Packaging and bonding 72
3.9 “Old” fabrication route 73
3.10 “New” fabrication route 74
3.11 Example of graphene Hall-bar fabrication 75
3.12 Shaping graphene flakes 80
3.13 Samples storage and handling 81
3.14 Flake suspension and further technology development 83
3.15 Summary 84

4 Transport in graphene flakes 86

4.1 Introduction 86
4.2 Experimental setup 86

4.3 Basic characterisation 87
4.4 Annealing and Doping
Samples Statistics 89
4.5 Review of scattering mechanisms 92
4.6 Temperature dependencies of the conductivity: experimental results . 95
4.7 Transport in high magnetic field 96
4.7.1 Specifics of high B behaviour in graphene 96
4.7.2 Experimental observation of resistance in high B 97
4.8 Weak Localisation 100
4.9 Conclusion 101

5 Suspended bridge fabrication 102
5.1 Introduction 102
5.2 General technique 103
5.3 EBL and resist 104
5.3.1 Focusing and exposure 104
5.3.2 Resist intermixing 105
5.4 Undercut profile and dose selection 106
5.5 Way forward 109
5.6 Conclusion 111

6 Transport in top-gated structures 112
6.1 Transmission through a single p-n junction 112
6.2 Characteristic lengths of a p-n-p structure, effects of disorder 115
6.3 Experimental results: overview 117
6.4 Electrostatic modeling 119
6.5 Diffusive and ballistic regimes of a single p-n interface 121
6.6 Fully ballistic regime of the p-n-p structure 124
6.7 Transport through p-n-p structure in magnetic field 128
6.8 Conclusion 131

7 Further developments and suggestions 132

Bibliography 134

A Inserts **141**

List of Figures

1.1 Graphene honeycomb crystal lattice. (a) Two independent sublattices are shown with different colour, yellow rhombus is the primitive cell. (b) Graphene lattice in the reciprocal space, yellow fill shows two possible selections of the Brillouin zone. 19

1.2 Band diagram of graphene in the nearest neighbours approximation according to relation 1.12. 22

1.3 Lines of the constant energy for the graphene dispersion relation 1.12. 23

1.4 Change from the hexagonal Brillouin zone to the diamond-shaped. . . 23

1.5 Illustration for the chirality in graphene – yellow and blue colours denote chirality of 1 and -1. 27

2.1 Different termination of the oxide surface. 34

2.2 TAFM surface image of silicon dioxide, 1 - roughness distribution and 2 - autocorrelation function for the given image. 37

2.3 Water H-bonded to silanol terminated SiO_2. 38

2.4 Dependence on the relative humidity of: water film thickness on SiO_2 by XPS study (left axis) and the surface potential measured by Kelvin-probe AFM (right axis) [32]. 38

2.5 Hexagonal graphite lattice arranged in Bernal $A\bar{B}$ stacking. 40

2.6 SEM image of natural graphite, scale bar 100 μm. 40

2.7 Micrometer size water droplets on graphite surface [36]. 41

2.8 Comparison of binding energies of molecules on graphite surface obtained from the friction experiments to other values in literature. From [41]. 42

2.9 Nitto adhesive tape (blue) with graphite flakes (black). 43

2.10 Chamber for environmental graphene deposition. 44

2.11 Density of deposited graphite as a function of relative humidity. . . . 45
2.12 Optical image of a multi-step flake under optical microscope, (a) with white light source, (b) green filtered. Scale bar is 20 μm. 1 and 2 denote single layer and bilayer parts. 47
2.13 Schematics of scanning probe microscope. 48
2.14 TAFM image of a folded graphene flake. Insets give the height profiles averaged over rectangular boxes 1 and 2, respectively. 49
2.15 TAFM image of a graphene flake. Number 1 denotes SiO_2, 2 – graphene single and 3 – triple-layer regions. 50
2.16 Flake manipulation using the AFM tip. (a) TAFM scan of the initial flake, b – folded flake, c – zoomed area indicated on image b. 52
2.17 Effect of local charging of silicon dioxide. Scale bar is 2 μm. 52
2.18 Topography of pristine flake (a), phase contrast image of contaminated (b) and heavily contaminated (c) flake. All images have the same scale and were acquired in the same region. 54
2.19 Topography of a pristine graphene flake on silica (left) and a sample which passed the conventional contact fabrication procedure (right). . 55
2.20 Effect of annealing on topography of graphene devices: (a) a sample annealed in helium at 150° C; (b) single line scan showed as the white dashed line in (a); (c) annealed in Ar/H_2 mixture at 400° C; (d) summary table for topography measurements. Scale bar is 1 μm. 56

3.1 Schematic of an electron beam microscope. 60
3.2 Pattern fragmentation before the exposure. Numbers shown default left-to-right exposure order. 61
3.3 Gaussian contribution from forward scattering (solid line) and backscattering (dashed dot line) for low (a) and high (b) beam energy. Proximity effect: initial pattern (c), actual dose distribution (d) and profile of developed resist (e). 64
3.4 Metal contacts to a graphene flake. Left - correct dose distribution and shape, right - distortion due to the proximity effect. Scale bar 1 μm. 64

3.5 Developed resist thickness plotted against exposure dose. Solid line is normal resist; dashed line is the same resist with higher molecular weight, short dashed – with broad distribution of molecular weights. . 66
3.6 Structure of PMMA polymer. 67
3.7 PMMA reaction under electron or UV irradiation. 68
3.8 Structure of the P(MMA-MAA) copolymer. 69
3.9 Illustration of the 'shadow' effect during metal evaporation using two sources. 71
3.10 Lift-off in the acetone distiller. 71
3.11 A piece of silicon wafer with a graphene sample glued and bonded to a package. 72
3.12 Back side of the package for the further electrical connections. 72
3.13 Standard technological route. Dotted block can be placed in any of two positions. 74
3.14 Second technological route. 75
3.15 Optical image of uncovered flake on 275 nm silicon dioxide surface (in white light). 77
3.16 Optical image of the flake covered with $\sim$ 100 nm PMMA layer and the 4 nearest crosses (green light). 77
3.17 Structure design superimposed on the optical image of a graphene flake. 78
3.18 Optical image of the developed contact pattern. 79
3.19 Optical image of the finished sample. 79
3.20 Plasma etching of graphene flakes: (a) initial optical image of a flake, (b) Hall-bar design (black lines), (c) final device after the etching and contacts fabrication. Scale bar is 2 μm. 81
3.21 SEM image of the sample damaged by ESD. 82
3.22 SEM image of the sample damaged by thermal shock. A split in the flake can be seen around the contact. 82
3.23 SEM image of (left side) suspended and (right side) collapsed parts of a graphene flake, tilt 45°. 84

4.1 Characterization of a graphene sample: a - resistivity (left scale, black) and conductivity (right scale, red) as a function of the carrier concentration, b - carrier mobility (left scale, black) and mean free path (right scale, red) as a function of the carrier concentration. . 88

4.2 (a) Effect of annealing on the $R(V_{\rm bg})$ dependence of single and bilayer graphene samples. Inset shows optical image of the sample. (b) Statistical results on the graphene mobilities plotted against peak values of the sheet resistance. Black circles denote standard fabrication technique, blue dots – flakes deposited in dry argon, red dots – lithography-free technique. 90

4.3 Lithography-free graphene device. Flake lenth is ∼20 μm. 91

4.4 (a) Conductance as a function of back-gate voltage for different temperatures, top black curve shows result of the linearization procedure. (b) Extracted values of $R_{\rm min}$ as a function of temperature. (c) Slope α as a function of temperature. Colours denote different samples. . . 95

4.5 Shubnikov-de Haas oscillations (a) and Hall effect (b) as a function of magnetic field for three different concentrations indicated as coloured dots on $R(V_{\rm bg})$ in the inset of (b). Temperature is 4 K, carrier mobility for the studied range on $V_{\rm bg}$ is $\mu = 12000$ cm^2/Vs. 98

4.6 Left axis: quantum lifetime as a function of the carrier concentration for different temperatures (corresponded data shown as symbols, see colour-code). Right axis: momentum relaxation time (refers to solid line) calculated from $R(V_{\rm bg})$. 99

4.7 R_{xx} as a function of B for $n = 1.5 \cdot 10^{12}$ cm^{-2}, $T = 50$ mK. The filling factor values are found from the position in B of centers of minima in R_{xx}. 99

4.8 The longitudinal (black and red, left axis) and transverse (green and blue, right axis) conductivity as a function of gate voltage, with $T =$ 5.6 K $B = 12.5$ T. 99

5.1 Stages of suspended gate fabrication: a – electron beam exposure, b,c – resist development, d – metalization and e – lift-off. 104

5.2 Contamination spot grown using 20 second point-like exposure. . . . 105

5.3 PMMA dissolution rates, taken from [99]. 106
5.4 Undercut profile for different resist configurations. Bilayer (a) (span) and triple layer (b) (pillar), (c) (span) resist techniques. 106
5.5 Developed resist thickness against the exposure dose for the two different resist layers. Red lines d_{span} and $d_{pillars}$ illustrate a correct exposure doses for the different regions of suspended bridge. 107
5.6 SEM image of three different bridges made with 45° tilt to the surface. Image (b) shows the optimal span dose, whilst (c) and (a) are overexposed and underexposed cases, respectively. 108
5.7 Bridge clearance as a function of the span dose. Three curves show 60, 75 and 150 nm wide patterns resulting in 90, 105 and 150 nm real span width, respectively. 108
5.8 Nanotube suspension: a nanotube embedded into resist (a), illustration for metal clamping (b). 110
5.9 MWCN manipulation on a graphene sample. Initial (a) and final (b) positions of the nanotube (highlighted with the green arrow) imaged with TAFM. 111

6.1 Illustration of chiral tunneling through a sharp p-n junction (see text).112
6.2 Tunneling through a smooth p-n junction. 113
6.3 Illustration for different transport regimes inside p-n-p structure: from (a) fully diffusive to (c) fully ballistic. 115
6.4 Oscillations in (a) transmission coefficient and (b) resistance as a function of the potential depth under the top gate from [104]. Inset shows scaling of the peak positions as a function of $n^{2/3}$, where n is the peak number. 117
6.5 Sample S2: (a) SEM image and (b) resistance in high magnetic field (see text) 118
6.6 Top-gate dependence of the resistance for different values of $V_{\rm bg} = V_{\rm bg}^{\rm off} + i[{\rm V}]$, where i = 1...9, from top to bottom. 119
6.7 Colour-scale plot of the resistance as a function of $V_{\rm tg}$ and $V_{\rm bg}$ (sample S1). Coloured arrows refer to the line sweeps in Fig.6.6. 119

6.8 Electrostatic modeling reported in [94]: (a) Geometry of top gated structure used in the calculations, (b,c,d) potential profile along the flakes S1,S2,S3 at fixed V_{bg} and different V_{tg}. Bold bars indicate the mean free path length. 120

6.9 (a) Resistivity of samples S1, S2 and S3 as a function of V_{bg}, at $T = 50$ K and $V_{\mathrm{tg}} = 0$. (b,c,d) The resistance of samples S1, S2 and S3, respectively, as a function of V_{tg} (values of V_{bg} shown as symbols in (a)). The empty circles show the result of the modeling assuming diffusive transport of carriers. 122

6.10 Resistance as a function of V_{tg} showing an oscillatory behaviour for a small values of l_{pnp} in the range of V_{tg} between 19 and 32 V. 124

6.11 The oscillations at 4.2 K: reproducibility test for a different mesoscopic realization, curves shifted by 0.5 kΩ. 124

6.12 Reproducibility test for the dependence shown in Fig.6.10. Black and red curves denote different sweep directions. 125

6.13 Temperature dependence of the oscillations. The curves are shifted by 0.5 kΩ. 125

6.14 Results of electrostatic modeling for sample S4: (a) potential profile along the flake calculated for different top-gate voltages; (b) dependence of l_{pnp} and the potential depth ε on the top-gate voltage; (c) the parabolic fit for the potential shape (see text). 127

6.15 Comparison of the observed peak positions (black dots) with the theoretically predicted values (red dots and line) [104]. 128

6.16 Shift of the oscillations in magnetic field: red curve $B = 0$, blue $B = 300$ mT. 129

6.17 Grey-scale plot of resistance as a function of V_{tg} and B showing a shift of the oscillations. 129

6.18 Magnetoresistance up to 1.5 T for three different regions on the R($\mathrm{V_{tg}}$). Solid lines are the weak localisation fits. 130

A.1 Modification done to Heliox VL criostat cold-finger. Allows quick and reliable connection of the sample packages to the cryostat wires. . . 141

A.2 Low temperature part of the experimental insert used for characterisation study of graphene samples and annealing in a transport dewar. 142
A.3 Environmental chamber for doping experiments. Insert with the sample nest, heater and environmental gauges (top) and a chamber body with transparent optical window, gas inlet and pumping port. 143

List of Tables

6.1 Summary of measured samples. 118

Introduction

The first experimental realisation of graphene transistor structures in 2004 created an explosion of theoretical and subsequently experimental activities in condensed matter physics. Graphene structures have a number of significant differences in their properties compared with conventional two dimensional systems: in optical, mechanical and, most importantly, electrical transport properties. The understanding of charge transport in graphene is important for fundamental physics, where solid state and relativistic physics overlap, as well as for possible applications in semiconductor technology.

The technology of graphene transistors is relatively new and under active development by different research groups. This work is dedicated to fabrication and experimental study of graphene-based devices. Particular attention is paid to the details of all stages of the fabrication process which might have an effect on the properties of the final product. It also describes the characterisation of graphene transistor structures, as well as experimental studies of charge transport through graphene p-n junctions.

Chapter 1 introduces some basic theoretical concepts needed to understand charge transport phenomena in graphene. Starting form the nearest neighbour approximation, it illustrates how the Dirac equation is related to graphene, and gives the explanation for such phenomena as being due to its peculiar density of quasiparticle states, the chirality of charge carriers and suppression of backscattering in graphene.

Chapter 2 describes the results of studies of graphene's environment, such as materials which are in contact with graphene, various atmospheric deposits, both on top of graphene and below it. It also discusses the contamination from the contact fabrication procedure and its removal by thermal annealing.

Chapter 3 discusses all stages of contact fabrication and ways to optimise it. Sample handling, problems of damage are discussed here, as well as some preliminary experiments on flake shaping and suspension.

Chapter 4 is dedicated to the electrical characterisation and transport studies of graphene Hall-bar structures. Statistical results on the quality of fabricated samples are presented.

Chapter 5 explains the details of the fabrication of suspended metal gates above graphene flakes. **Chapter 6** describes the results of transport measurements of top-gated devices. It shows that, depending on the ratio of characteristic sizes of the system, different regimes of charge transport through a graphene p-n-p structures can be realised. It shows that propagation of chiral carriers in graphene p-n-p structures is very different from the conventional p-n structure based on a two-dimensional electron gas.

Chapter 1

Basic theoretical concepts of graphene

1.1 Graphene dispersion relation. Tight binding approximation

The carbon atoms in graphene are sp^2 hybridized, so each forms three strong covalent σ bonds $(2s, 2p_x, 2p_y)$ with their nearest neighbour atoms. The remaining p_z orbitals are perpendicular to the plane and have a weak overlap, making charge transport possible. Therefore the following discussion will be about the electronic bands formed by the p_z-orbitals.

The honeycomb lattice can be described as two triangular sublattices Λ_1 and Λ_2, positioned as shown in Fig. 1.1. This lattice cannot be reproduced by copying one single atom using only two *translation* vectors. Therefore, the primitive cell contains two atoms (one from each sublattice) and can be selected as a yellow rhombus as shown in Fig.1.1. The vectors a_1, a_2 are two primitive translations,

$$\vec{a}_1 = a\left(\frac{\sqrt{3}}{2}, \frac{1}{2}\right), \ \ \vec{a}_2 = a\left(\frac{\sqrt{3}}{2}, -\frac{1}{2}\right), \tag{1.1}$$

where $a = \sqrt{3}a_{\text{bond}}$ is the lattice constant and a_{bond} the carbon-carbon bond length in graphene (approximately 1.42 Å [1]).

In reciprocal space the lattice is also hexagonal, and is rotated through 30° in plane with respect to the direct lattice. The following vectors can be used as a basis:

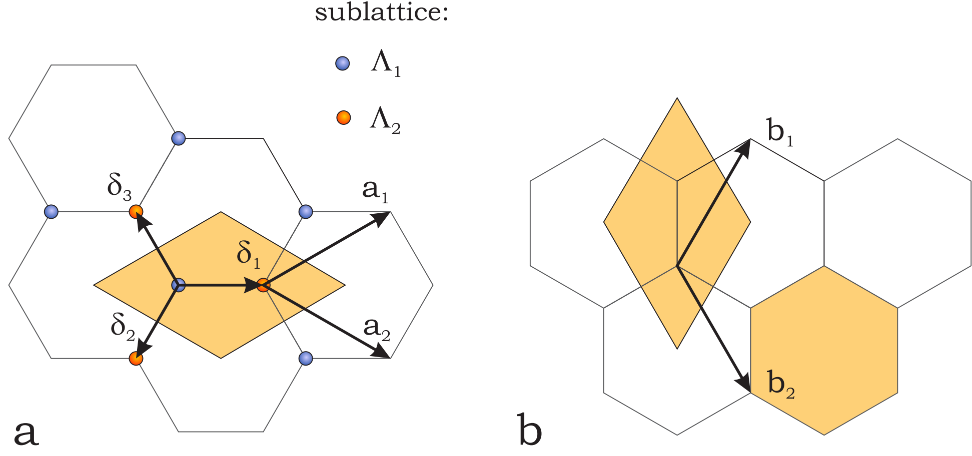

Figure 1.1: Graphene honeycomb crystal lattice. (a) Two independent sublattices are shown with different colour, yellow rhombus is the primitive cell. (b) Graphene lattice in the reciprocal space, yellow fill shows two possible selections of the Brillouin zone.

$$\vec{b}_1 = \frac{2\pi}{a}\left(\frac{1}{\sqrt{3}}, 1\right), \ \vec{b}_2 = \frac{2\pi}{a}\left(\frac{1}{\sqrt{3}}, -1\right). \tag{1.2}$$

Here $\vec{b}_1$, $\vec{b}_2$ satisfy the relation $\exp(i\vec{K}\vec{R}) = 1$, where $\vec{R} = k_1\vec{a}_1 + k_2\vec{a}_2$ and $\vec{K} = n_1\vec{b}_1 + n_2\vec{b}_2$ are the vectors of the normal and reciprocal lattices, respectively, and $k_{1,2}$, $n_{1,2}$ are integer numbers. Figure 1.1b shows the reciprocal lattice with two different primitive cells. The hexagonal type is commonly used as a Brillouin zone for symmetry reasons.

Any atom $\vec{r}_j$ in sublattice Λ_1 is connected with its nearest neighbours in Λ_2 by three vectors $\vec{\delta}_i$:

$$\vec{\delta}_1 = a\left(\frac{1}{\sqrt{3}}, 0\right); \quad \vec{\delta}_2 = a\left(-\frac{1}{2\sqrt{3}}, \frac{1}{2}\right); \quad \vec{\delta}_3 = a\left(-\frac{1}{2\sqrt{3}}, -\frac{1}{2}\right). \tag{1.3}$$

Written out in second quantization notation, the tight-binding Hamiltonian for the nearest neighbours takes the form [2]:

$$H = -t\sum_j\sum_{i=1}^{3} a^\dagger(\vec{r}_j)b(\vec{r}_j + \vec{\delta}_i) + c.c. \tag{1.4}$$

$$\left[a(r_i), a^\dagger(r_j)\right]_+ = \left[b(r_i), b^\dagger(r_j)\right]_+ = \delta_{ij}, \tag{1.5}$$

where $a, a^\dagger$ and $b, b^\dagger$ are creation and annihilation operators for sublattices Λ_1 and Λ_2 respectively, and follow the usual anticommutative relation for fermions (Eq.1.5); t

is the overlap integral, which sets the probability for an electron to jump from sublattice Λ_1 to sublattice Λ_2.

Let us write the Hamiltonian in Eq.1.4 in $\vec{k}$ space, using Fourier transforms of the operators:

$$H = -t\sum_j \sum_{i=1}^{3} \frac{1}{(2\pi)^2}\int_{BZ} e^{-i\vec{k}\vec{r}_j} a^\dagger(\vec{k}) d^2k \frac{1}{(2\pi)^2}\int_{BZ} e^{i\vec{k}'(\vec{r}_j+\vec{\delta}_i)} b(\vec{k}') d^2k' + c.c. =$$
$$= \frac{-t}{(2\pi)^4}\int_{BZ} a^\dagger(\vec{k}) d^2k \int_{BZ} b(\vec{k}') d^2k' \sum_j e^{i\vec{r}_j(\vec{k}'-\vec{k})} \sum_{i=1}^{3} e^{i\vec{k}'\vec{\delta}_i} + c.c.\,,$$

$$a(r_j) = \frac{1}{(2\pi)^2}\int_{BZ} e^{i\vec{k}\vec{r}_j} a(\vec{k}) d^2k,$$
$$b(r_j) = \frac{1}{(2\pi)^2}\int_{BZ} e^{i\vec{k}'\vec{r}_j} b(\vec{k}') d^2k'.$$

After using the relation $\sum_j e^{i\vec{r}_j(\vec{k}'-\vec{k})} = (2\pi)^2\delta(\vec{k}'-\vec{k})$ for $j \ni \Lambda_1$ and integrating over k' the resulting integral takes the following form:

$$H = \frac{-t}{(2\pi)^2}\int_{BZ}\left[a^\dagger(\vec{k}) b(\vec{k}) \sum_{i=1}^{3} e^{i\vec{k}\vec{\delta}_i} + b^\dagger(\vec{k}) a(\vec{k}) \sum_{i=1}^{3} e^{-i\vec{k}\vec{\delta}_i}\right] d^2k. \tag{1.6}$$

This view can be optimized using vector forms of the operators:

$$\varphi(\vec{k}) = \begin{pmatrix} a(\vec{k}) \\ b(\vec{k}) \end{pmatrix}; \quad \varphi^\dagger(\vec{k}) = \left(a^\dagger(\vec{k}),\, b^\dagger(\vec{k})\right) \tag{1.7}$$

$$H = \frac{-t}{(2\pi)^2}\int_{BZ}\left(a^\dagger(\vec{k}),\, b^\dagger(\vec{k})\right)\begin{pmatrix} 0 & \sum_{i=1}^{3} e^{i\vec{k}\vec{\delta}_i} \\ \sum_{i=1}^{3} e^{-i\vec{k}\vec{\delta}_i} & 0 \end{pmatrix}\begin{pmatrix} a(\vec{k}) \\ b(\vec{k}) \end{pmatrix} d^2k, \tag{1.8}$$

and, denoting the 2×2 matrix as $\tilde{H}$, a spinor representation of the Hamiltonian in k-space:

$$H = \frac{-t}{(2\pi)^2}\int_{BZ} \varphi^\dagger(\vec{k})\tilde{H}(\vec{k})\varphi(\vec{k}). \tag{1.9}$$

The nearest neighbour Hamiltonian is invariant under a number of discrete symmetries [2, 3]:

- Spatial inversion symmetry P: $(\vec{r}, a(\vec{r}), b(\vec{r})) \to (-\vec{r}, b(-\vec{r}), a(-\vec{r}))$ – inversion of the spacial coordinates and change of the atom type from one sublattice to another. This symmetry can be lifted if the particle densities on Λ_1 and Λ_2 are different, and in some cases it leads to the formation of a gap [4].
- Time inversion T: $t \to -t$ – does not change the coordinate sign, but inverts momentum and spin. Can be broken by applying a magnetic field.
- Particle-hole symmetry – antiparticle with the same momentum and spin has the same energy. This type of symmetry can be removed by taking into account next-nearest-neighbour interactions.

The dispersion relation $E(\vec{k})$ can be calculated as follows. For the time independent case, $H\psi = E\psi$, eigenvalues for this Hamiltonian can be expressed using the relation

$$\begin{vmatrix} E & t\sum_{i=1}^{3} e^{i\vec{k}\vec{\delta_i}} \\ t\sum_{i=1}^{3} e^{-i\vec{k}\vec{\delta_i}} & E \end{vmatrix} = 0. \tag{1.10}$$

Due to the fact that the honeycomb structure contains two atoms per unit cell, the spectrum of quasiparticles has two energy branches [5]:

$$E = \pm t\sqrt{\sum_{i=1}^{3} e^{i\vec{k}\vec{\delta_i}} \sum_{i=1}^{3} e^{-i\vec{k}\vec{\delta_i}}}. \tag{1.11}$$

Using values $\vec{\delta_i}$ from Eq.(1.3) the dispersion relation in the tight binding approximation for graphene is

$$E = \pm t\sqrt{1 + 4\cos\frac{k_y a}{2}\left(\cos\frac{\sqrt{3}k_x a}{2} + \cos\frac{k_y a}{2}\right)}. \tag{1.12}$$

Figure 1.2 plots relation 1.12. We see two symmetric bands: the valence band E_v (bottom surface) and conduction band E_c (top surface), which touch each other at 6 corners of the Brillouin zone when $E = 0$. Since each carbon atom has one π electron and two available spin projections, only half of the total number of states are occupied. Thus, in the absence of external electric charges and for zero temperature, the Fermi level lies at $E = 0$. The maximum energy at $k = 0$ can be estimated from Eq.1.12 using a tunneling constant $t \simeq 2.8$ eV [6] as $E_{\max} \simeq 8.4$ eV.

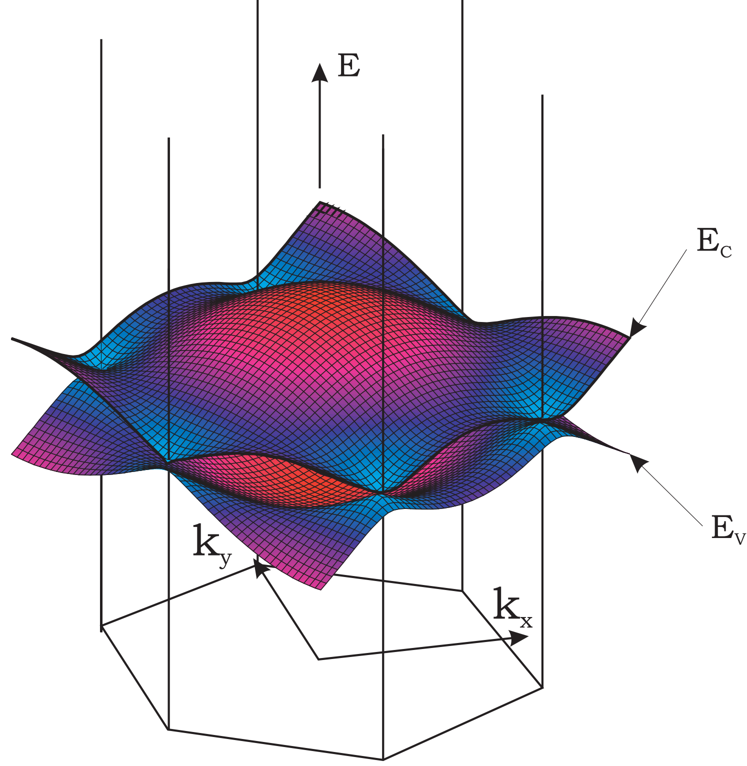

Figure 1.2: Band diagram of graphene in the nearest neighbours approximation according to relation 1.12.

1.2 Low energy approximation. Dirac Hamiltonian. Berry phase

In the low energy limit, when the Fermi energy measured from the touching point $E_{\mathrm{F}} \ll t$, the dispersion relation can be studied locally around the BZ corners, where the lines of constant energy approach a circular shape (blue, Fig.1.3). In Fig.1.4 the coloured sectors indicate inequivalent values of $\vec{k}$ for one of the sublattices. Due to the periodicity in k-space they can be merged into one cone (Fig.1.4), and to the opposite cone for the second sublattice.

Thus, further discussion will refer to two opposite valleys, with their centers at:

$$\vec{K}^{\pm} = \pm \frac{4\pi}{3a} (0, 1) , \tag{1.13}$$

and a wavevector $\vec{\kappa}$ designating a small parameter around $\vec{K}^{\pm}$:

$$\vec{k} = \vec{K}^{\pm} + \vec{\kappa} = \left(\kappa_x, \pm \frac{4\pi}{3a} + \kappa_y \right) . \tag{1.14}$$

One of the two components of the Hamiltonian (1.8) is

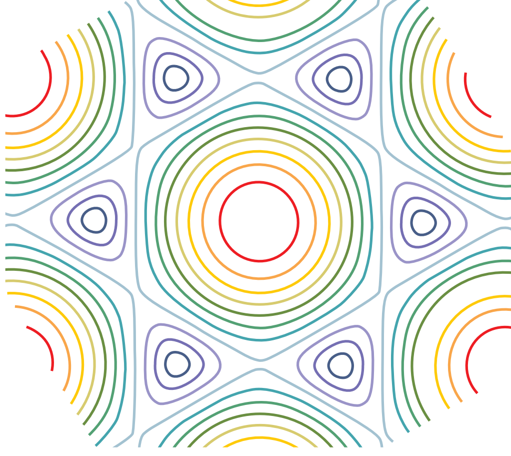

Figure 1.3: Lines of the constant energy for the graphene dispersion relation 1.12.

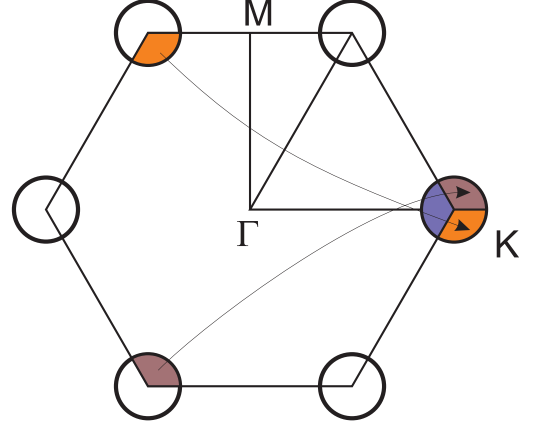

Figure 1.4: Change from the hexagonal Brillouin zone to the diamond-shaped.

$$\tilde{H}_{12}(\vec{k}) = \sum_{i=1}^{3} e^{i\vec{k}\vec{\delta}_i} = e^{ik_x a/\sqrt{3}} + 2\cos(\frac{k_y a}{2})e^{-ik_x a/2\sqrt{3}}.$$

This formula can be expanded, leaving only terms proportional to the first order of κ_x, κ_y, so that the Hamiltonian is linearized:

$$\tilde{H}_{12}(\vec{\kappa}) = \frac{\sqrt{3}a}{2}(i\kappa_x \mp \kappa_y),$$
$$\tilde{H}_{21}(\vec{\kappa}) = \frac{\sqrt{3}a}{2}(-i\kappa_x \mp \kappa_y),$$

where "+" corresponds to K^+ valley and "−" to K^-, so the Hamiltonian in Eq.1.9 for low energies is

$$H = \frac{-t}{(2\pi)^2} \int_{DC} [\varphi^\dagger_{K^+}(\vec{K}^+ + \vec{\kappa})\tilde{H}_{K^+}(\vec{\kappa})\varphi_{K^+}(\vec{K}^+ + \vec{\kappa}) + \\ + \varphi^\dagger_{K^-}(\vec{K}^- + \vec{\kappa})\tilde{H}_{K^-}(\vec{\kappa})\varphi_{K^-}(\vec{K}^- + \vec{\kappa})] d^2\kappa,$$

$$\text{where} \qquad \tilde{H}_{K^+} = \begin{pmatrix} 0 & i\kappa_x - \kappa_y \\ -i\kappa_x - \kappa_y & 0 \end{pmatrix} = -\sigma_2\kappa_x - \sigma_1\kappa_y,$$

$$\tilde{H}_{K^-} = \begin{pmatrix} 0 & i\kappa_x + \kappa_y \\ -i\kappa_x + \kappa_y & 0 \end{pmatrix} = -\sigma_2\kappa_x + \sigma_1\kappa_y.$$

and integration is done in the vicinity of the Dirac cones.

Note, that σ_1, σ_2 are two Pauli matrices usually associated with spin projections in quantum mechanics, but the spin was not included here before (will be added in the next formula). The Pauli matrices here operate on two sublattices and therefore refer to the different isospin projections.

These results can be combined in one 4x4 block-diagonal matrix adding up two spinors $\varphi_{K^\pm}(\vec{K^\pm} + \vec{\kappa})$ for different valleys (the new four-dimensional spinor denoted by $\Psi(\vec{k})$) and the resulting Hamiltonian takes the form [2]

$$H_0(k) = c\sum_\sigma \int_{DC} \frac{d^2k}{2\pi^2}\,\Psi^\dagger(\vec{k}) \begin{pmatrix} & K^+\Lambda_1 & K^+\Lambda_2 & K^-\Lambda_2 & K^-\Lambda_1 \\ & 0 & i\kappa_x - \kappa_y & 0 & 0 \\ & -i\kappa_x - \kappa_y & 0 & 0 & 0 \\ & 0 & 0 & 0 & -i\kappa_x + \kappa_y \\ & 0 & 0 & i\kappa_x + \kappa_y & 0 \end{pmatrix} \Psi(\vec{k}),$$

where c is a constant.

This low energy spinor structure of the Hamiltonian and the wave functions is a direct consequence of having two sublattices in the direct and reciprocal spaces. In a more compact view

$$H_0(k) = -c\sum_\sigma \int_{DC} \frac{d^2k}{2\pi^2}\,\Psi^\dagger(\vec{k})(\alpha_2\kappa_x + \alpha_1\kappa_y)\Psi(\vec{k}), \tag{1.15}$$

$$\alpha_i = \begin{pmatrix} \sigma_i & 0 \\ 0 & -\sigma_i \end{pmatrix} \qquad \beta = \begin{pmatrix} 0 & I \\ I & 0 \end{pmatrix}.$$

This view is similar to the Dirac (or Dirac-Weyl) equation for massless particles with spin 1/2 - one of the biggest physics developments in 20th century. Unlike the original Dirac equation, here we are dealing with a two-dimensional case and so

only two alpha matrices out of three are being used. Such an analogy between 2+1 (space + time) quantum electrodynamics (QED) and condensed matter was first demonstrated in [7]. The original Dirac equation also includes a non-diagonal mass term $\sim (-m\beta)$ which can be introduced in a similar manner for graphene for the case when Λ_1, Λ_2 are not equivalent.

The particular form of α_i shown here is usually called the “spinor” representation (in contrast to the ”standard” representation for the nonrelativistic case [8]). Usually in the literature α_1 and α_2 enter Eq. 1.16 in the opposite order due to a different choice of the coordinate system (x, y). Using such notation, the Hamiltonian is more convenient and after the Fourier transform will look like [8]:

$$H_0(r) = -i\hbar v_{\mathrm{F}}(\alpha_1 \partial_x + \alpha_2 \partial_y). \tag{1.16}$$

The dispersion relation for the time-independent case can be found from (1.16) as before (1.10):

$$E = \pm\hbar v_{\mathrm{F}} \left|\vec{\kappa}\right|, \qquad v_{\mathrm{F}} = \frac{\sqrt{3}}{2}\frac{ta}{\hbar} \approx 10^6 \text{ m/s}. \tag{1.17}$$

The linear dispersion [5] implies a constant carrier group velocity $v_{gr} = \left|\partial E/\hbar\partial\vec{k}\right| = v_{\mathrm{F}}$, independent of the Fermi energy. By analogy with QED, the Fermi velocity v_{F} plays the role of the speed of light c.

Since the Hamiltonian (1.16) has block-diagonal form it does not mix the states from different valleys $K^{\pm}$ and the wavefunction for one of the valleys can be found independently as follows:

$$H_{K^+}(x, y)\chi_{K^+}(x, y) = -i\hbar v_{\mathrm{F}} \begin{pmatrix} \frac{\partial}{\partial x} - i\frac{\partial}{\partial y} \\ \frac{\partial}{\partial x} + i\frac{\partial}{\partial y} \end{pmatrix} \begin{pmatrix} \chi_2 \\ \chi_1 \end{pmatrix} = E \begin{pmatrix} \chi_1 \\ \chi_2 \end{pmatrix}. \tag{1.18}$$

These two equations can be combined into the wave equation with the solution taken as a plane wave:

$$\frac{\partial^2 \chi_1}{\partial x^2} + \frac{\partial^2 \chi_1}{\partial y^2} = -\kappa^2 \chi_1, \qquad \chi_1 = A \exp\left(-i\kappa_x x - i\kappa_y y \pm \frac{iEt}{\hbar}\right), \tag{1.19}$$

where A is a complex constant and “±” corresponds to the different eigenvalues

$E = \pm\hbar v_{\mathrm{F}}\kappa$, i.e. the conduction and valence bands. Similar to the 'Dirac sea', one can think of two types of quasiparticle excitations: electrons having a positive value of energy and their "antiparticles" – holes with negative energies. The two resulting spinors in k-space, found for electrons and holes according to Eq.1.18, are

$$\chi^e_{K^+} = \begin{pmatrix} 1 \\ -e^{i(\frac{\pi}{2}-\theta)} \end{pmatrix}, \quad \chi^h_{K^+} = \begin{pmatrix} e^{-i(\frac{\pi}{2}-\theta)} \\ 1 \end{pmatrix}, \qquad \theta = \arctan\frac{\kappa_x}{\kappa_y}. \tag{1.20}$$

In a similar way one can find wavefunctions for the K^- valley.

By a gauge transformation this wavefunction can be written as (in momentum space) [6]:

$$\chi_{K^+} = \begin{pmatrix} e^{i\theta/2} \\ \pm e^{-i\theta/2} \end{pmatrix}, \qquad \chi_{K^-} = \begin{pmatrix} e^{-i\theta/2} \\ \pm e^{i\theta/2} \end{pmatrix}. \tag{1.21}$$

Let us imagine a closed loop trajectory in k-space, which encloses a point $\vec{\kappa} = 0$ and let the wavefunction travel in k-space adiabatically along this loop. During one turn parameter θ changes from initial value θ_0 to the final value $\theta_0 + 2\pi$ and the spinors in Eq. 1.21 gain an additional geometrical phase of π. This phase is usually called the Berry phase [9], and leads to a peculiar Quantum Hall Effect, which will be discussed later.

1.3 Chirality, DOS

Let us consider a direct analogy of the helicity operator from QED in (3+1) space-time dimensions [2]:

$$\Lambda^{2D} = k_x\Sigma_1 + k_y\Sigma_2, \qquad \Sigma_i = \begin{pmatrix} \sigma_i & 0 \\ 0 & \sigma_i \end{pmatrix}, \tag{1.22}$$

which is the pseudochirality operator for the (2+1) dimension case. One can see that this operator commutes with the Hamiltonian in 1.16 and therefore corresponds to a conserving quantum number, called *chirality*. The four-dimensional spinors built from the solutions of 1.20

$$\Psi^e_{K+} = \begin{pmatrix} \chi^e_{K+} \\ 0 \end{pmatrix}, \quad \Psi^h_{K+} = \begin{pmatrix} \chi^h_{K+} \\ 0 \end{pmatrix}, \quad \Psi^e_{K-} = \begin{pmatrix} 0 \\ \chi^e_{K-} \end{pmatrix}, \quad \Psi^h_{K-} = \begin{pmatrix} 0 \\ \chi^h_{K-} \end{pmatrix}, \tag{1.23}$$

are the eigenstates of Λ^{2D}:

$$\Lambda^{2D}\Psi^e_{K\pm} = \mp\Psi^e_{K\pm}, \qquad \Lambda^{2D}\Psi^h_{K\pm} = \pm\Psi^h_{K\pm}. \tag{1.24}$$

Therefore, this operator corresponds to the valley index. Since the pseudochirality operator is a projection of the isospin operator on the momentum operator by definition, one can build a direct vector analogy and represent the isospin as a vector $\vec{\sigma}$ in k-space. Thus, for the holes in K^+ valley eigenvalue of Λ^{2D}, i.e. chirality, is +1, and therefore $\vec{\sigma}$ and $\vec{\kappa}$ are codirectional. However, for electrons in K^+ chirality is -1 and therefore $\vec{\sigma}$ and $\vec{\kappa}$ are always opposite. The latter case is illustrated in Fig.1.5, where different colours indicate different chirality values.

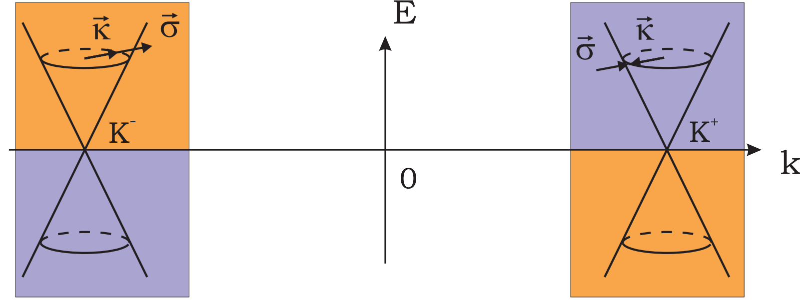

Figure 1.5: Illustration for the chirality in graphene – yellow and blue colours denote chirality of 1 and -1.

The chirality quantum number plays an important role when considering scattering of carriers in graphene.

In the presence of an external potential $V(r)$ which acts on both sublattices in the same way, there will be another term in the Hamiltonian (1.4):

$$H_{dd} = \sum_i V_i(a^\dagger(\vec{r}_i)a(\vec{r}_i) + b^\dagger(\vec{r}_i)b(\vec{r}_i)), \tag{1.25}$$

which acts as a shift of the chemical potential [6]. Depending on the potential $V(r)$ it can be local 'doping', as in the case for charged impurities, or a global effect, in the case of a back-gate potential. The carrier concentration induced due to this shift

(at T=0) can be found as

$$n = \int_0^{E_\mathrm{F}} g(E)dE, \tag{1.26}$$

where $g(E)$ is the 2D density of states for graphene, which, according to the linear dispersion relation (1.17) is

$$g(E) = \frac{1}{S}\frac{dN}{dE} = \frac{g_s g_v}{2\pi\hbar^2 v_\mathrm{F}^2}E. \tag{1.27}$$

Here S is the area, N is the number of states and g_s, g_v the spin and valley degeneracies, respectively. Thus, similarly to the silicon 2DEG [10]

$$k_\mathrm{F}^2 = \frac{4n\pi}{g_s g_v}. \tag{1.28}$$

1.4 Transistor structure: graphene on n-Si/SiO$_2$

The shift of the chemical potential, induced by an external electric field, allows one to control the carrier concentration in graphene. In order to do that, graphene is placed on a conductive substrate coated with an insulating layer. An electric potential V_bg applied between the substrate, i.e. 'back-gate', and the graphene causes an accumulation of the surface charge according to the capacitive coupling:

$$n = CV_\mathrm{bg}, \qquad C = \frac{\varepsilon\varepsilon_0}{de}, \tag{1.29}$$

where n is charge per unit area, C is the capacitance per unit area, $\varepsilon_0, \varepsilon$ are the electric permittivities of free space and the dielectric layer, d is the thickness of the dielectric and e is the electron charge.

For 300 nm thick silicon dioxide ($\varepsilon = 3.9$) as a dielectric layer grown on a highly doped n-Si substrate

$$n\ [\mathrm{cm}^{-2}] = 7.19 \cdot 10^{10} \cdot V_\mathrm{bg}\ [\mathrm{V}]; \qquad E_\mathrm{F}\ [\mathrm{meV}] = 31\sqrt{V_\mathrm{bg}\ [\mathrm{mV}]}. \tag{1.30}$$

Thus, by applying a back-gate voltage of up to 100 V one can induce a carrier concentration of $7.19 \cdot 10^{12}$ cm^{-2}. The sign of the charge of carriers depends on

the gate voltage sign, i.e. positive gate potential produces electrons and negative attracts holes to graphene. This structure was first made by K. Novoselov et al. [11] in 2004 and gave birth to experimental graphene research.

Due to the presence of inhomogeneities in SiO_2 there will be random fluctuations of spatial potential distribution. These fluctuations lead to the spatial charge inhomogeneity and breaks the graphene into a system of electron and hole puddles at low carrier concentrations. Such puddles were observed experimentally [12, 13] with characteristic concentrations $\sim 10^{11}$ cm^{-2}, which corresponds to $\sim 1 - 1.5$ V of the back-gate voltage.

1.5 Carrier scattering in graphene on SiO_2

The resistance measured as a function of the carrier concentration exhibits a peak centered at zero average concentration, with a monotonic decrease either side of this peak. This region is called the electroneutrality (EN) or Dirac region, and transport properties there are most probably determined by the charge inhomogeneities described earlier.

Away from the electroneutrality region, in usual graphene samples, transport is diffusive and described by the standard Boltzmann transport equation [14]. The conductivity is given by the Drude formula:

$$\sigma = en\mu, \tag{1.31}$$

where n is the concentration of mobile carriers and μ is the mobility given by [15]

$$\mu = \frac{ev_{\mathrm{F}}^2}{E}\tau(E). \tag{1.32}$$

The momentum relaxation time $\tau(E)$ is determined from the collision integral [15]:

$$\frac{\hbar}{\tau(E)} = 2\pi \int \left\langle |V_{\kappa,\kappa'}|^2 \right\rangle (1 - \cos(\theta_\kappa - \theta_{\kappa'}))\delta(E_\kappa - E_{\kappa'})\frac{d^2\kappa'}{(2\pi)^2}, \tag{1.33}$$

where κ, κ' denote the incident and scattered states, respectively, $V_{\kappa,\kappa'}$ is the scattering-potential matrix element, $\delta(E_\kappa - E_{\kappa'})$ is the delta function. The scat-

tering potential depends on the type of scatterers.

Considering a scattering potential with a characteristic size bigger than the inter-atomic distance in graphene, Ando et al. [14] demonstrated strong suppression of back-scattering processes. Let us consider a charge carrier following a diffusive trajectory with the momentum change $\vec{\kappa} \to -\vec{\kappa}$ within one valley. Due to chirality conservation, the isospin direction is always parallel to the momentum $\vec{\kappa}$. As was demonstrated earlier, a change of the isospin direction leads to the appearance of the Berry phase. In the absence of magnetic field such a trajectory always has a time reversal pair. Due to a total Berry phase of π these trajectories interfere in a destructive way, therefore suppressing the probability of backscattering (which also leads to antilocalisation quantum correction [16, 17]). Mathematically, the matrix element $V_{\kappa,\kappa'}$ in Eq.1.33 becomes proportional to $(1 + \cos(\theta_\kappa - \theta_{\kappa'}))$ due to the chirality conservation as was demonstrated in [15].

One important example of such scatterers are Coulomb impurities in silicon dioxide, since they are assumed to give a major contribution to the resistivity away from the EN point. Integration of Eq.1.33 taking into account Coulomb interactions results in a mobility independent of concentration [15]:

$$\mu_{ci} = \frac{e}{4\pi^2\hbar n_i} H_0, \tag{1.34}$$

where H_0 is a constant (which depends on the charge screening), n_i is the concentration of charged impurities. The resulting conductivity is a linear function of the concentration:

$$\sigma_{ci} = \frac{e^2}{4\pi^2\hbar}\frac{n}{n_i} H_0. \tag{1.35}$$

The experimentally observed values of $\mu = 10^4$ cm^2/Vs corresponds to an impurity concentration $n_i \sim 4 \cdot 10^{11}$ cm^{-2} [15], which, as it will be explained in the next chapter, is a realistic value.

The second type of scatterers are short-range, with a characteristic size similar to the carbon-carbon inter-atomic distance. This type of impurities breaks the sub-lattice symmetry and the Dirac model described earlier becomes inapplicable. It has been shown that the resistivity due to short-range scatterers does not depend on the carrier concentration [18].

Other sources of scattering in graphene are acoustic phonons (short-range) [19], optical phonons (short-range, originating from the substrate) [20], height corrugations of graphene sheet and midgap states [21]. A combination of these mechanisms according to Matthiessen's rule can explain the experimentally observed $\sigma(V_{\mathrm{bg}}, T)$ [22] and will be discussed in Chapter 4 in detail.

1.6 Conclusion

Experiments on suspended graphene sheets done by the Columbia group [23] demonstrate significant increases of the carrier mobility up to $2 \cdot 10^5$ cm^2/Vs (with the acoustic phonons as the dominant source of scattering). This indeed suggests that the scattering source originates from the charged impurities in the dielectric layer.

As was demonstrated in [15] the scattering on charged impurities strongly depends on the dielectric constant of the graphene environment, usually taken as the average for vacuum and silicon dioxide: $k = (k_{ox}+1)/2$. A recent experiment done by the Manchester group, where graphene was measured in a high k environment [24], demonstrates that the mobility increases by only 20%, instead of the expected increase of about an order of magnitude (if charges impurities in the substrate are the dominant scatterers). Moreover, the experiment in graphene placed on the different substrates [24] does not indicate a significant change in the mobility either, showing that the major contribution to the scattering processes can not be attributed to the charged impurities. These results are in direct conflict with experiments done by the Maryland group (for review see [22]), where the carrier transport in graphene was explained by the contributions given in the previous section. As a result, at the present moment the scattering in graphene is not fully understood and is a hot topic of scientific debate.

Therefore, the next chapter is dedicated to the study of the graphene environment and its impact on charge transport in graphene films.

Chapter 2

Experimental methods of graphene fabrication

2.1 Introduction

Since the graphene technology is in its earlier ages, a lot of attention should be paid to the details of the fabrication process. Some stages of the fabrication process usually take place in the laboratory or cleanroom environment. Since the air is a complicated mixture of common gases (nitrogen, oxygen, argon, carbon dioxide etc.) and a large number of traces of other species, it is impossible to count all contaminants arriving at a flake surface during and after its fabrication. The exact composition also changes in time and depends on the position within the lab environment. In the ideal case graphene should not be exposed to the air, but this is difficult to achieve and at present moment no methods have been reported whereby a graphene flake is always kept (when fabricated and measured) in a clean, controlled atmosphere. Therefore this chapter will consider various deposits on graphene surface and the graphene's environment.

An adsorption process is usually classified as chemisorption (e.g., a covalent bond formation) or physisorption (weak van der Waals forces), depending on the type of the force responsible for the attractive interaction. Graphene's surface is inert and will not readily chemically bond to most of the compounds it potentially meets in the fabrication process (at room temperature). This property of graphene helps to preserve the carrier mobility, as any π orbital taken out of the conduction band can

cause a scattering event.

Graphene will easily physisorb different atoms and molecules and their presence can influence the charge transport. For two unpolarized atoms brought into close proximity, their combined energy becomes lower due to the dynamical polarization effect $V \propto -1/r^6$. For one atom on a thick substrate, this energy has to be integrated over the substrate half space, giving $V = -c_2/d^3$, where d is the distance between the substrate and the atom, and c_2 is the Hamaker constant. Thus there is always an attractive interaction, even without considering adsorbates with a constant dipole or an electric charge, which will increase the interaction significantly.

If the surface is heated, the energy transferred to the adsorbed species will cause it to desorb. Thus, in the presence of such species in the environment, there will be a dynamical balance between incoming and leaving adsorbates. The rate of leaving follows an activation rule, $\propto x \exp(-u/RT)$, where x is the fraction of the surface covered by adsorbate, u is the binding energy and T is the temperature of the surface. The rate of arriving is $\propto (1-x)p$, where p is the partial pressure of the vapour. Therefore a contaminated surface can be cleaned by increasing its temperature (annealing) in a clean environment.

It is important to mention that due to the graphene deposition process, explained in detail in this chapter, some adsorbates will be trapped between the substrate and graphene and can not be removed by annealing. Apart from obvious candidate, H_2O, other species can also be trapped between graphene and the substrate. This circumstance was not considered before in the literature. Depending on energy level configuration of the impurity, even a few tens of molecules per square micron can be enough to cause noticeable scattering and doping effects.

The effect of the physisorbed materials can be generally viewed as a charge transfer and an additional source of scattering. Two electronic states of an adsorbed molecule are of particular interest for the understanding of the charge transfer: the highest occupied and lowest unoccupied molecular orbital (HOMO and LUMO). The positions of these levels can be imagined as delta-peaks in the DOS and need to be compared to the electronic band-structure of graphene. Thus, if HOMO is above the Fermi level there will be an electron transferred to graphene, and conversely, if LUMO is below the Fermi level there will be an electron transferred from graphene. As will be shown later, for many impurities direct transfer does not occur since E_{F}

is positioned between HOMO and LUMO. Apart from the direct charge transfer there is another mechanism determined by mixing of HOMO and LUMO with the graphene orbitals, i.e. hybridization. The mixing strength is inversely proportional to the energy level difference of mixing states and for usual atmospheric gases (CO_2, H_2O) results in the charge transfer of the order of $0.01e - 0.05e$ per molecule [25].

The third mechanism discussed theoretically [26] is a composite effect of the substrate and water: the authors demonstrated that H_2O molecules can shift the substrate impurity bands and change their hybridization with the graphene bands. The effect predicted can explain the strength of experimentally observed water doping (see Chapter 4). Similar to this mechanism, there can be other combinations of adsorbates which were, to best of my knowledge, not discussed in the literature.

2.2 Wafers for graphene deposition

2.2.1 General information

We use Czochralski-grown SEMI Prime grade n-type Si, doped with Sb or As to the resistivity of 0.02 - 0.001 Ωcm. It is important to have highly doped wafers so that the conductivity does not decrease to zero down to 100 mK temperature range, i.e. a doping level higher than 10^{19} cm^{-3} to form an impurity band. During the fabrication process, the wafer surface (100) is mechanically polished to an average roughness $\sim$ 5 Å and thermally oxidized at $\sim 1050°$ C in dry, 99.9999% pure O_2. During the oxidation, oxygen diffuses into the bulk Si and forms amorphous SiO_2, and as a result the initial top layer swells and becomes almost 1.5 times thicker. This process produces high quality oxide and low surface charge density in the oxide layer, 10^{10} cm^{-2} (all information specified by the manufacturer).

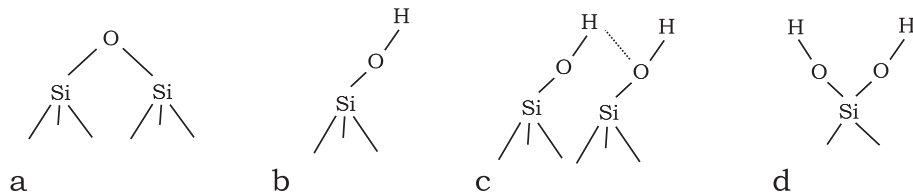

Figure 2.1: Different termination of the oxide surface.

We have sourced our wafers from two different suppliers [27,28], with an order of magnitude variation in the resistivity, two different dopants (As, Sb) and different

oxide thicknesses (in the range of 200-350 nm). However, there was *no obvious dependence of carrier mobility* and other graphene properties (see Chapter 4) on the wafer type, and AFM study of the oxide surface does not reveal any differences either. Therefore the following chapter will be considering graphene on arsenic doped silicon substrates with resistivity of 0.003-0.004 Ωcm from [28].

The surface of amorphous SiO_2 can be terminated either with a *siloxane group* (Fig.2.1a) with an oxygen atom on the surface or with a *silanol group* (Fig.2.1b). Silanol groups may interact forming a hydrogen bond if they are close to each other (Fig.2.1c) or share one Si atom as shown in Fig.2.1d [29]. Thus, a dangling bond formed on the surface will be quickly terminated by the atmospheric oxygen or water, and therefore graphene is deposited on a fully passivated surface.

2.2.2 Cleaning methods

Prior to graphene deposition, the wafers are cleaned (since the surface can potentially get contaminated during the shipping and storage). Three cleaning methods have been used:

1.
   - Acetone, room temperature (ultrasonic aggravation, 5-10 minutes), wet transfer to
   - IPA, room temperature (ultrasonic aggravation, 5-10 minutes),
   - dry in N_2 flow.
2.
   - Acetone, boil 56°C (ultrasonic aggravation, 5-10 minutes), wet transfer to
   - IPA, room temperature (ultrasonic aggravation, 5-10 minutes),
   - dry in N_2 flow.
3.
   - Piranha, $\sim$ 100°C (stirring, 1-5 minutes), wet transfer to
   - water, room temperature (ultrasonic aggravation, 5-10 minutes),
   - dry in N_2 flow.

The first method is a standard method of cleaning. The second is a more aggressive version of the first, utilising normal behaviour of organic solvents to increase

its reactive ability at higher temperatures. The third method also originates from the semiconductor industry. It uses 'piranha etch' – a mixture of sulfuric acid and hydrogen peroxide which is especially good in removing organic residues. This mixture is a strong oxidizer and will also hydroxylate most surfaces (add OH groups), making them hydrophilic [30]. We use a typical mixture – 3:1 concentrated H_2SO_4 to 30% H_2O_2 aqueous solution, which reacts exothermically when mixed increasing its temperature to $\sim 100°$C.

The silica wafers cleaned with methods 1 and 2 demonstrate a finite wetting angle with water on the surface, whereas the third method makes the surface completely wettable, indicating dominant silanol termination (Fig.2.1b) of the surface. These cleaning methods give either no or a negligible impact on the carrier mobility in graphene devices and the only difference we have mentioned is a small change in adhesion between the wafer surface and graphene (discussed further in the corresponding Section 2.5).

(All chemicals used were purchased either from Fisher Scientific UK Ltd or Sigma-Aldrich Company Ltd. We normally use general laboratory grade, electrochemical or trace analysis grades of solvents, with all the specifications available online on the manufacturers websites.)

2.2.3 Surface topography

As an initial experiment we have studied SiO_2 wafer prior to graphene deposition. Tapping mode AFM (TAFM) with typical free oscillation amplitude $\sim 30 - 40$ nm and a spatial step size ~ 1 nm were used to obtain a small area scan of a pristine silica surface, Fig.2.2.

The resolution of such an image is limited by the system noise and the AFM tip size, i.e. the curvature radius of its end. We have used extra-sharp diamond-like carbon (DLC) tips with typical curvature radius ~ 2 nm (nsg01-DLC from NTMDT), and estimate the limit of spatial resolution as 5 nm. The system noise is below 1 Å (in z-direction). The upper inset of Fig.2.2 shows the height distribution of the scanned region (black) with a Gaussian fit (red). The standard deviation for this fit $\sigma = 0.26$ nm, gives a good measure of disorder in the vertical direction.

For characterization of surface roughness size in x,y direction, we use the au-

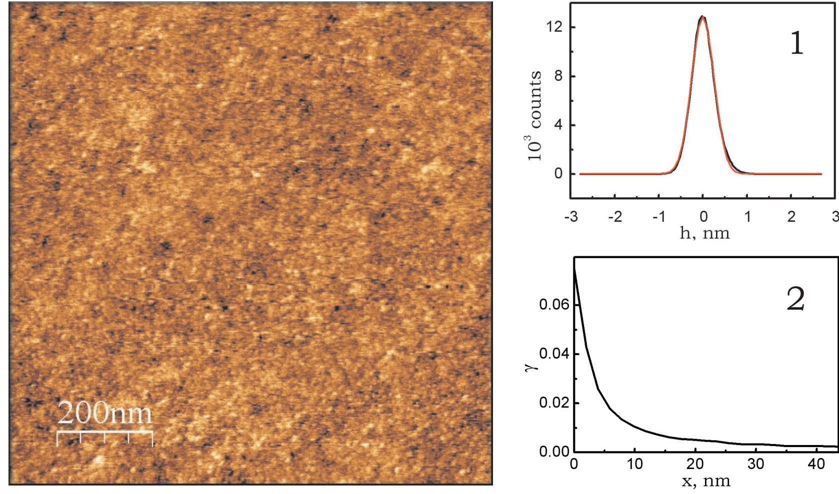

Figure 2.2: TAFM surface image of silicon dioxide, 1 - roughness distribution and 2 - autocorrelation function for the given image.

tocorrelation function – the result of cross-correlating the surface profile with the same profile shifted by $\vec{\rho}$:

$$\gamma(\vec{\rho}) = \int h(\vec{r})h(\vec{r} - \vec{\rho})d\vec{r}, \tag{2.1}$$

where $h(\vec{r})$ is the measured height map. A periodicity in the original data would be reflected in its $\gamma(\vec{\rho})$ function, plotted on the lower inset of Fig.2.2, which appears to have no certain period or feature size. The same autocorrelation, $\gamma(\vec{\rho})$, also carries information about the variance $\sigma^2 = \gamma(0)$. As a measure of the spatial disorder the quasiperiod ρ_c can be used, which is defined to be the value of ρ at which $\gamma(\vec{\rho})$ drops to half its maximum value. For these data it is equal to 4 nm and because this value is too close to the tip size, it cannot be treated as a real characteristic of the silica morphology.

2.2.4 Water on SiO_2

Simple arguments in section 2.1 show that there is always an attractive force even for non-polar molecules. In addition to water being polar, it likes to hydrogen bond to (OH) groups on the SiO_2 surface and to itself, Fig.2.3.

The conclusions of recent work are that there is always at least one monolayer of H-bonded water on a silica surface [31]. Moreover, XPS study [32] (X-ray photoemission spectroscopy) shows the presence of two monolayers of water already at

15% RH (typical laboratory values 30-60% RH).

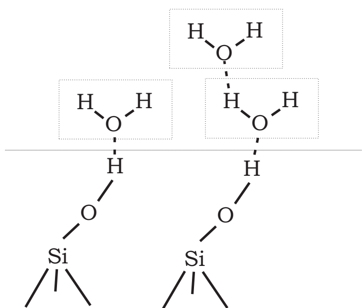

Figure 2.3: Water H-bonded to silanol terminated SiO_2.

Figure 2.4 was taken from [32]. Filled symbols show the dependence of water film thickness against relative humidity in the environment. Vertical dashed lines indicate 2 and 4-5 monolayer thicknesses and divide the dependence into three distinct regions. Open circles show the surface potential measured with Kelvin-probe AFM.

It is clearly seen that the first two monolayers do not change the surface potential, indicating random or parallel orientation of the dipole moment of water molecules, dictated by the rough silica surface. In the intermediate region there is a slowdown in the adsorption rate and the main change in the surface potential occurs, showing formation of perpendicular dipole-oriented water layers. Further increase of RH leads to a rapid increase in the film thickness with formation of a bulk droplet near 100 % RH without affecting the surface potential.

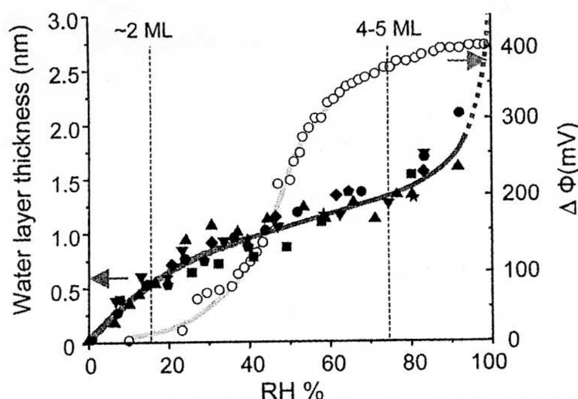

Figure 2.4: Dependence on the relative humidity of: water film thickness on SiO_2 by XPS study (left axis) and the surface potential measured by Kelvin-probe AFM (right axis) [32].

2.3 Graphite

2.3.1 General information

Graphite is a three dimensional crystal composed of stacked graphene layers. There are two forms of graphite, hexagonal and rhombohedral, that have very similar physical properties and differ in the way how the layers stack. Figure 2.5 illustrates the so-called AB Bernal stacking (hexagonal lattice), where an atom B from one sublattice in the bottom layer has above it an atom $\bar{A}$ from another sublattice of the upper layer, as shown in Fig.2.5. In the rhombohedral structure the third layer does not repeat the position of the first one and is moved relative to the second layer by the same amount as the second shifted compared to the first one, so the stacking can be represented as ABC. The interlayer π-interaction (~ 0.05 eV/atom) is considerably smaller than covalent in-plane bonds, and therefore the physical, mechanical and thermal properties of graphite have distinct anisotropy, with one result that the crystal can be easily cleaved in one direction.

Graphite used for deposition of the thin films is a polycrystalline material originating from one of the following sources:

1. Highly Ordered Pyrolytic Graphite (HOPG);
2. Kish graphite;
3. Natural graphite.

HOPG is a synthetic product widely used in different scientific experiments as a substrate. The growth of HOPG is based on thermal decomposition of hydrocarbons with further graphitization at a high temperature ($\sim$3000°C). The controlled growth of this material allows it to be chemically clean and AB stacked, however it may still have lattice defects. The second type, Kish graphite is a byproduct of the metal industry and is produced during the cooling of molten steel. Therefore, it is expected to have metallic impurities, yet can also be chemically purified. Natural graphite is mined around the world in the form of a lump, amorphous and crystalline flake graphite, and its properties strongly depend on the geography. However, even good-quality monocrystals of natural graphite may contain up to 5 % of rhombohedral phase which is known to have smaller average interlayer distance [33]. Pristine

and chemically purified samples of all three materials are commercially available from various suppliers (Toshiba Ceramics Co., NTMDT, NGS Naturgraphit GmbH, Branwell Graphite Ltd., etc.).

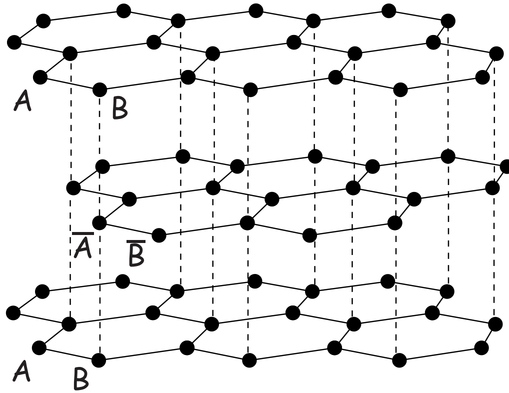

Figure 2.5: Hexagonal graphite lattice arranged in Bernal $A\bar{B}$ stacking.

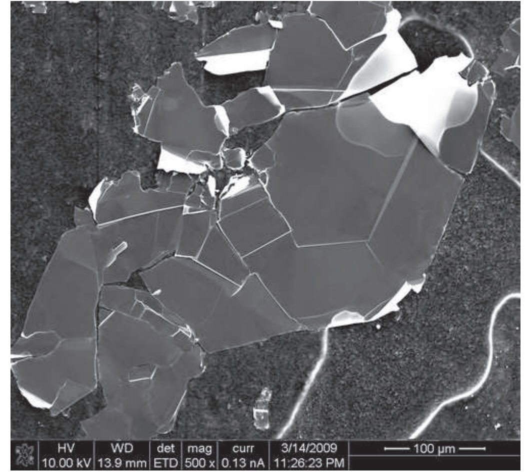

Figure 2.6: SEM image of natural graphite, scale bar 100 μm.

All three types of graphite were used in this project. The carrier mobility of graphene devices seems to have no direct dependence on the graphite source used, however most of the samples were made of natural flake graphite mined in Madagascar. The choice of this particular type is based on the big lateral size of monocrystalline areas it is made of and therefore the big size of graphene flakes extracted (up to 50 μm).

Fig.2.6 shows an SEM image of a graphite flake with a lateral size of $\sim$ 1 mm. The surface is freshly cleaved using a sticky tape (procedure explained in the section 2.4). One can see that the large graphite flake is composed of smaller crystals with lateral size of $\sim$100 μm and a few microns thick [33]. An AFM study shows that the regions that appear flat in figure 2.6 actually represent smaller atomically flat terraces of a few microns lateral size.

The flake graphite from Madagascar is known to have one of the biggest flake sizes and smaller electrical resistance [33]. It is also known that average interlayer distance is a good measure of crystal quality, and this parameter is small (0.33538 nm) for Madagascan and Korean graphites, indicating good layer matching and absence of intercalated impurities [33]. (It is important to mention that different research groups reporting on similarly high-mobility graphene samples do not use the same

source of graphite, e.g. Manchester [34] and Columbia University [35] tend to use natural and Kish graphite, respectively, both with the lateral flake size reaching ∼100 μm.)

2.3.2 Adhesion to graphite surface

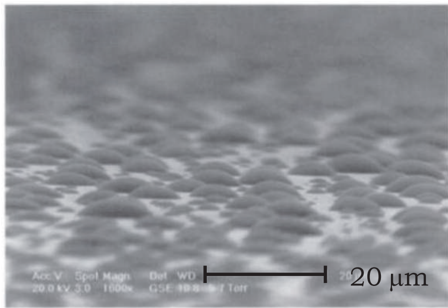

Figure 2.7: Micrometer size water droplets on graphite surface [36].

A simple experiment involving putting a small water droplet on a graphite surface shows that graphite is hydrophobic, with a water droplet contact angle around normal. The contact angles are very sensitive to the purity of the water, so smaller angles can be observed in experiment. Indeed, Fig.2.7 shows experimental results obtained on an ESEM (environmental SEM) revealing the presence of water droplets on the surface with a few micron lateral size and contact angles ∼ 30% [36]. The presence of water droplets has also been confirmed in a non-contact AFM study [37], where at 60 % RH water droplets pinned to the atomic steps have been observed.

Due to the fact that there is always an attractive interaction between water molecules and the graphite surface, there will always be some molecules on the surface. For the interaction energy, numbers as big as the energy of the H-bonded water dimer can be found in literature [38]. Due to the high bond saturation of graphite atoms and its atomic flatness, water molecules can diffuse on the surface, and water-water interaction becomes of high importance. So above a thin sub-monolayer layer molecules will bunch up to form a drop, pinned near a lattice defect or an atomic step.

Important information about the graphite surface is rooted in the friction studies performed between 1950 and 1980. It was found that, in a vacuum below ∼1 mbar the friction coefficient of graphite increases from its usual value 0.15 to about 0.5 and the graphite surface wears down much quicker as a result. Moreover, it was shown that a small amount of water or other condensable vapour restores the low friction

regime [39]. It was also proven [40] that no usual air gases intercalate between the graphite planes, so this effect originates from the surface 'lubrication' only.

Vapour	θ_T at 10 Torr (°C)	Adsorption energy (kcal mol^{-1})		Source
		Dusting experiments	Literature	
Methane	—	—	3.03	1 Constabaris *et al* (1961)
Ethane	38	8.9	4.3	2 Bezus *et al* (1964)
Propane	121	10.6	6.5	3 Kiselev (1961)
Butane	188	12.5	8.8	4 Beebe *et al* (1947)
Pentane	215	14.1	9.1 10.2	5 Kiselev (1967) 3 Kiselev (1961)
Hexane	253	15.3	11.2	6 Isirikyan and Kiselev (1961)
Heptane	327	17.2	14.0	3 Kiselev (1961)
Methanol	64	14.5	5.3	7 Kiselev and Yashin (1960)
Ethanol	152	15.7	6.9	7 Kiselev and Yashin (1960)
Propanol	192	18.3	8.1	7 Kiselev and Yashin (1960)
Iso-propanol	177	16.6	—	7 Kiselev and Yashin (1960)
Butanol	—	—	9.4	7 Kiselev and Yashin (1960)
Water	140	145	4.6 8.9–9.9 8–9 12.5	8 Gale and Beebe (1964) 9 Keyes and Marshall (1927) 10 Avgul *et al* (1963) 11 Millard *et al* (1955)
Oxygen	42	9.2	3.5	9 Keyes and Marshall (1927)
Hydrogen	—	—	1.8 1.9 2.0	12 Barrer and Rideal (1935) 9 Keyes and Marshall (1927) 13 Barrer (1937)

Figure 2.8: Comparison of binding energies of molecules on graphite surface obtained from the friction experiments to other values in literature. From [41].

Studying the conditions at which the switching between low and high friction occurs allows one to estimate the binding energy of the surface species which promote the sliding. The results of one of the latest (1981) experiments done on the 'dusting transition' of graphite [41] are shown in Fig.2.8. Binding energies measured are also compared with those obtained from adsorption experiments done by various groups with the main consequences listed as follows:

- Although values of the binding energy obtained in [41] are consistently higher that those reported before, they claim they are still characteristic of the physical adsorption on the basal plane of graphite.
- Thus, there is always a sub-monolayer film coverage on the graphite surface of water, oxygen and other species present in the air.
- Hydrocarbons will also adsorb on the surface. For instance, the binding energy of n-paraffins is almost linearly proportional to their molecular weight and,

even for the light alkanes, comparable to that for water. Similar behaviour can be expected for arenes and various complicated molecules present in the air.

- Alcohols and other organic solvents used during fabrication have similar binding energies to water and may also be present on the graphite surface.

2.4 Conventional graphene deposition

The following procedure was used in [34] to obtain the first graphene flakes and is often called 'micromechanical cleavage' in the literature. It is still used by most researchers in the field and was utilised in this project.

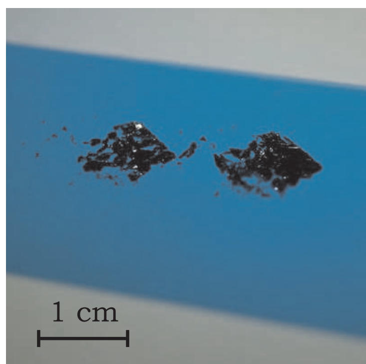

Figure 2.9: Nitto adhesive tape (blue) with graphite flakes (black).

We use single-side adhesive 'Nitto' tape (SWT-20), which is used in the semiconductor industry for wafer protection. The tape consists of a specially formulated acrylic adhesive $\sim$ 10 μm thick on a PVC film carrier. A small piece of graphite (usually a few mm lateral size and less than 100 μm thick) is placed between two pieces of the tape and then two tapes are torn asunder, splitting the graphite piece into halves (Fig.2.9). This procedure is repeated a few times until the graphite covers a significant area on the tape surface. The tape is then pressed against a freshly cleaned wafer with a pressure of 100 N/cm^2 and removed straight away. This creates many flakes on the surface of the wafer with a variety of thicknesses from a monolayer up to a few microns held by the van der Waals force. Once the tape is attached to the surface, the best result usually comes with the force applied perpendicular to the surface. Lateral displacement of the tape during deposition does not lead to significant improvement in the number of deposited thin flakes. Increasing the vertical pressure leads to an increase in the total flake density but can damage the surface oxide layer and leaves unwanted dust. Therefore, the contact area between graphene surface and the wafer is important for interaction. For instance, deposition on the rougher (twice bigger rms value) surface of Al_2O_3

with other conditions being equal gives almost zero flake density. For each deposition a fresh wafer is used, i.e. we never 'reuse' the wafers again. Repeated placement of the tape on the surface can, with a high chance, remove a flake.

Typically, graphite flakes occupy a few percent (0-5 %) of the total wafer area. The presence of organic contamination (e.g. skin secretion, exhaled air, vacuum grease) on the surface often increases the flake adhesion and therefore the covering ratio. On average, the described procedure gives at least one $\sim 20\ \mu$m monolayer flake on a 4 cm^2 wafer (also depending on the source of graphite).

2.5 Environmental graphene deposition

After a number of graphene depositions done according to the procedure explained above, we have found that two depositions done in exactly the same way do not result in the same average flake density. The reason for this can be that the adhesion force depends on the environmental conditions, especially taking into account the fact that the deposition was done without temperature and humidity control.

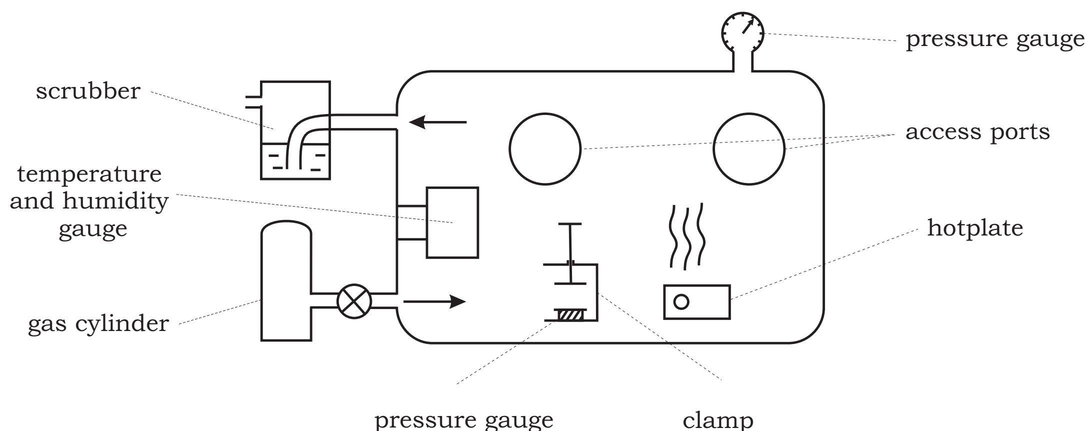

Figure 2.10: Chamber for environmental graphene deposition.

An experiment was performed inside a glove-box where environmental conditions can be controlled. The experimental setup is shown schematically in Fig.2.10. The hermetically sealed metallic case with clear perspex windows has two ports with embedded rubber gloves used for the manipulations inside the chamber. (Prior to the experiment the glove-box was fully cleaned using organic solvents, sealed and leak tested.) Clean, dry argon (99.999% pure) was continuously passed through the chamber at the rate of 2-5 litres/min and released to the atmosphere via a liquid

scrubber. After approximately 40 hours of purging, the humidity inside the glovebox saturated at ∼5% (the limit of the humidity sensor). Variation of humidity was achieved by evaporation of a small amount of water using a hotplate and intermixing of the gas inside the box.

In order to account for randomness we have used sifted graphite material with 1.5 mm piece size. Four such pieces were placed on the tape and cleaved approximately 10 times until graphite covered the tape completely. Then the tape was pressed against the wafer surface using a mechanical clamp with a pressure gauge and then released. 10 mm square wafers were cleaned using piranha solution as explained in section 2.2.2 prior to the deposition.

Fifty optical images 0.5×0.5 mm^2 in size were collected from random places in the middle of the wafer. These images were then analyzed by a program [42] which calculates the total area covered by flakes and the result was averaged. This procedure was repeated for 10 wafers at each humidity to account for the random nature of the deposition process.

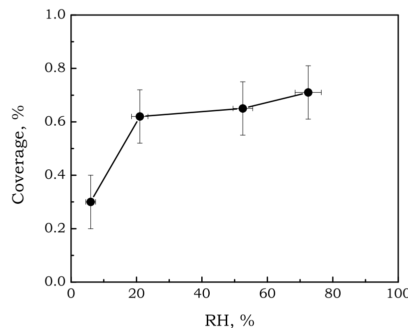

Figure 2.11: Density of deposited graphite as a function of relative humidity.

At the lowest humidity it was found to be impossible to deposit any noticeable graphite density using the same pressure as that used in the 'usual' air environment. Therefore, the pressure was increased up to five times in order to obtain a measurable graphite coverage. Figure 2.11 shows the density test result for 4 different humidity values. The lowest humidity (5-7%) results in a coverage of 0.3% of the total wafer surface. This value does not entirely correspond to the graphite flake density as at least half of it represents crumpled graphite dust and various surface defects. Increase in humidity to 20% leads to a few times higher density of the flakes deposited, again with the same 'dust' background of ∼ 0.15 %. Further increase of

humidity introduces no or a weakly rising dependence below the experimental error.

These results reflect the relative adhesion force between the wafer and the tape, and tape may also change its properties in different environments. However, if the substrates are not annealed prior to the graphene deposition, the observed effect does not appear, i.e. the density is almost independent of the humidity. This result suggests that the presence of environmental species (e.g. water) promote the adhesion of graphite on silica.

The water layer thickness measurements [32] shown in Fig.2.4 also resemble our density tests, suggesting that the water layer indeed increase the force and promotes adhesion. One reason for this can be that the water smoothers the roughness in the silicon dioxide making the effective contact surface larger.

It is also important that flake density resulting from the glove-box deposition is always below the atmospheric value, even if the humidity outside and inside the box is made almost equal (in this case, densities are approximately two times different). This suggest that other atmospheric gases also help graphene to adhere onto silica surface.

2.6 Thin flakes search and identification

Single and few-layer flakes were found on the surface using an optical microscope (Nikon Eclipse LV-150). Each wafer was routinely examined under 200 times magnification (500 for small flakes), yielding about 1-2 single-layer flakes (size bigger than 10 μm) per centimeter square of wafer for the conventional deposition process. Since we normally do not modify the flake's shape (see the next chapter), we have to select appropriate flakes for devices out of those found. Many thin flakes are attached to thicker ones and therefore effectively shunted, so less than half the number can be used for devices without etching. Figure 2.12a shows a multi-step flake under white light, with two regions labeled as monolayer and bilayer.

The visibility of graphene has been studied theoretically [43] and experimentally [44]. It was shown that the flake's contrast oscillates as a function of the oxide thickness, due to the interference of the reflected light. In particular, 280 nm was suggested as a good oxide thickness with the maximal contrast in the green part of the optical spectra (also, the human eye is more sensitive to green). Fig.2.12b,

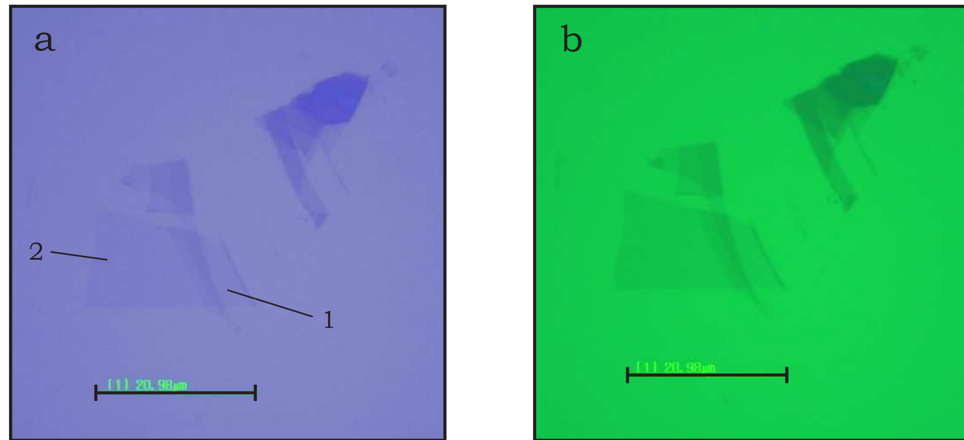

Figure 2.12: Optical image of a multi-step flake under optical microscope, (a) with white light source, (b) green filtered. Scale bar is 20 μm. 1 and 2 denote single layer and bilayer parts.

obtained using a green filter, indeed gives better contrast for this particular oxide thickness.

We have observed that putting a thin PMMA layer on top of the graphene deposited oxide can actually increase the graphene visibility by a few percent. Once coated by this layer, graphene is also protected from the potential atmospheric contaminants during its location, so most of our samples were spin-coated straight after the deposition procedure.

2.7 AFM study of graphene and its environment

2.7.1 Introduction

Ultra high resolution provided by scanning force microscopy makes it an attractive tool for graphene surface study. Among a large variety of different approaches to the scanning force microscopy, the most popular and reliable are Scanning Tunneling Microscopy (STM) and Atomic Force Microscopy (AFM) briefly reviewed below, as well as their current implementation in graphene study.

In an Atomic Force Microscope a sharp tip is used to scan across a specimen surface. In close proximity to the sample surface, this tip experiences different forces, which leads to elastic deformation of the cantilever. Such deformation is usually detected using a laser beam shining onto the top surface of the cantilever, and reflected onto an array of photodiodes. The cantilever (or sample) is mounted

on a piezoelectric tube which moves it in x-y surface directions. Another piezo crystal moves the sample in perpendicular z-direction, maintaining constant force (or distance) between tip and the sample through a feedback circuit. The resulting response plotted in x-y represents the force topography of the sample.

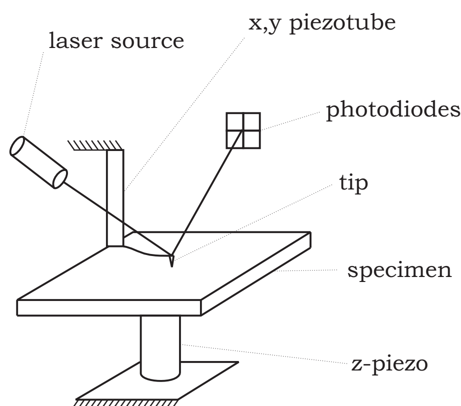

Figure 2.13: Schematics of scanning probe microscope.

Two modes were used for atomic force microscopy: contact (static) and tapping (dynamic). In contact mode (CAFM) the tip is pressed into the sample surface and the deflection of the laser spot provides a feedback signal. In tapping mode (TAFM) the cantilever is forced to oscillate at a frequency near its resonance by an extra piezo crystal. When the tip interacts with the surface the oscillation amplitude (also phase and frequency) will change and this provides the feedback signal. It is generally known that tapping mode is gentle enough to image single molecules and soft biological tissues when used correctly.

Unlike AFM, Scanning Tunneling Microscopy involves current measurements. A bias voltage is applied between a specimen and a conductive tip. When the tip is brought into close proximity with the surface a tunneling current can be measured and used for feedback. In spite of its high accuracy this technique requires the whole surface of the sample to be conductive.

The results below were obtained on a NTEGRA AFM (from NTMDT). The system is placed on an antivibration table and can be covered with an acoustic hood to reduce the external noise. It also has the ability to perform experiments in a vacuum or gas environment.

2.7.2 Step height measurements

Monoatomic layers in graphite are packed together according Bernal stacking and separated by 0.335 nm. If one such layer is taken out of a crystal and deposited on silica surface, one would expect the distance between graphene and the substrate to increase, as the hexagonal atomic lattice does not match relatively rough amorphous

oxide. Since the beginning of experimental graphene studies [34], step-heights measured by AFM reported by different groups vary from 0.4 to 2 nm. TAFM does not give a purely topographic image as the tip interaction depends on the mechanical properties of the material and different tip-surface interactions, such as capillary, electrostatic and van der Waals. The authors of [45] recently showed the importance of the choice of free amplitude and setpoint and demonstrated that a change in the free amplitude from 20 to 30 nm may lead to 1 nm difference in the step-height measurements between silica and graphene. The difference was attributed to the change of the tip-surface interaction from long-range attractive regime (van der Waals, electrostatic, liquid layer capillary forces) to the short-range repulsive regime (atomic forces) when the tip is brought closer.

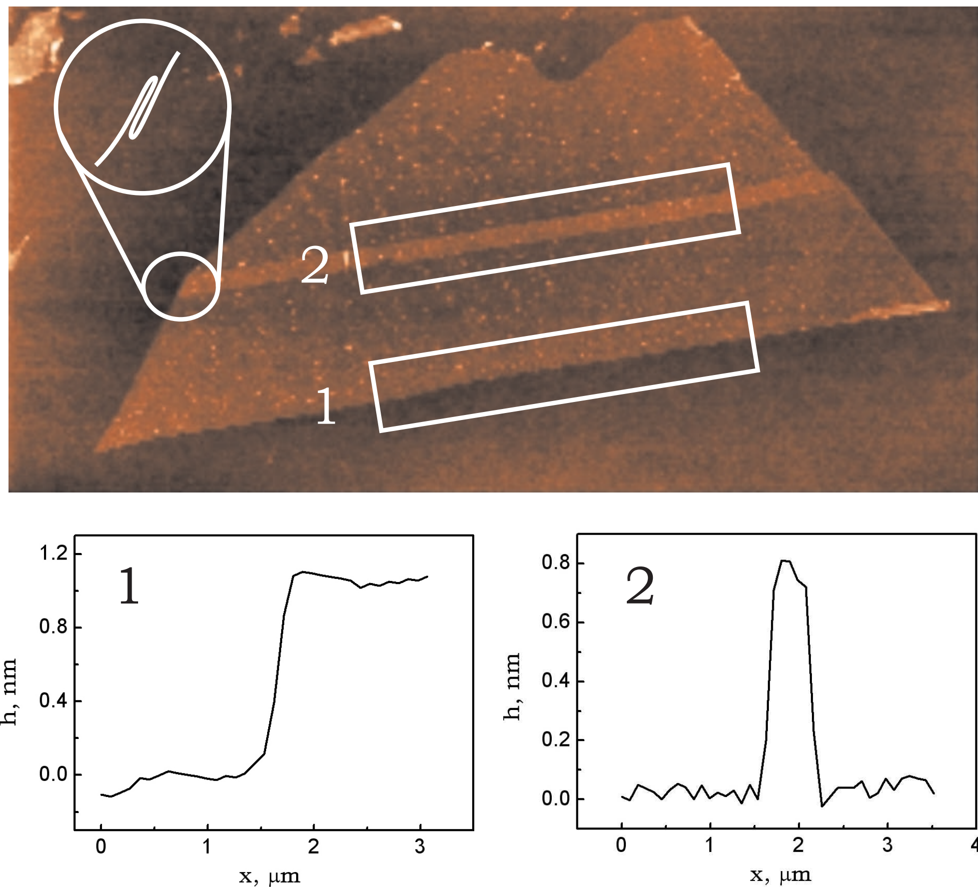

Figure 2.14: TAFM image of a folded graphene flake. Insets give the height profiles averaged over rectangular boxes 1 and 2, respectively.

Although we have not studied the reported bi-stability [45], the measured thicknesses of graphene also vary from 0.7 to almost 2 nm in our experiments in air. Thus, the image in Fig.2.14 was taken in the repulsive regime, while the image in Fig.2.15

corresponds to the attractive regime according to [45]. Both flakes are single layers with the same optical contrast, but the first demonstrates a step height of ~ 1 nm and the second ~ 2 nm with particular scan settings.

A common practice, started in [46], is to use folded regions on the flake to measure graphene-graphene step height. Because in this case surface-tip interaction has the same type, measured values correspond to the actual topography and are usually ~ 0.4 nm in our experiments. For example, Fig.2.14 shows a flake with a double folded region. The step-height was analysed and averaged for the regions in white boxes, with the result shown in the insets 1 and 2. One can see that double fold graphene-graphite is 0.8 nm and the 'normal' step graphene-silica is 1 nm.

2.7.3 Morphology of graphene on silica

The stability of free-standing two dimensional crystals has been a subject of theoretical discussions since 1968 [47]. The formation of intrinsic rippling was predicted earlier (see review in [48]) and confirmed experimentally [49], where intrinsic corrugations of a suspended graphene flake were studied.

One would expect the shape of a flake to be different when placed on a substrate. Atomic resolution STM study of graphene on an insulating substrate confirms the presence of a graphitic lattice, and the results show either almost ideal hexagonal structure [50] or one only slightly affected by the interaction with the substrate [51]. However, the authors of both articles state that the observed roughness of graphene can be fully explained by the underlying SiO_2.

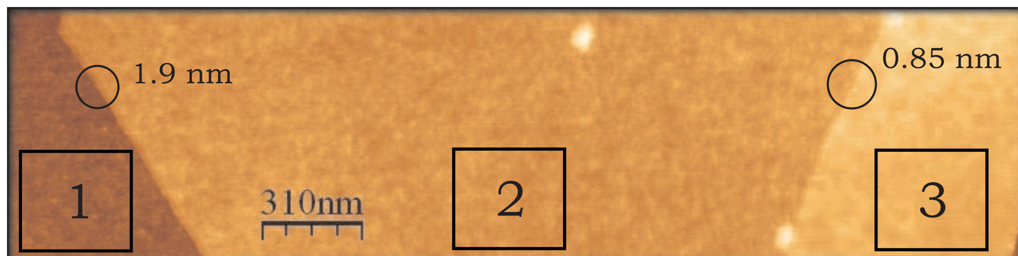

Figure 2.15: TAFM image of a graphene flake. Number 1 denotes SiO_2, 2 – graphene single and 3 – triple-layer regions.

The TAFM image in Fig.2.15 shows a flake with a single layer (2) and triple layer (3) region. As explained above, the measured height of graphene, 1.9 nm, depends on the AFM scan parameters. The roughness of various graphene samples

was analysed for fixed size areas and compared with oxide and 2,3-layer regions as shown in Fig.2.15. Although different tips and scan parameters cause slight variation in the results, *graphene is generally smoother* than the SiO_2, with rms values being approximately 65-85% of that of the oxide. Our observation shows that the roughness of graphene originates from the silica but does not follow its shape completely due to the finite stiffness of graphene, and becomes flatter for bi- and trilayers. These results generally agree with [50, 51]. No additional periods or patterns (reflected in the autocorrelation function) arise in graphene and few-layer graphite. For few-layer graphite the correlation length becomes bigger than the tip size, for instance 14 nm for trilayer graphite, because stiffer flakes cannot follow short size height fluctuations of SiO_2.

Currently there is only one paper [52] claiming appearance of small ($\sim$ 15 nm) period intrinsic corrugations of the graphene surface on silica not caused by the substrate. The authors compared the AFM image of the silica surface with high resolution STM images of graphene in order to prove that short period corrugations are intrinsic for graphene and do not originate from the substrate. However, careful analysis of silica explained above shows that the oxide structure is actually finer, with a correlation length smaller than 5 nm, in contrast to the reported value of 25 nm in [52], and can be responsible for the observed ripples.

2.7.4 Effect of high electric field on SiO_2 wafers

Using the capability of NTEGRA system to do nanolithography, we have tried to move the flakes by pushing them with an AFM tip in order to see the presence an additional material underneath (such as adhesive tape residue or other solid contaminations). This work was done by the author and David Horsell from Exeter University. Both the back gate and the conductive tip (NSG01/W2C) were grounded during this experiment. Image (a) in Fig.2.16 is a TAFM scan of two graphite flakes deposited using the conventional method. The top flake is approximately 120 nm thick and the bottom is 70 nm. After image (a) was taken, the tip was moved along the green arrow (Fig.2.16a) maintaining a constant force applied against the surface. The subsequent image is shown in Fig.2.16b and demonstrates that the flake is now folded, exposing a region of oxide underneath. A closer scan of the indicated

region, Fig.2.16c, reveals no difference between the oxide under and around the flake, and also the absence of glue residue or other solid contaminants between graphite and the oxide. (Regions along the flake edge on the last image are lower than the surrounding oxide, because of an artifact arising from the background subtraction procedure.)

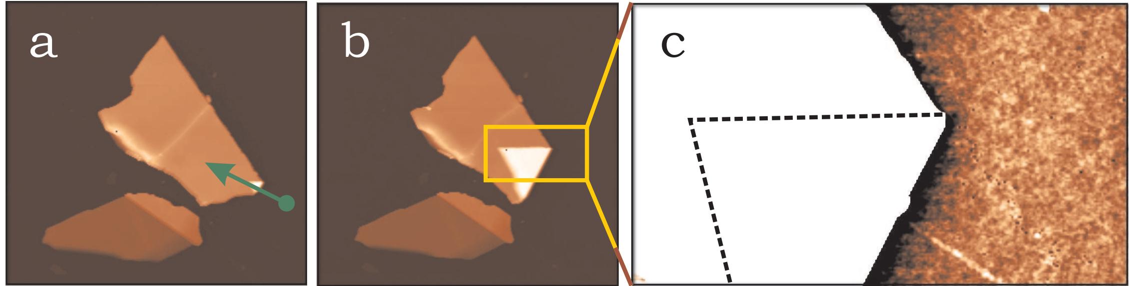

Figure 2.16: Flake manipulation using the AFM tip. (a) TAFM scan of the initial flake, b – folded flake, c – zoomed area indicated on image b.

The charge density in bulk SiO_2 and on the surface may differ when a large 10^9 V/m electric field is applied between the gate and a graphene flake. The following experiment on the same flake shows that charging effects in the silica can be important in electronic transport thought a graphene flake. Keeping the gate grounded, the tip with 10 V applied was brought into mechanical contact with the flake for a few seconds and then retracted. Thus, a parallel-plate capacitor was formed with 10 V potential between the 'plates' separated by the 300 nm silica dielectric layer. The flake was then peeled back using the AFM tip in order to reveal the oxide underneath, as shown in Fig.2.17-1.

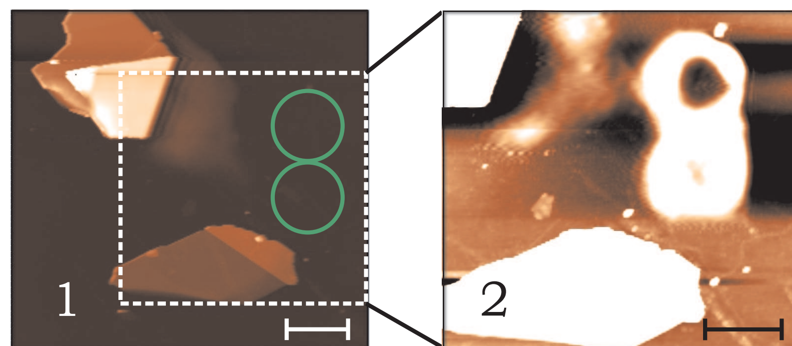

Figure 2.17: Effect of local charging of silicon dioxide. Scale bar is 2 μm.

One can see that the oxide underneath the flake demonstrates a significant charging effect, seen as a 30 nm hump on the surface (caused by the electric field). This effect is reproducible and has the same magnitude for the reversed sign of potential.

An image taken several hours later shows this charging to have partially diminished, probably due to charge dissipation in ambient conditions (humid air). Repeating these measurements in vacuum can partially restore the magnitude of the observed signal, showing that surface species coming from the air (i.e. liquid layer) can help to screen out the charge.

Moving the tip along the silica surface with a potential applied also gives the same charging. The tip was moved along two circles shown in green in Fig.2.17-1. The result can be seen in Fig.2.17-2 with the colours adjusted, so one can see the effect clearly (black spots around high objects are artifacts of image processing). The effect of the tip is actually stronger, due to the fact that its sharp shape creates a bigger electric field density near the tip's end.

For the transport properties and carrier scattering in graphene it is important to know the charge density in the surface oxide layer. Although we can clearly see the charging effect, the AFM measurements do not give such quantitative information. By using the spring constant of the tip and its deflection in the static mode one can estimate the total charge but not its distribution in the oxide. Even for the total charge, our estimations have an uncertainty of one order of magnitude since this force is mixed with the other interactions and cannot be clearly separated.

2.7.5 Contamination induced by electric field

Once deposited, the graphite flakes on the surface are open to the environment and can adsorb various substances. The step height of the same flake measured one hour after deposition and repeatedly measured every few days may increase (sometimes up to 1 nm) indicating a few monolayer thick film adsorbed on the surface. Whereas this process seems to have a long-term character, the situation changes if there is a gate voltage applied between the n-Si back gate and a few-layer flake.

The image in Fig.2.18a shows a flake with a single- and few-layer ($\sim$5) regions labeled accordingly. This flake is actually attached to a much bigger piece of graphite ($\sim 100\ \mu m$) which is contacted to a voltage source using conducting silver glue and a thin wire. The gate voltage was applied to the n-Si substrate, keeping the flake and tip grounded. Topography measurements on the silicon dioxide become strongly affected by the electrostatic force, however it is not the case for graphite

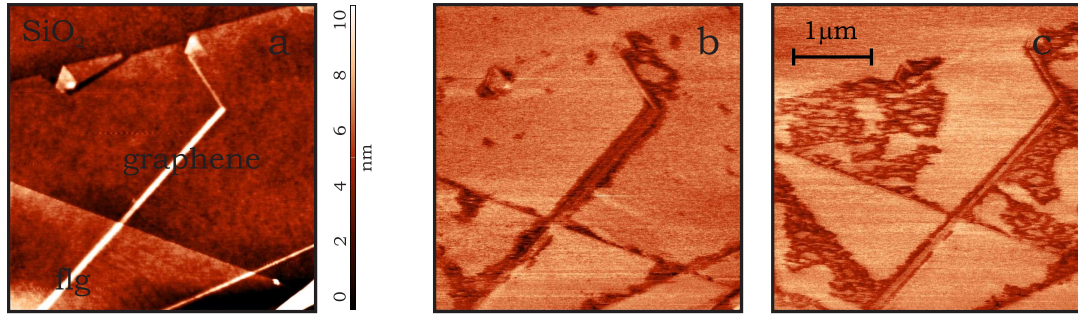

Figure 2.18: Topography of pristine flake (a), phase contrast image of contaminated (b) and heavily contaminated (c) flake. All images have the same scale and were acquired in the same region.

and graphene as they screen out the electric field from the gate.

We detect about 0.5 nm high foreign layer on the surface after the gate voltage was applied for a few minutes and then removed. The deposited material can be seen using both topography and phase techniques, but the phase imaging gives much better contrast, indicating a change in tip-surface interaction when it comes over a contaminated region (e.g. a charge, dipole). The image in Fig.2.18b shows contamination after 5 V was applied to the gate. The deposits can be seen as a dark contrast along the edges, folds and other structural defects. Further experiments with higher gate voltages, Fig.2.18c, introduce even more contamination, which changes its structure depending on voltage, time and ambient conditions, always 'growing' from the defects.

This qualitative experiment shows that even for simple room temperature measurements involving the gate voltage the measurements need to be done in a clean and inert atmosphere. Although these contaminations were later removed by annealing at 400°C in argon/hydrogen, all the measurements discussed in this project were carried out in helium or vacuum conditions, unless otherwise stated.

2.7.6 Contamination after fabrication and annealing

During the contact fabrication, a number of chemical compounds are in contact with the graphene surface. Although this procedure will be discussed later in detail, the effect caused to the surface needs separate consideration. The chemicals used in fabrication are:

- PMMA (poly-methyl methacrylate),

- anisole (resist solvent),
- acetone,
- isopropanol.

We have observed that SiO_2 and graphene become significantly contaminated (this was checked on several samples). The image 2.19a shows the flake topography before and 2.19b – after the contact fabrication. For this sample, the roughness of the oxide increases twice from 0.25 to 0.5 nm rms, and graphene's even more – from 0.2 to 0.8 nm rms. The step height measured across the flake edge also increases from its normal value of ∼1 nm to 2 nm, therefore the graphene is more attractive for the contaminants and adsorbs at least a 1 nm thicker layer.

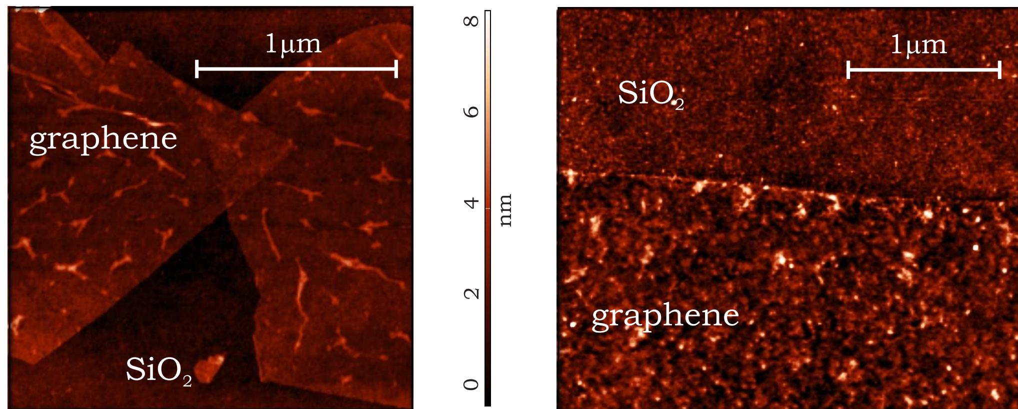

Figure 2.19: Topography of a pristine graphene flake on silica (left) and a sample which passed the conventional contact fabrication procedure (right).

In order to clean the processing residues we use two different annealing methods. The first is 'low temperature' annealing devised by the Manchester group and currently widely used by many people studying graphene. The sample is heated up to $\simeq 150°$ in a clean helium or high vacuum (10^{-5} mbar) environment. The duration of the annealing depends on the sample and is usually determined by the saturation in the sample resistance, which is monitored during the process (∼ few hours).

An example of the sample topography after this annealing is shown in Fig.2.20a. Instead of a uniform layer one can see a surface with randomly placed objects, which cannot be changed by longer annealing. A line scan from the colour-scale indicated by a horizontal dashed line is shown in Fig.2.20b. Since the lateral size of the surface objects is limited by the tip size, we measure their height which appears to

be $\sim 2-5$ nm and very close to the PMMA molecule size. As indicated in Fig.2.20b the step height recovers the initial value, equal to 0.8 nm for this flake. Roughness analysis for SiO_2 gives 0.35 nm rms, with is closer to the 'clean' value of 0.25 nm given in table Fig.2.20d. The height histogram for graphene is no longer a single Gaussian but a combination of a Gaussian and an odd-shaped peak introduced by the PMMA residue. The rms value of 1.3 nm is actually bigger than for a not annealed flake, due to the fact that the removed contaminations were adsorbed in the gaps between PMMA molecules resulting in an apparently flatter surface. The edges of the flakes seem to always collect bigger amount of contaminants, because the binding energies for the edge sites are higher than for the basal plane.

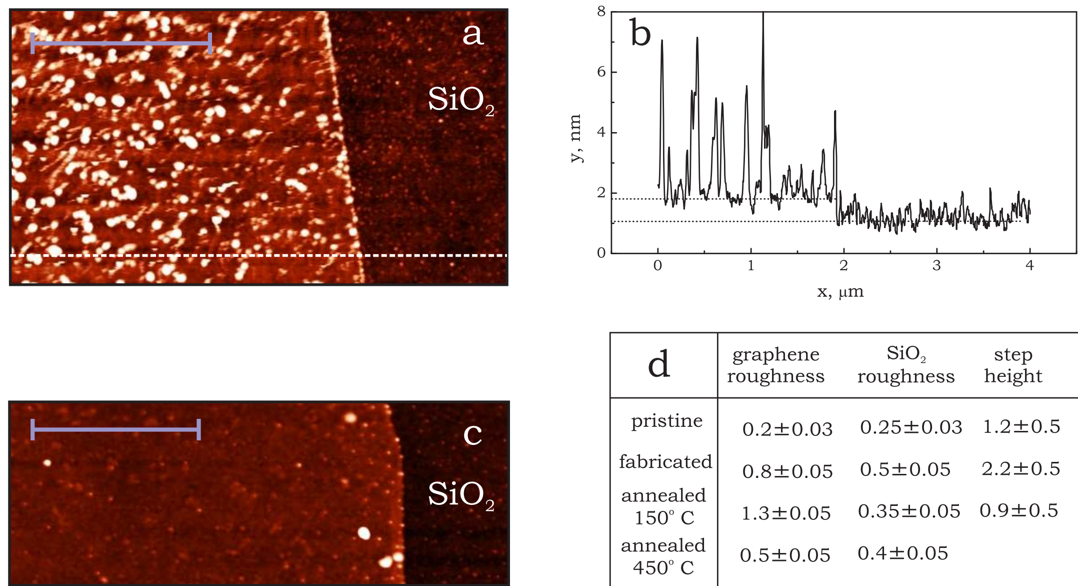

d	graphene roughness	SiO_2 roughness	step height
pristine	0.2±0.03	0.25±0.03	1.2±0.5
fabricated	0.8±0.05	0.5±0.05	2.2±0.5
annealed 150° C	1.3±0.05	0.35±0.05	0.9±0.5
annealed 450° C	0.5±0.05	0.4±0.05	

Figure 2.20: Effect of annealing on topography of graphene devices: (a) a sample annealed in helium at 150° C; (b) single line scan showed as the white dashed line in (a); (c) annealed in Ar/H_2 mixture at 400° C; (d) summary table for topography measurements. Scale bar is 1 μm.

'High temperature' annealing utilises the high temperature reaction between hydrogen and unsaturated hydrocarbons. It was shown [51] that indeed heating graphene flakes up to 400° C in a hydrogen/argon mixture efficiently removes PMMA contamination. In order to try this technique we constructed a simple annealer out of a glass tube and a heater element. The 99.999% pure hydrogen/argon (5:95) gas mixture was constantly supplied to the glass reaction tube through a PTFE tube from the gas cylinder and exhausted through a liquid scrubber to prevent back-streaming. Samples were placed into a holder made of gold coated magnetic

stainless steel and transfered into the middle of the reaction tube by a bar magnet. The volume was then purged for 1-2 hours and then gradually heated up to $\sim 350°$ C.

The image in Fig.2.20d shows a graphene flake annealed in H_2/Ar for three hours. We have observed the absence of the majority of PMMA molecules, although some traces of them can be still seen on the surface. However, we have not studied this procedure in detail since it does not appear to improve the transport properties of graphene.

2.8 Conclusion

This chapter describes materials and methods used for obtaining graphene flakes. For conventional atmospheric deposition, the presence of adsorbed species on both graphene and oxide surfaces was discussed. It was shown that, taking into account water adsorbed both on the silica and graphite surface prior to their direct contact (deposition procedure), there will be always a few monolayers of water between deposited graphene and silica (under normal atmospheric conditions). Other gaseous contaminants can also be trapped together with the water layer, and will not be removed by conventional annealing, and their effect on the charge transport is unclear.

In the second part a number of AFM experiments were presented. In particular we confirm that the roughness of a monolayer flake follows the roughness of the oxide layer, as was previously mentioned in [50, 51]. Also we have demonstrated that the electric field used for driving the carrier concentration in the transistor graphene structures significantly modifies the trapped charge density in the oxide layer. As a consequence, it is not correct to estimate with the surface charge density of the unaffected SiO_2, when considering the charge inhomogeneity [12] and the carrier scattering [19] in graphene.

Finally, the effect of fabrication and two types of annealing on the graphene topography is shown. We see a few nanometer thick adsorbed layer of different compounds used in the device fabrication procedure. Conventional 150° annealing helps to remove most of these chemicals, leaving only similar 4-8 nm high objects which are the PMMA molecules. These molecules can be removed by the second step of the high temperature annealing in an Ag/H_2 gas mixture.

Chapter 3

Device Fabrication

3.1 Introduction

This chapter is dedicated to device fabrication and will mainly consider the technical side of it. Most of the methods used for device fabrication were developed in the semiconductor industry more than 10 years ago and successfully applied to graphene.

Due to the current state-of-the-art graphene fabrication, the final transport properties of each sample are determined by a number of factors which either can not be controlled directly or are not clearly established yet. Thus, there is always a random element in fabrication, for instance the carrier mobility of two graphene samples fabricated together under exactly the same conditions may differ by as much as a factor of two. Consequently, each experiment should be repeated on several samples to exclude sample dependent artifacts and uncertainties.

Therefore, all the samples were fabricated in groups of 5-15 items, which I will refer to as "generations". Each generation was assigned for a particular experiment. Overall, during this project over 200 samples were fabricated (24 generations), with the yield of 10% to 90% strongly dependent on the actual fabrication process. The average time it takes to fabricate one generation is one to four weeks, covering at least one year in total for fabricating all the generations.

For reason of efficiency, most of the processing stages were done for the whole generation simultaneously. To exclude a random mistake, one sample was selected and marked as "satellite". This sample goes through the fabrication routine first, and when its quality is confirmed the rest can be treated in exactly the same way.

This method helps to prevent the situation when one month of work on one generation perishes due to a systematic mistake.

3.2 Electron Beam Lithography

Electron beam lithography (EBL) is a technology which allows one to transfer a pattern from computer memory to a surface by means of electron beam irradiation. Usually the pattern is not transfered directly but through a thin layer of sensitive resist which then acts as a mask for a further processing. The clear advantages of EBL (in contrast to optical lithography) is the less impact of electron diffraction, allowing for a high resolution (down to a few nanometers) and the ability to design and modify the pattern using an ordinary PC. However, there are disadvantages – low production output (which is usually not a problem for research applications) and relatively high equipment price. The following paragraph will start with a discussion on EBL in general followed by a more specific consideration of the system used in this project.

An electron beam system usually consists of three main blocks – an electron beam column (with vacuum sample chamber), driving electronics and a computer. The schematic in Fig.3.1 shows the main parts of an e-beam column. Electrons emitted from a cathode are accelerated by an electric field to a kinetic energy of 5 - 100 keV. Following this, the condenser lens collects emitted electrons and forms them into a beam. After that the beam enters a set of lenses which adjusts the focal plane and focuses it, including also stigmatism correction if the beam crossection has an elleptical shape. Electron lenses can be either electrostatic or magnetic, but the latter gives a better aberration and is used widely.

One of the main resolution limiting factors of electron optics is the lens' spherical aberration, which increases with increasing beam spread angle [53]. Clearly, blanking off a part of the electron beam will affect the total current and time consumption for large exposures, so, usually, the aperture can be changed to give either higher resolution or bigger beam current. Similarly, a hole aperture and an electrostatic deflector are used as a shutter to blank the beam completely and prevent unwanted exposure when it is necessary.

The next part, the deflector, performs scanning of the surface. When the beam

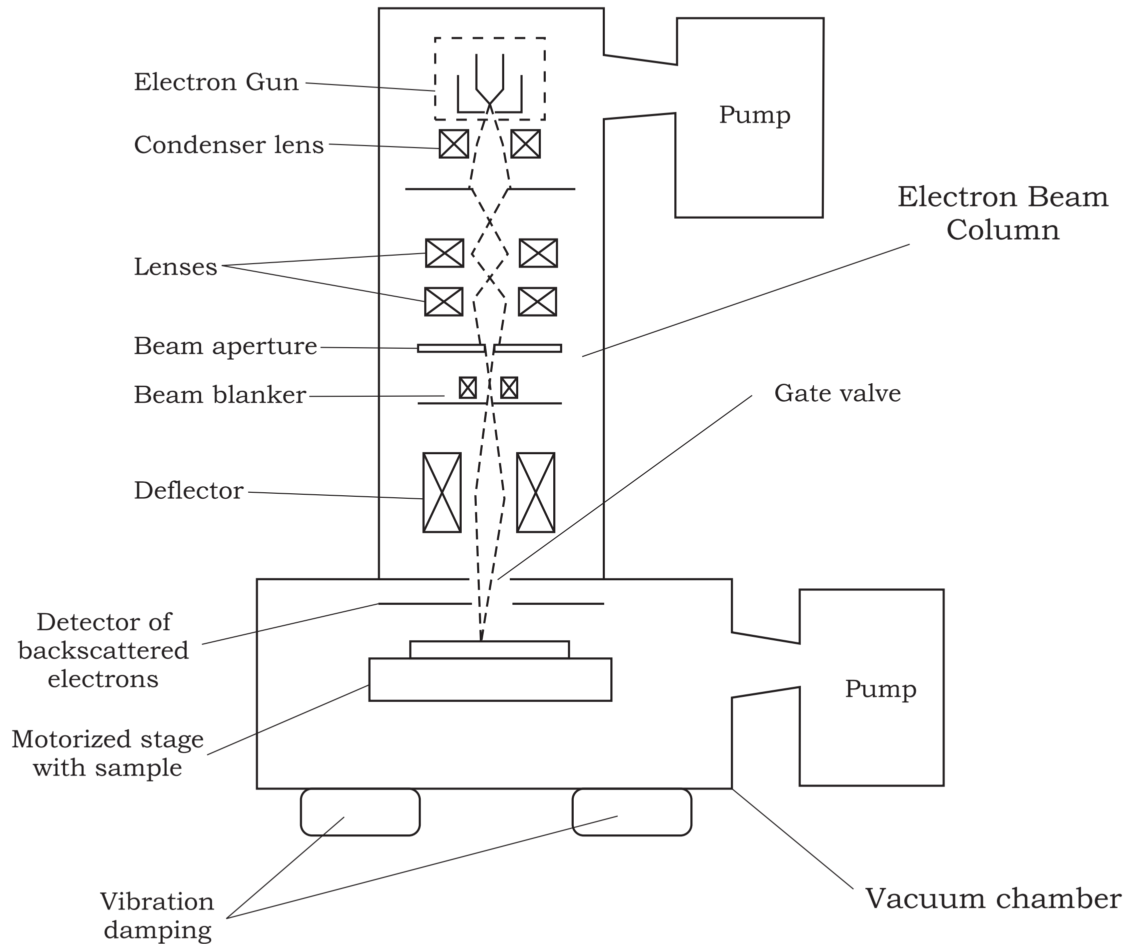

Figure 3.1: Schematic of an electron beam microscope.

hits a surface it scatters back, and the reflected electrons can be detected with a detector. Thus, scanning the surface and reading the detector response for each point gives the Scanning Electron Microscopy technique.

Samples can be loaded in two ways – most specialized EBL machines have an intermediate vacuum port which can be evacuated separately. This method allows to keep main vacuum chamber clean and takes less time to pump down a relatively small loading bay. Alternatively, some combined SEM-EBL systems allow the vacuum chamber to be opened and the sample loaded directly, temporarily shutting off the electron beam column with a gate valve.

In order to work with large samples (bigger than the maximal deflection of the beam) the chamber is equipped with a motorized stage. This stage also has a current detector, so the current of absorbed electrons can be measured in situ.

3.3 Elphy quantum. Exposure logistics

Most of the EBL was done on a dual-beam microscope from the Nova family (NovaLab 400) produced by FEI Company. Two independent columns – electron beam and focused ion beam (FIB) – are positioned at an angle of 52° to each other to make simultaneous writing and imaging using both beams possible. However, FIB was not used in this project because the high energy Ga^+ ions it uses can easily damage our graphene samples and the underlying substrate. The presence of the FIB column does not affect SEM performance, so it can be excluded from further discussion.

The electron beam column of this system (XL30 "Sirion") has a Schottky field emission electron source (SFEG), which utilises a hybrid technology of thermal and field emission and therefore has good stability, relatively small source size and high brightness. It allows the use of an acceleration potential in the range from 1 to 30 kV and a beam current from 5 pA to 25 nA stable to better than 0.5% per hour. However, switching the acceleration voltage may cause transient drifts of the beam position and therefore the system needs some time (depending on the type of exposure) to settle down after the voltage has been changed.

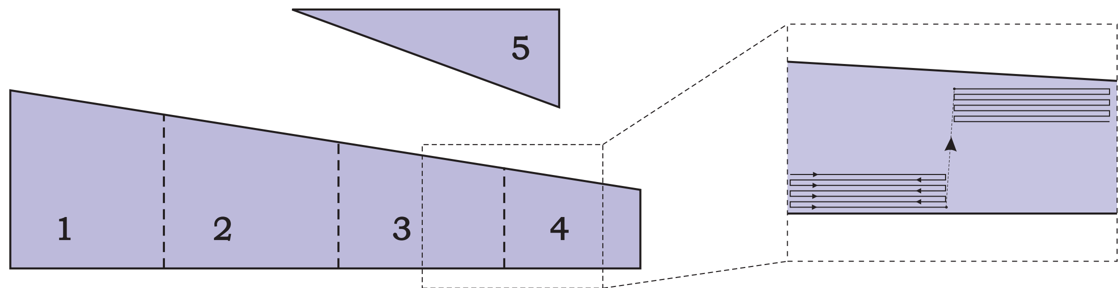

Figure 3.2: Pattern fragmentation before the exposure. Numbers shown default left-to-right exposure order.

In order to adapt this microscope for EBL, a special system called Elphy Quantum from the Raith Gmbh company has been used. It is a universal lithography system which consists of a scan generator electronic hardware and a PC-based operating software. This system takes control of the following parts of e-beam column: deflectors, detectors, beam blanker and the motorized stage. Elphy Quantum is a 'vector' EBL system, which means that it only scans over the places to be patterned, in contrast to a 'raster' system, which scans everything and uses a beam blanker to

control the exposure.

An exposure pattern can be designed either with the internal editor or can be loaded from a vector .dxf file created previously using an editor of choice. The software splits the loaded pattern into a number of simple shapes (trapeziums and triangles) as shown in Fig.(3.2) and sends them one by one to the pattern generator hardware. The pattern generator creates an array of points out of these primitive shapes and feeds this array to DACs which drive the current through the deflector coils (two DACs for x and y direction). Thus, it is actually a point-by-point scan with a step size $l_{st} = L_{wf}/2^{16}$, where L_{wf} is the full beam deflection called Write Field (WF) size and 2^{16} comes from the bit capacity of the DACs. The area $L_{wf} \times L_{wf}$ should be chosen so it contains the whole pattern, but sometimes the pattern can be split into a few WF in order to get a higher accuracy for certain regions. Traveling between the centers of WF regions can be done using the motorized stage. The full dose can be calculated as

$$D = \frac{It_{dw}}{l_{st}^2} \qquad \left[\frac{\mu\text{C}}{\text{cm}^2}\right],$$

where I is the beam current, t_{dw} the point dwell time, $I \cdot t_{dw}$ the charge obtained by one pixel. For this system the dwell time has a limit of 400 ns, mainly because of the limited speed of data transfer between the pattern generator and DAC. The inductance of the deflector coils also adds a restriction – it limits the beam speed (speed of the spot traveling along the surface) to 10 m/s.

For the conventional PMMA resist used the exposure dose D varies in the range of $100 - 400$ μC/cm^2 depending on different factors, that will be discussed later. An example of Elphy Quantum exposure logistic is shown in Fig.(3.2). The normal exposure sequence for this pattern will be $1 \to 2 \to 5 \to 3 \to 4$ as the software 'reads' the structure from left to right. However, sometimes the exposure may take a long time (up to a few hours), and drifts in electron optics or thermal drifts of the sample holder may lead to a shift between parts 2 and 3 caused during exposure of part 5. This can cause gaps (overlaps) to appear in integral structures and can be partially solved by changing the exposure sequence manually ($1 \to 2 \to 3 \to 4 \to 5$) or writing with a slightly unfocused beam. Nevertheless, the best option would be giving a sufficient settling time before the exposure (after the sample reload or gun voltage change).

3.4 Spatial energy distribution. Proximity effect.

It is common to use a Gaussian function for the approximation of the incident beam energy distribution. The factors limiting the spot size are discussed in detail in [54] and often cannot be improved without modification of the electron beam column. The real size of the beam for the XL30 is much larger than the wavelength of electrons ($\lambda_e = 0.012$nm for 10 kV beam) and in the best case can be optimised to be as small as 10 nm.

When electrons enter a solid they experience different scattering events. Scattering can be roughly divided into two types: small angle scattering called *forward scattering* and large angle scattering – *backscattering*. During their path through a solid, initial electrons lose their energy, creating secondary electrons, UV and heat. The secondary electrons have smaller energy ($\sim 1 - 10$ eV) and short paths (up to 10 nm). However they are responsible for the actual resist exposure due to their large number, and thus limit the minimal feature size for PMMA to be $\sim 5 - 10$ nm.

Both forward- and backscattered electrons are usually described by a sum of two gaussians [55]:

$$f(r, z) = a_1 \exp\left[-r^2/\beta_f^2(z)\right] + a_2 \exp\left[-r^2/\beta_b^2(z)\right], \tag{3.1}$$

where $\beta_f^2(z), \beta_b^2(z)$ are variances describing the width of the two contributions, whilst a_1 and a_2 are coefficients.

Monte Carlo simulations done by Kyser et. al [56] show trajectories of electrons injected at one point in a PMMA/Si bilayer substrate for two different acceleration voltages. Forward scattering is responsible for beam broadening when it passes through the PMMA layer, and it has a smaller impact on faster electrons. In fact, a pattern exposed with 30 kV beam has almost vertical sidewalls after development, when 10 kV gives significant undercut profile (sometimes up to 45°). Such undercut profile becomes important on the stage of the metal deposition/lift-off. On the other hand, 10 kV beam suffers more from external electromagnetic fields and therefore it has bigger beam noise/drift and slightly larger minimal spot size.

The size of the backscattered electrons distribution $\beta_b(z)$ also strongly depends on the beam energy – it gets wider with increasing energy. The broadening of the beam distribution is accompanied by a decrease in the dose per unit area a_2, since the

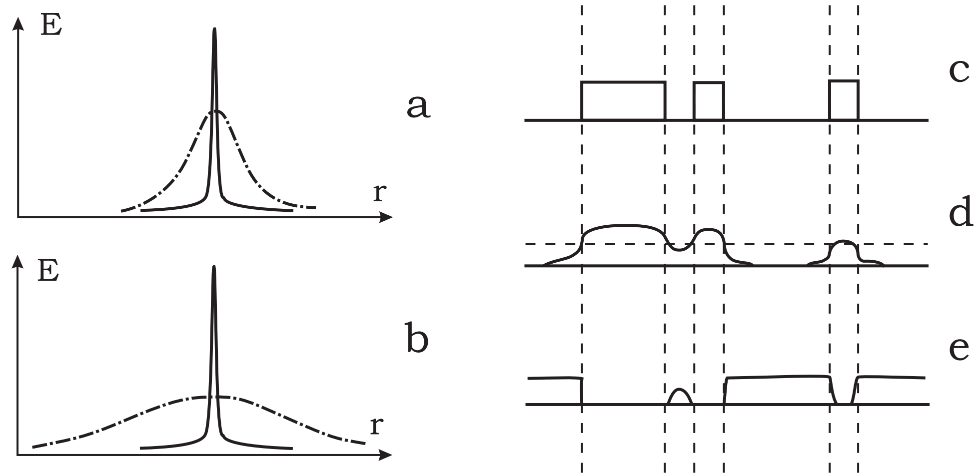

Figure 3.3: Gaussian contribution from forward scattering (solid line) and back-scattering (dashed dot line) for low (a) and high (b) beam energy. Proximity effect: initial pattern (c), actual dose distribution (d) and profile of developed resist (e).

total amount of backscattered electrons is almost independent of beam energy [57] and depends mainly on atomic number of the substrate material. Backscattered electrons still have high energy, and some of them can leave the material and be detected, making it possible to see substrate features (alignment marks, defects) 'through' the resist layer. The average depth of electron penetration in Si is 2 μm and 10 μm for 10 and 30 kV beams, respectively [54].

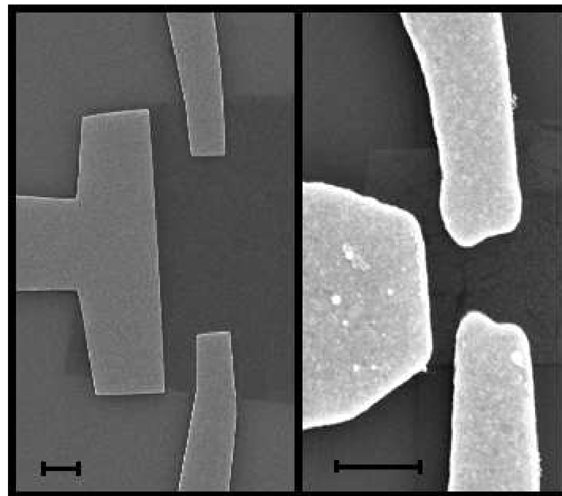

Figure 3.4: Metal contacts to a graphene flake. Left - correct dose distribution and shape, right - distortion due to the proximity effect. Scale bar 1 μm.

When two closely located shapes are exposed, backscattered electrons from one can reach the other patterns and increase their overall dose. This effect is called the proximity effect and is illustrated in Fig.3.3 [57]. The dose distortion – large structures obtain bigger dose in the middle and smaller along the edges, and small

solitary structures can fail to be developed at all. At the same time, exposure of two adjacent structures may remove the gap between them, so often a dose correction is needed. The effect is shown in Fig.3.4 – metal contacts to a graphene flake with a correct dose on the left, in contrast to a distorted (overexposed) shape on the right.

Some EBL systems are equipped with proximity correction software. However, often the dose pattern can be adjusted manually after a few EBL tests. These tests are normally just exposure of lines, dots, gaps in arrays with a dose variation, then development and metalization. During SEM study of the obtained structure, a particular dose should be selected for each line thickness (dot, gap size) and used further. Such calibration was made after every major change in lithography process, i.e. beam voltage, resist type or thickness, change of the development conditions, etc.

3.5 E-beam resists

Electron beam resist is a compound designed for transferring a pattern on a substrate for further processing. Most of the EBL resists are organic polymer materials which change their chemical and physical properties under electron beam irradiation. There are two processes that can happen with a polymer during exposure – chain secession and crosslinking. If the first one dominates, exposed polymer chains become shorter and more soluble, thus can be selectively removed by a solvent called the developer. Such a resist is called positive, as opposed to negative, where chain crosslinking dominates and the exposed pattern becomes harder to remove.

In order to cover a wafer with a thin resist layer, liquid resist is spilled onto the surface and then spun at 500 - 10000 rpm for 10 - 200 sec until it forms a uniformly thick layer. As many EBL resists are solid under normal conditions, they need to be dissolved in a solvent unless the coating method is different (vapour condensation, spray). Once coated, the wafer is baked to drive out all the solvent and make the resist dry and solid.

Normally, the development process involves immersion of the wafer in a developer solution for a certain time and then washing it in another liquid to remove residual developer. Depending on the electron beam dose (other conditions being equal), the exposed resist can remain or be partially/completely removed. Fig.3.5 is a sketch of

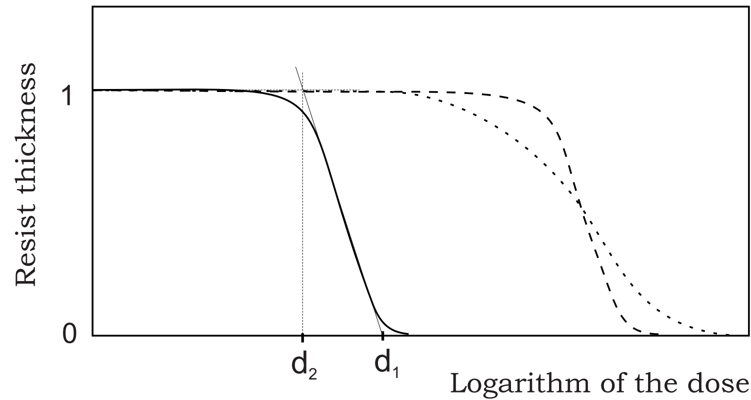

Figure 3.5: Developed resist thickness plotted against exposure dose. Solid line is normal resist; dashed line is the same resist with higher molecular weight, short dashed – with broad distribution of molecular weights.

the dependence of the resist thickness after development on the dose. The dose d_1 sufficient to completely remove the resist is called its sensitivity and d_2 the threshold dose. The contrast $\gamma = 1/(\lg d_1 - \lg d_2)$ describes their difference and gives the idea of EBL limits when patterning small densely packed shapes (due to the proximity effect), and it also has an impact on the edge quality and undercut profile.

These parameters d_1, d_2, γ depend on the following conditions:

- **The choice of resist.** There are dozens of EBL resists commercially available and d_1 may vary more than 100 times among them. Also, for a given resist the change in the the molecular weight of the polymer causes a difference in the sensitivity.
- **Resist thickness.** Electrons can be scattered when penetrating the resist, thus the bottom part of the film may receive a smaller dose.
- **Electron beam energy.** This is significant because a more energetic electron beam is less affected by scattering. Additionally, using a hard wafer causes backscattered electrons to return to the resist film, so **wafer material** should also be considered.
- **Pattern size**. Due to the proximity effect as discussed above.
- **Bake conditions**. A longer and hotter bake makes the resist stronger and denser. Also, residual solvent may cause a change in the resist solubility.

- **Development process**. This includes development time, temperature and developer solution strength.

Among the large number of positive tone resists available at present [54], the most popular are acrylic based polymers, i.e. Poly(methyl methacrylate) (PMMA, also known as Plexiglas or Perspex) and its copolymers and modifications [58]. In addition to dozens of practical applications, it has been showing excellent e-beam performance for more than 30 years [59] and has an extremely high resolution of less than 10 nm [60]. It is also sensitive to deep UV radiation (220 - 250 nm), so hybrid structures can be made where a fine pattern produced by EBL can be combined with large-scale exposure by deep UV light. The size of a single PMMA molecule can reach 10 nm [61], giving yet another limiting factor for its resolution.

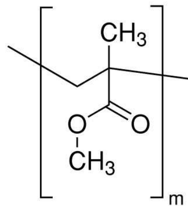

Figure 3.6: Structure of PMMA polymer.

Fig.3.6 shows the structural formula of the PMMA polymer. This clear plastic material has a density of $1.150 - 1.190$ kg/m^3 and is solid under normal conditions. However it can be easily dissolved in different organic solvents (chlorobenzene, anisole, etc.). Resist viscosity can be changed by altering the ratio of solid and liquid, which results in a film thickness difference during spinning. Usually its mass concentration varies from 0.5% to 10% and spin speed from 1000 to 6000 rpm – these conditions give a flat and uniform film of thickness ranging between 25 nm and 2 μm.

As the melting point of PMMA is $120 - 140\,°$C (depending on molecular weight (MW)), baking it at temperatures $\sim 150 - 180\,°$C actually involves two processes: solvent removal ($\sim 100\,°$C) and PMMA phase transition to liquid. The latter improves the film uniformity, making the film surface as flat as $\sim$ 1 nm, removing micro bubbles and helping PMMA to fill in the surface roughnesses. The baking process may take from 60 sec to 1 hour, again depending on the temperature, resist thickness and process requirements.

The mechanism of the chain secession occurring with PMMA during EBL is depicted in Fig.3.7 [62]. Electron or UV radiation breaks one of the C-C bonds, which causes formation of a double bond inside the monomer and chain secession. Just a few breaks per chain is enough to make the resist sufficiently exposed (so it

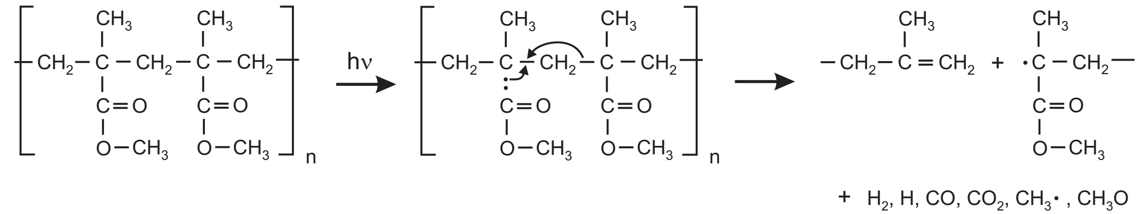

Figure 3.7: PMMA reaction under electron or UV irradiation.

can be developed) [58]. The products of this reaction may adhere to the underlying graphene flake, contributing to the initial doping level of graphene devices. A more detailed discussion of the electron radiation chemistry of PMMA and reaction products can be found in [62].

If PMMA is exposed with an order of magnitude higher dose it will crosslink, forming a polymer network insoluble in acetone and many other organic solvents. Thus, it becomes negative tone resist and can be used as an insulation layer in many technological problems. However, patterning with PMMA in negative tone gives a poor resolution (tens of nm) and introduces contamination if removed without use of aggressive stripping techniques such as oxygen plasma etching or piranha etch treatment.

3.6 Multilayer resist. Development

PMMA is available in molecular weights ranging from 50K to 2.2M [63]. Its resolution is almost constant [60], but its sensitivity d_1 increases with the increase in molecular weight by about 10% between 100K and 950K. The latter allows for the creation of various step height profiles in the resist using two or more layers of PMMA with different chain length.

This technique is widely utilised for controlling undercut profiles, creating Γ- and T-gates [64] and other structures. However, the 10% difference is often not enough, and chemical modification of PMMA is needed to change d_1 more significantly [58]. Copolymer methyl methacrylate -co- methacrylic acid (P(MMA-MAA)) is a convenient substitute for a low molecular weight PMMA, as it requires a few times lower exposure dose (depending on the ratio of MMA and MAA monomers).

Development of PMMA and P(MMA-MAA) resists usually involves immersion of the substrate in a developer solution, often a binary solvent mixture. As a default developer, a solution of MIBK and isopropyl alcohol (IPA) is used. Since MIBK is a stronger solvent, increasing its amount gives a higher sensitivity, i.e. a smaller exposure dose is needed. However, the increase in sensitivity is always accompanied by a decrease in contrast – clean MIBK etches even unexposed PMMA. Two standard ratios [63] are usually used for development – 1:1 and 1:3 (MIBK:IPA) – they differ by two times in sensitivity and by 50% in contrast. Other binary mixtures such as water/IPA, water/MIBK, methylethylketone(MEK)/ethanol, 2-ethoxyethanol/methanol can also be found in the literature. Since resolution (i.e. contrast) was more important than sensitivity ($\propto$ exposure time) during this project, two solutions were used: ultrasound (US) assisted IPA / MIBK / MEK 15:5:1 and water / IPA 3:7 [65] (both providing similar contrast).

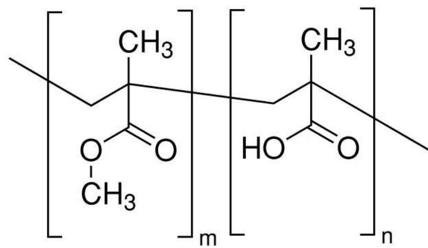

Figure 3.8: Structure of the P(MMA-MAA) copolymer.

It was also reported (see refs in [65]) that ultrasonically (US) assisted development enhances contrast and helps to remove undeveloped islands from the bottom of the lithographically-defined trench. In fact, the contact resistance of the graphene-metal interface becomes smaller with US assisted development, indicating that the US treatment helps to remove residual PMMA from the graphene surface, therefore increasing the effective contact area. This method of development also helps to define structures with high aspect ratio (e.g. deep and narrow channels), due to the micro-streams induced by US waves in the liquid.

3.7 Metalization. Undercut profile. Lift-off

Metalization, used for the fabrication of contacts and gates, involves deposition of a metal layer. Among the variety of metal deposition methods [55], thermal evaporation is the simplest, and is the one used in this project.

Edwards E306 single-source thermal evaporator uses a simple principle of passing a high current (up to 50 A) through a tungsten filament basket with a source material

inside. As the source metal gets hot, it starts to emit atoms or few-atom clusters. The vacuum ($\sim 5 \cdot 10^{-6}$ mbar) allows these particles to travel directly to the target substrate, where they condense back to a solid state. The vacuum is maintained with a diffusion pump, using a nitrogen trap to prevent oil backstreaming to the main chamber.

As for most graphene devices reported in the literature, a Cr/Au metal bilayer was used for contacts (and also gates). The bottom Cr layer plays the role of an adhesion layer between gold and silica and is normally 3-10 nm thick. As chromium immediately gets oxidized in the presence of oxygen, it must be covered with the subsequent gold layer in high vacuum (pressure lower than 10^{-5} mbar). The gold layer can be 20 - 250 nm thick, depending on the device application. Normally, a standard graphene device has to have more than 80 nm total bilayer thickness for comfortable wire bonding (in the later stages of sample packaging). However, markers and labels can be only 20 nm thick and suspended bridges (see Chapter 5) require 250 nm thick gold film for mechanical stability.

The Cr/Au bilayer grows as a continuous polycrystalline film with an average grain size $\sim 5 - 40$ nm depending on substrate temperature, evaporation speed and method of evaporation. We normally see $\sim$ 20 nm grains (SEM, AFM) accrete together, and the top surface roughness does not exceed a couple of nanometers. The overall resistance of the gold film contacts is $< 10\ \Omega$ and is negligible compared to metal-graphene interface resistance (several hundred Ohms for a conventional sample described later).

The evaporator was modified so that it can carry two sources by installing an additional filament, vacuum feedthroughs and a high current switch. The distance between the two filaments is approximately 15 mm and the substrate is placed $\sim$ 30 cm away from them, so the incident beam angle between the two sources has a difference of about $2.8°$, giving an insignificant shadow misplacement of a few nanometers between the Au and Cr spots. However, when working with narrow channels in a thick resist, e.g. 100 nm lines in 600 nm resist as for suspended gates, Cr and Au lines can be $\sim$ 30 nm misplaced. Often this effect can be eliminated by rotation of the substrate so the line connecting two sources is parallel to the lithography channel direction.

The growth rate is controlled manually by increasing the current through the

filament, and normally it is kept ∼ 1 Å/sec for chromium and ∼ 2 Å/sec for gold. A significant increase in the growth rate may influence the quality of the film, and a decrease can lead to overheating of the substrate and thermal expansion of the polymer film, resulting in a distortion of the pattern.

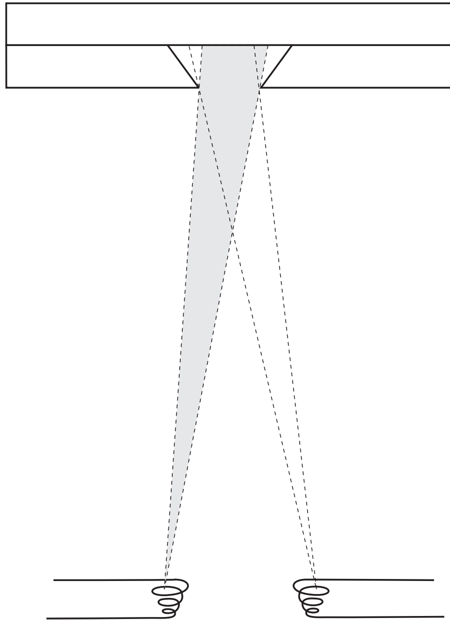

Figure 3.9: Illustration of the 'shadow' effect during metal evaporation using two sources.

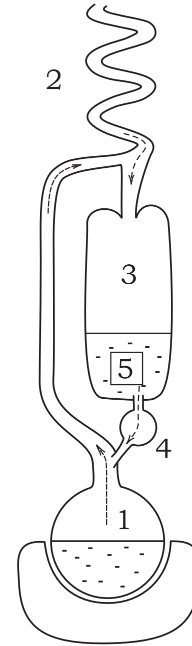

Figure 3.10: Lift-off in the acetone distiller.

After metalization, substrates are placed in acetone. Starting from the wafer edge, the acetone dissolves the PMMA layer and the metal film peels off where it is not attached directly to the substrate. This procedure is called lift-off and normally takes several hours. Acetone does not decompose PMMA but only dissolves it, and often PMMA molecules adhere to a surface and stay there after the lift-off. These molecules can be seen using AFM, as they are quite big (∼ 5 nm). Usually PMMA residue can be removed by oxygen plasma ashing or further chemical treatment. Most of the cleaning methods however are not suitable for our purposes as they can easily damage graphene.

Heating the acetone can hasten the lift-off process since it becomes more active. Also, hot acetone leaves less PMMA residue according to our AFM tests. In Fig.3.10 one can see the device used for the lift-off process. Hot acetone vapour from the bottom vessel (1) goes to the condenser (2). The resulting clean liquid comes into the sample space (3). When the liquid level in the sample space reaches a certain

level, valve (4) opens and release the liquid back to the hot chamber, leaving a small amount of liquid to keep the sample (5) always wet. It repeats the circle approximately 5-10 times per hour, flushing the sample with clean acetone. The temperature in the sample space depends on the boiling intensity in the vessel (1) and can be tuned in the range $\sim 30 - 45$°C. We normally keep it below 35°C as a surface modification was detected (using AFM) after a graphene sample was placed in boiling acetone.

3.8 Packaging and bonding

When the sample is taken out of acetone (through IPA and N_2 dried) it can be mounted onto a leadless chip carrier (from here on referred to as a 'package' for simplicity). The package is made of a ceramic material with Ni/Au plated areas. It has a square recess in the middle for a sample and two sets of contact pads connected together: one looking inside of the cavity, Fig.3.11, the second outside on the bottom of the package, Fig.3.11. The wafer is glued inside with silver 'dag' – a colloidal solution of fine silver powder in an organic solvent. It creates an electrical contact between the metal cavity on the package and the sides of the n-doped Si wafer (which serves as a back-gate for the graphene flake).

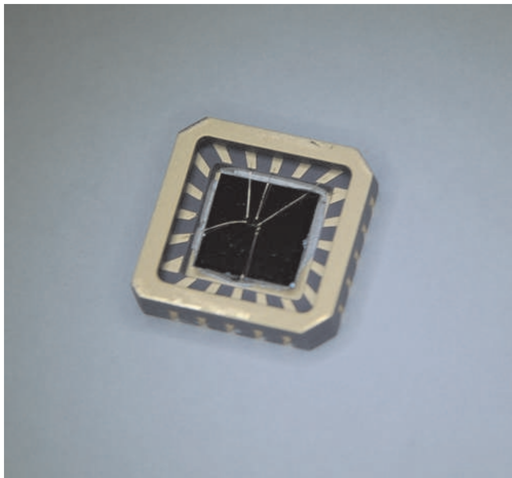

Figure 3.11: A piece of silicon wafer with a graphene sample glued and bonded to a package.

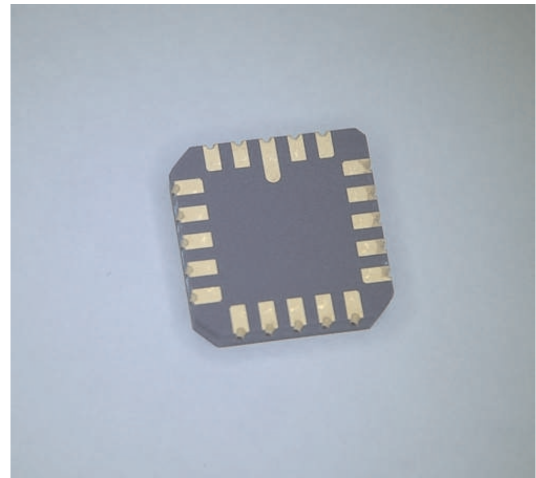

Figure 3.12: Back side of the package for the further electrical connections.

Within about ten minutes the sample is firmly attached to the package. Then we interconnect the EBL defined contacts on the wafer with the contact pads on the

package, using a Kulicke & Soffa ultrasonic wedge bonder. The linking gold wire is 25 μm thick and can be seen in Fig.3.11. Measuring equipment then needs to be connected to the firm contacts on the bottom of the package (Fig.3.12) as will be explained later.

Using the ultrasound wedge bonder requires the metal thickness to be more than 50 nm and a sufficiently thick oxide layer (more than 200 nm) to sustain an ultrasound pulse which smashes the gold wire into the contact pad. For the case when a US bonder is not applicable, interconnections can be glued using the same silver dag.

3.9 "Old" fabrication route

In order to match the contact pattern and a graphene flake during EBL, one needs to have alignment markers on the surface. The further away these markers are from the flake, the bigger the misalignment that can occur. Assuming the maximal positioning error to be within 100 nm, the markers should be placed not further than 100 μm for the EBL system used. As the deposition of graphene is a random process, these markers should cover considerable area on the surface.

Any metal spots thicker than 10 nm on SiO_2 can be seen in SEM through a normal PMMA layer, so the common practice to do aligned EBL involves initial patterning of the surface with equally spaced grid of labels by means of electron beam, optical or mechanical contact mask lithography.

The following technological route shown in Fig.3.13 is the standard procedure used by most of the people who do patterning aligned to a randomly located object (graphene flake in this case).

As the wafers can be contaminated during shipping/handling they are first cleaned. Taking into account that the lithography routine also introduces contamination to the surface, the next move can be different. First option is to deposit graphene on a pristine wafer and then do both lithographic cycles (markers and contacts). Second is to pattern markers first, clean the substrate and do graphene deposition followed by second lithography cycle for the contacts. It is generally known that using optical lithography for markers will introduce much higher level of resist residue contamination which is especially difficult to get rid of, without

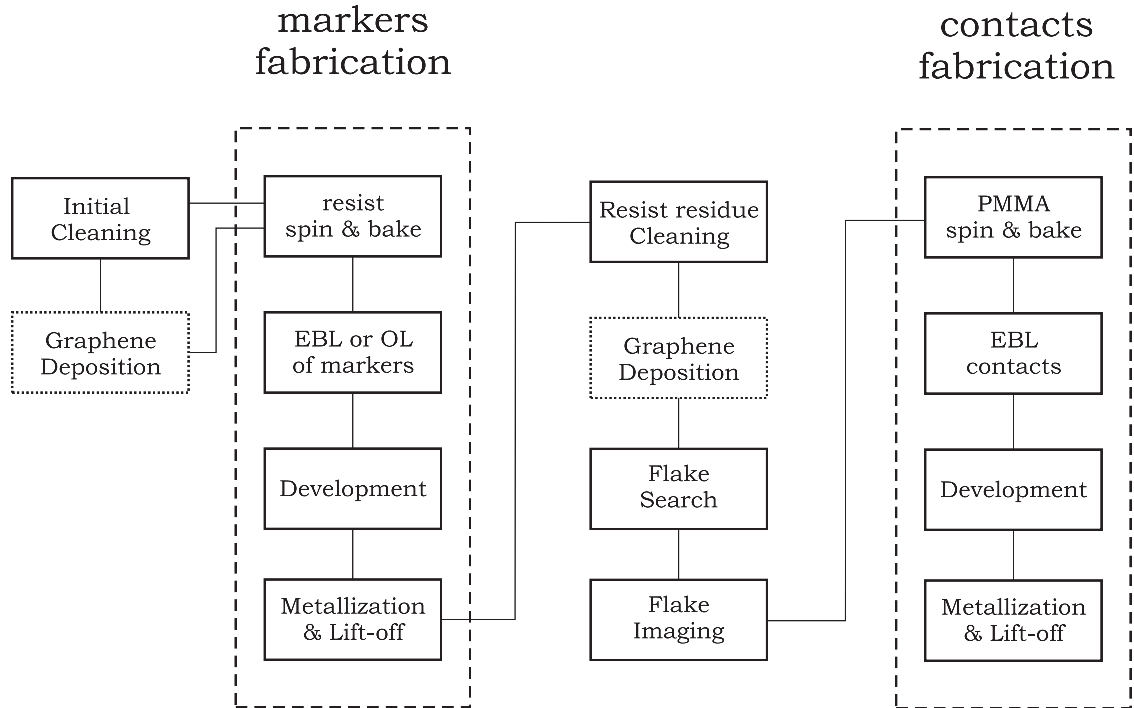

Figure 3.13: Standard technological route. Dotted block can be placed in any of two positions.

involving aggressive oxidants or plasma ashing in the process.

After the markers have been deposited, an image of the flake and the four nearest labels must be taken. It will then be used for the contact pattern design and contact EBL alignment according to the position of these four labels. SEM can be used for taking this picture with a small exposure dose. It gives a good resolution (down to 10 nm) image, however the whole flake will be exposed by electrons. To prevent unnecessary exposure and possible damage of the flake optical imaging can be used. Due to the diffraction limit, all the contours on such an image will be $\sim$ 500 nm smeared, however a careful approach can give positioning accuracy within 100-200 nm.

3.10 "New" fabrication route

The following route (Fig.3.14) that came as a substitution for the old one, utilises the fact that holes developed in PMMA for markers deposition (before metalization) have a good contrast in SEM so they can be used as the actual markers. It has a number of advantages, which can be listed as follows:

- *Lesser possibility to have contamination under the flake.* Graphene is deposited

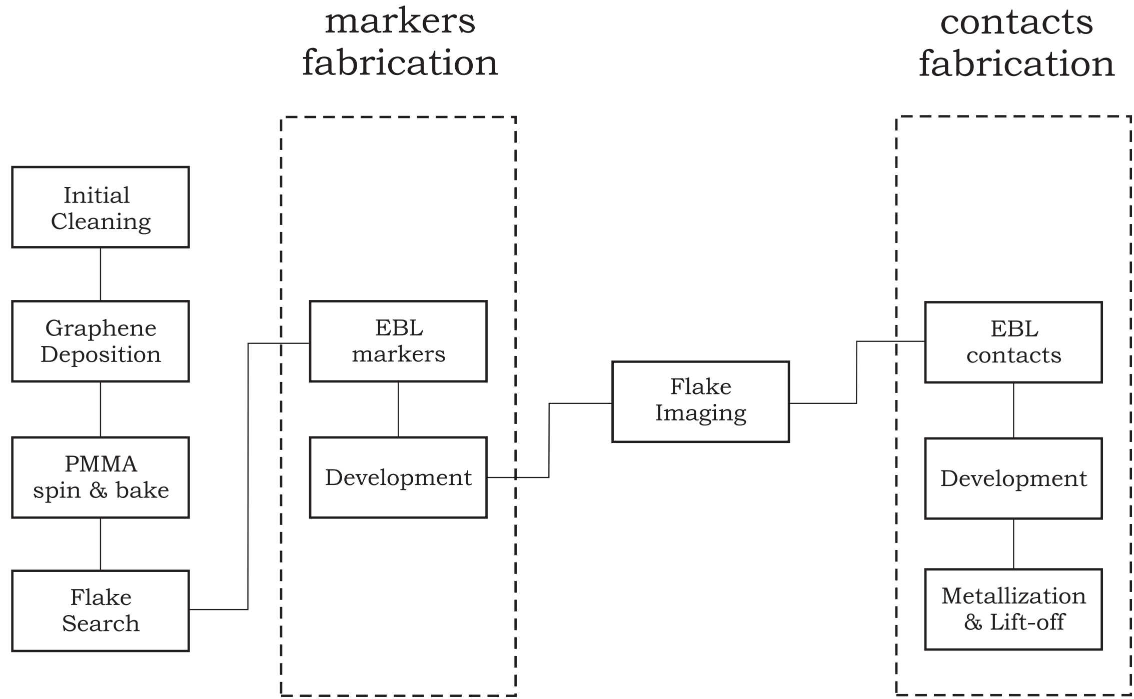

Figure 3.14: Second technological route.

on a clean wafer with no treatment done to it except the first cleaning.

- *Lesser amount of adsorbed material on the flake.* After the flake deposition, the surface can be immediately coated with PMMA. The fact that flakes can be seen though the PMMA layer in an optical microscope allows one to minimize the time the sample is exposed to the ambient conditions. The next time the flakes will have a contact with the environment is on the packaging & bonding stage.

- *Overall process is simpler and faster* – metalization and lift-off are done only once.

At present, the fabrication of a group of 10 Hall-bar type samples from the initial wafer cutting to the last bonding stage would normally take about 10 working days, assuming no problems happen at any fabrication stage.

3.11 Example of graphene Hall-bar fabrication

An example of the fabrication of a graphene sample is given here to summarize all the stages listed above.

We start with a graphene flake deposited and located on a 20 mm wafer under a layer of PMMA. Simply because this size is not convenient for wafer handling, the piece of wafer is trimmed to 4x4 mm with the flake being roughly in the middle. This wafer size will also fit into the sample package cavity (which is 5x5 mm big), so no further cutting will be required.

Cutting is done using a manual scriber with a diamond blade tool. It creates a scratch parallel to one of the wafer crystal directions and a modest force is then applied to brake the wafer along the scratch.

After this the wafer is placed into a specially made EBL holder, which can carry up to 8 samples using a simple set of small metal screws. Pushing against the wafer side, these screws create a conductive link between the wafer and the sample holder so there is no charge accumulation during EBL. Using an adhesive tape on this stage is inadvisable as it may leave glue residue on the wafer bottom, which later will be dissolved and spread on the sample. The second argument against the tape is that it can have a built-in stress and the latter gives a slow, long-term drift as it relaxes.

The EBL holder is then loaded into the electron beam microscope for the markers lithography. Markers are placed as a square array of crosses with a pitch of 100 μm, forming a coordinate system. The origin of this coordinate system as well as a few distinct points in the corners of the wafer are labeled with large features so they can be easily seen in a microscope with a small magnification. Exposing this grid over a 4 mm square wafer normally takes about 1 hour.

Development of the markers can be done in any developer listed above as their exact shape is not important. An optical image of the uncovered flake on 275 nm oxide is depicted in Fig.3.16. The initial oxide colour turns to green as $\sim$100 nm of PMMA is spun on top. However, it does not have a significant impact on the flake visibility. The same flake covered with PMMA between 4 nearest crosses is shown in Fig.3.16. After the latter image is taken and the coordinate of the bottom-left cross written down, it can be loaded back into EBL. In the meantime the drawing of the contacts will be created as explained below.

After the image was loaded to a vector redactor, it is rescaled and rotated. A new coordinate system is formed using positions of the four crosses (Fig.3.17), with the origin located between the four nearest crosses.

As was explained earlier, using a smaller write-field size for EBL yields better

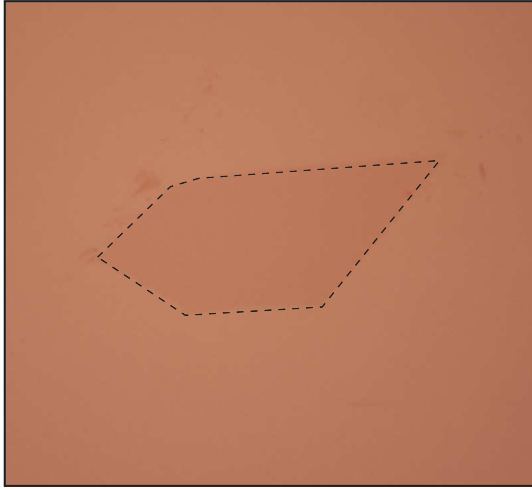

Figure 3.15: Optical image of uncovered flake on 275 nm silicon dioxide surface (in white light).

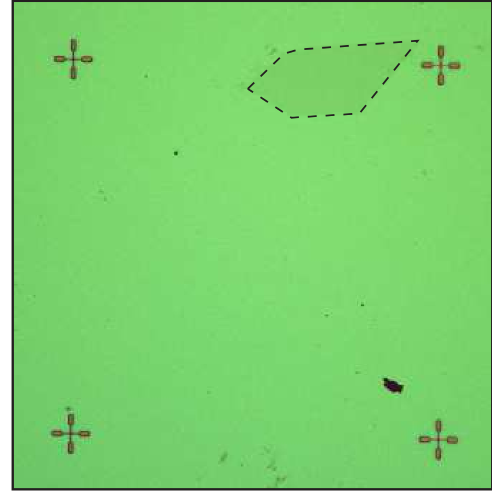

Figure 3.16: Optical image of the flake covered with $\sim$ 100 nm PMMA layer and the 4 nearest crosses (green light).

accuracy and resolution. Thus, to keep the error within ±100 nm, we choose a 125×125 μm write-field size. The small exposure area also allows one to use the smallest beam current available (smallest size aperture, see above) and focus the beam down to a 20 nm spot size.

As 125 μm is too small for bonding, the second set of contacts of a bigger size is placed within a 800×800 μm WF encompassing the first 'small' one. Fig. 3.17 shows a typical drawing for the contacts superimposed on the original image Fig. 3.16. Two different WF are shown as black squares containing two sets of contacts - red for smaller and blue for the large contacts.

The image is then saved in a .dxf format and transferred to the lithography software. The following details can be given for 30 kV exposure for both types of the contacts:

- write field 125 μm
- beam current 32 pA
- area dose 365 μAs/cm^2
- step size 4 nm
- dwell time 0.001391 ms

- write field 800 μm
- beam current 20 nA
- area dose 340 μAs/cm^2
- step size 12.5 nm
- dwell time 0.001645 ms

The area dose may vary ±20% to account for the proximity effect, depending on

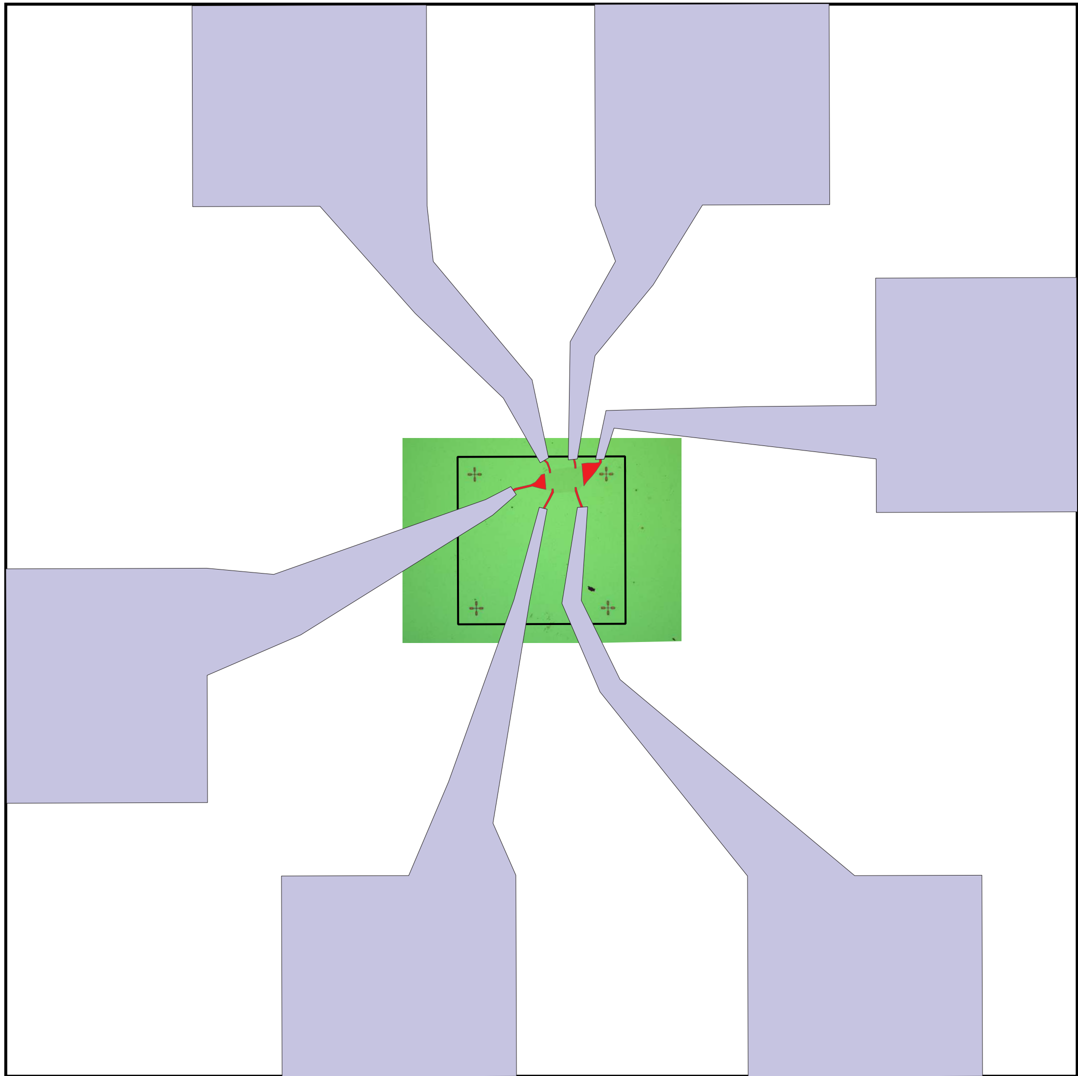

Figure 3.17: Structure design superimposed on the optical image of a graphene flake.

the width of the contacts and distance between them. In some cases, the contacts can be split into a number of polygons with different doses, e.g. higher dose near the edges and corners and lower in the middle.

When the design is ready, the sample is placed in the SEM chamber and the chamber is evacuated. When the pressure reaches 10^{-5} mbar the electron beam scan can enter the chamber. First, the lithography machine needs to be calibrated on a reference sample, then the beam needs to be focused on a wafer edge or a dust particle lying on the wafer surface.

The stage can then be moved to the WF center for the exposure. Using the markers near the wafer edge as a reference, one can travel directly to the desired place on the markers grid. During this stage no accidental exposure is allowed near the flake or the future contacts, so the navigation to the WF center should be done

with the beam blanked. The stage arrives at the middle of the black rectangle (see Fig.3.17).

The stage has a positioning error of 1-2 μm and the crosses pattern can be distorted (they were exposed with 1000 μm WF size). One needs to perform the final correction and match the designed pattern with the real flake position using the four markers. Each cross is scanned locally one by one and their exact real position is read. The software then applies the corrections (stretch and rotate) to the designed drawing accordingly and the exposure can be started. The above alignment procedure is repeated twice for each WF size.

The exposure normally takes several minutes for the small contacts and about one hour for the big ones.

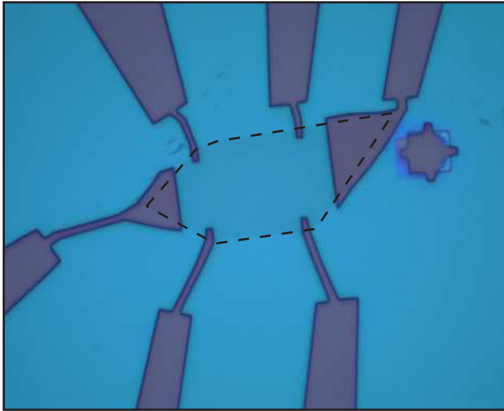

Figure 3.18: Optical image of the developed contact pattern.

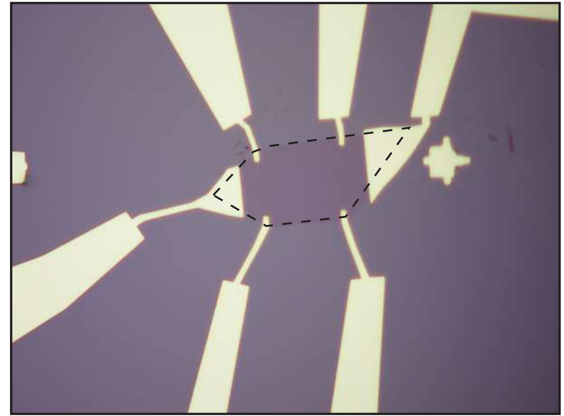

Figure 3.19: Optical image of the finished sample.

Then, the sample is taken back to the clean area for further processing. Development for the contacts is done as follows:

IPA : MIBK : MEK [15 : 5 : 1]	5 *sec in ultrasound*
	+ 5 *sec still*
clean IPA	60 *sec*

and then blow-dried in N_2 flow. The image of the developed sample can be seen in Fig.3.18 – blue regions are still covered with PMMA and the SiO_2 can be seen where the contact pattern is (violet). Cr/Au (5/100) metal film is deposited on top of the whole structure using a thermal evaporator as explained earlier. During lift-off the

rest of the PMMA is dissolved, detaching unwanted metal from the surface. The final device image is shown in Fig.3.19: a six terminal structure made from a graphene flake, with two large 'current' contacts and four smaller 'potential' contacts. The location mark nearby was exposed during the WF alignment process. If there is another EBL stage after that (e.g. mask for etching or doping), these exposed markers can be used again, however, we usually put another set of markers nearby when exposing the contacts (not present on this sample).

Later, the wafer is glued into a package and interconnected using an ultrasound bonding machine as was explained earlier.

3.12 Shaping graphene flakes

A graphene flake can easily be shaped using dry plasma etching, according to a pattern defined by EBL. Apart from the obvious applications, such as creation of nanoribbons, Aharonov-Bohm interferometers, quantum point-contact devices, etc., it is also useful for making 'standard' Hall-bar samples. The current-carrying regions in such Hall-bars are not affected [66] by the presence of the 'invasive' potential contacts, which may cause non-uniform current density distribution (due to the large conductivity of gold) and also change the concentration in a graphene flake near the contacts [67] (due to the difference in the work function for graphene and gold [68]).

As was suggested by the Manchester group, Ar-O_2 plasma can be used for graphene etching using the conventional PMMA resist as a mask [11]. After metal contacts were placed on a graphene flake, the desired shape was defined using a third cycle of EBL. We have found that using an RF plasma barrel reactor (Emitech K1050X, isotropic) gives a vanishing etch rate for graphene compared to the PMMA's etch rate, so that 200 nm resist was removed before a single graphene layer was etched completely.

Successful etching was done later using 'Oxford-Plasma LAB 80' (Bath University) reactive-ion etcher, where RF plasma ions are accelerated in the direction perpendicular to the sample surface. Further experiments showed that the ratio between graphene and PMMA etch rates strongly depends on the gas pressure and perpendicular acceleration of plasma ions (i.e. graphene is etched faster at smaller

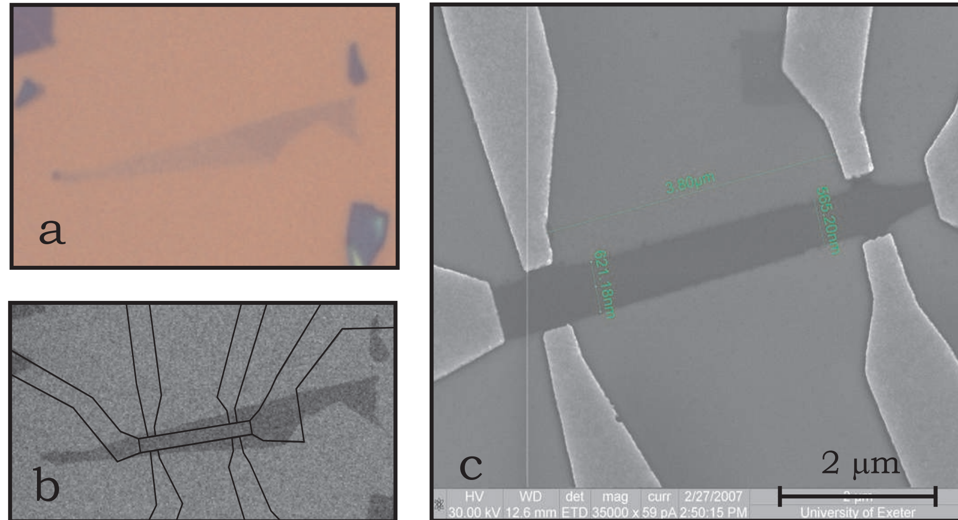

Figure 3.20: Plasma etching of graphene flakes: (a) initial optical image of a flake, (b) Hall-bar design (black lines), (c) final device after the etching and contacts fabrication. Scale bar is 2 μm.

pressure and higher energy). Thus, a good ratio was found at pressure ∼25 mTorr (just enough for ignition) and perpendicular power 25 W with 15 W RF forward power, where a few-layer flake (∼5) was etched completely with a small change in PMMA thickness.

An example of an etched hall-bar is shown in Fig.3.20. A graphene flake (optical image Fig.3.20a) was selected and the contacts were placed according to the pattern shown in Fig.3.20b. Then another EBL created the etching mask with the resulting device shown in Fig.3.20c.

We found that etching creates rough edges (the roughness is ∼20 nm) and charge transport (especially in the narrow structures) becomes affected by these edge defects [23,69]. Therefore, most of the experiments in this project were done using unetched flakes selected so they have a suitable shape.

3.13 Samples storage and handling

There are two significant problems with storing and handling graphene samples. Firstly, ESD (electrostatic discharge) safety is essential. For a 300 nm -thick oxide layer the breakdown voltage can be estimated as 300 V without taking possible defects into account, and can be easily exceeded by carelessly touching the gate contact. However, more care should be taken about the potential between ohmic

graphene contacts. For instance, as explained in [70] a few mA current can heat the graphene film on SiO_2 to a temperature of $\sim 600°C$, which causes its immediate ignition in the air and most likely destroys the flake even in an inert environment. This current can be produced by just a few volts across a usual graphene device.

ESD shocked devices do not seem to have a flake between the contacts and often contacts are partially melted. Such a case is illustrated in Fig.3.21, where the flake and two contacts are gone, leaving droplets of melted metal behind. Samples with a damaged oxide layer usually show a gate leak.

To prevent ESD damage, after bonding samples were always kept in special conductive boxes and stored in metal grounded desiccators to prevent the build up of an electrostatic charge.

Some of the destroyed samples appear to be different from the discussed above. Usually, such devices still have the flake on the surface, but they seem to have one or more contacts torn out along with a piece of the flake (Fig.3.22), most likely due to the thermal expansion of the flake, SiO_2 and metal with different rates and sometimes initial built-in stress in the graphene or metal film. A similar problem was seen by other groups ([71], private communications). This problem cannot be easily avoided, but has happened only to a few samples so far.

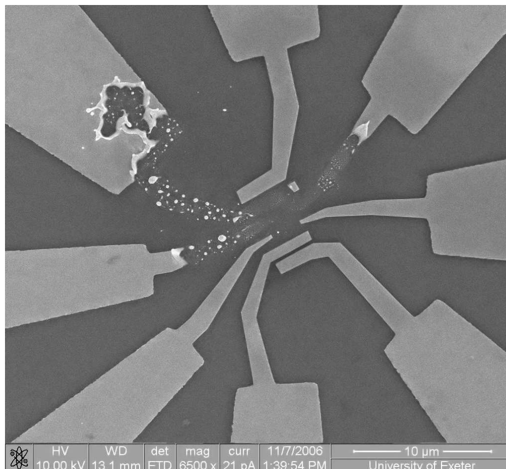

Figure 3.21: SEM image of the sample damaged by ESD.

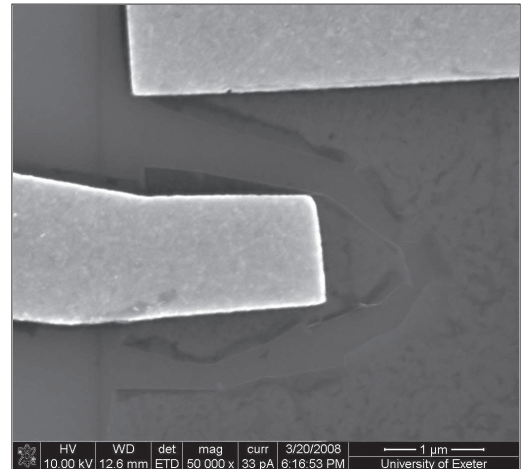

Figure 3.22: SEM image of the sample damaged by thermal shock. A split in the flake can be seen around the contact.

The second important issue concerns the ability of graphene flakes to absorb different compounds present in the environment and thus become contaminated.

The time when a sample is exposed to the air was minimised: the flake was open to air only for ~ 1 min when deposited and then for ~ 10 min when packaged and bonded. After that, samples were placed in a vacuum chamber which was then evacuated. However, we did not pump the volume continuously when storing the samples, because of the back-streaming oil from the rotary pump. Later it was replaced by an oil-free pump.

3.14 Flake suspension and further technology development

One promising and straightforward way to increase the mobility of graphene devices is to suspend them. There are two groups that have reported on transport in suspended flakes so far [23, 72], and many questions are still open in this field. An obvious reason for the small number of publication on suspended graphene is its mechanical instability as it should be spanned over a few micron distance held by the contacts only.

We have created a suspended flake with a 1 μm -long current carrying region. It was deposited and processed as explained earlier and then the wafer was protected with a PMMA film. An additional EBL procedure was used to open a 20×20 μm region in the resist above and around the flake, so that only this region is etched later. The sample was then immersed in buffered 15% HF for 3 minutes (buffering agent is ammonium fluoride (NH_4F)). This concentration of etchant removes 60-70 nm of SiO_2 per minute and does not significantly etch Si or PMMA. After etching the BHF was slowly replaced with vast amounts of water and IPA. Since a monolayer of graphene is very fragile, liquid's surface tension during the conventional drying procedure will easily collapse it. In order to prevent this situation we use the critical point drying procedure (CPD E3000), where a sample is placed in liquid CO_2 and then the volume is driven over the critical point of CO_2 (31° C and 73 Atm). Out of 5 samples only one fraction of one sample has not collapsed, its SEM image is presented in Fig.3.23. The substrate in Fig.3.23 is 45° tilted so that one can see a suspended piece of flake on the left, burst flake in the middle and a sagging flake on the right, where it touches the substrate. It was also suggested [23] that flakes

longer than 10 μm are almost impossible to suspend and so the survival rate strongly depends on the flake size and the contacts overlap area.

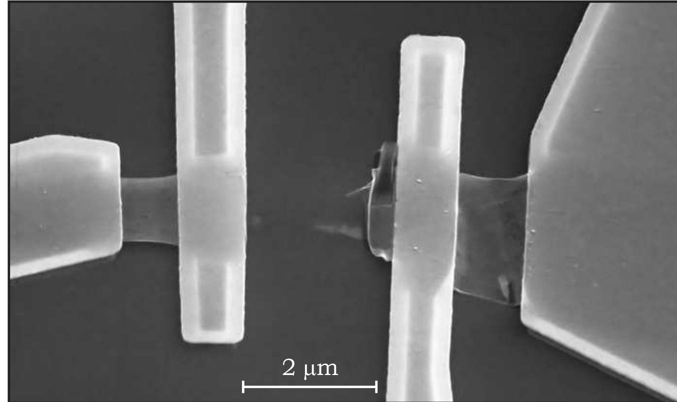

Figure 3.23: SEM image of (left side) suspended and (right side) collapsed parts of a graphene flake, tilt 45°.

The resistance of the suspended fraction of the flake was measured using a two-terminal measurement and is $\sim$ 16 kΩ before and $\sim$ 10 kΩ after annealing at 150° C. It demonstrates a weak dependence ($\sim$ 200 Ω) in the gate-voltage range of $\pm$10 V (higher voltages gives a high probability of the flake collapse due to the electrostatic attraction to the gate). The EN point is outside the studied gate-voltage region and can not be brought close to zero by the conventional annealing, so further experiments will require the current annealing [23].

As this method is a promising way forward, it requires a systematic technological approach and a significant time investment.

3.15 Summary

The chapter describes all stages of the graphene device fabrication, including EBL, development, metalization, lift-off and packaging. There are two sequences in which these stages can be arranged and the one developed during this project has a number of advantages and was discussed in detail.

This chapter can be viewed as a manual for conventional device fabrication and includes a description of safe device storage and handling, also giving examples of the most frequent problems occurring during these procedures. Finally, future suggestions and preliminary experiments done for their realization are given.

Samples fabricated by the author using the techniques explained in this chapter were used in [73–77].

Chapter 4

Transport in graphene flakes

4.1 Introduction

This chapter is dedicated to transport measurements of graphene devices. We investigate the impact of different fabrication conditions on carrier mobility and give statistical data on samples fabricated during this project. We also address the question of the origin of carrier scattering in graphene and compare our results with those obtained by other groups.

4.2 Experimental setup

Most of the experiments were done using the conventional 4-probe lock-in technique in the constant current regime (I=1-10 nA, osc. frequency 17.8 Hz). The measured resistance normally does not exceed 100 kΩ and therefore is not affected by the input impedance of the lock-in amplifiers ($\sim$ 100 MΩ, PerkinElmer instruments). Measurements were done in the temperature range of 300 mK - 350 K and magnetic field 0-12 T in two He^3 cryostats (HeloixTL, HelioxVL made by Oxford Instruments). The magnetic field in the cryostats is created by the passage of a current through superconductive solenoids, provided by a power supply unit PS 120 (also from Oxford Instruments). Gate voltages for the back and top gates were supplied from Keithley 230 and 2400 voltage sources through a RC filter (with a time constant of about one second). Routine testing of the samples and the measurements of the temperature dependencies were performed in a conventional transport dewar in a specially constructed insert (see Appendix). Most of the experimental results presented in

this chapter were obtained by the author, however experiments on QHE and weak localisation have been done with a major contribution of Fedor Tikhonenko.

Initially, all experimental systems had soldered connections between the sample package (shown in Fig.3.11) and the low-temperature wire connections. It was found that conventional soldering ($\sim 200^\circ$ C) damages graphene samples, most likely due to overheating in the presence of air. Therefore, a miniature mechanical clamp was developed with 20 gold spring-pins facing the bottom contact pads of the sample package (shown in Fig.3.12) and a portable heater for in-situ annealing. Such clamps were adapted to all laboratory low temperature systems, including a dilution refrigerator cryostat, Heliox VL, Heliox TL and two dipping inserts. Detailed drawings and material information are given in Appendix 1. Water doping experiments and vacuum annealing were done in a specially developed chamber, also shown in Appendix 1.

4.3 Basic characterisation

Most of the experimental samples studied were mono-layers of graphene. As an example of the characterisation procedure we discuss the same flake used to illustrate the fabrication process in the previous chapter. This sample is labeled G22D8, where G22 stands for 22$^{\text{nd}}$ generation and D8 is the device number. Since this is a multi-terminal device which is relatively big ($\sim$20 μm), the influence of the contacts on the total resistance can be neglected. The sheet resistance of this sample as a function of the carrier concentration is shown in Fig.4.1a. It is found as the measured resistance divided by a geometrical factor of L/W (for a rectangular sample, L, W is length and width, respectively) and the concentration from the capacitance relation (Eq.1.30), taking into account a small offset in the gate voltage. The breakdown voltage for silicon dioxide is $\sim$ 1 V/nm, which theoretically allows one to apply up to 300 V to the back-gate. However, due to accidental mechanical defects and impurities in the oxide layer we limit the range of voltages to $\pm$100 V at low temperatures and $\pm$40 V at 300 K.

In the absence of magnetic field there is no voltage drop across the Hall-contacts and therefore the conductivity can be found as the inverse of the resistivity: $\sigma_{xx} = 1/\rho_{xx}$. This dependence is given in Fig.4.1a as the red curve: one can see that away

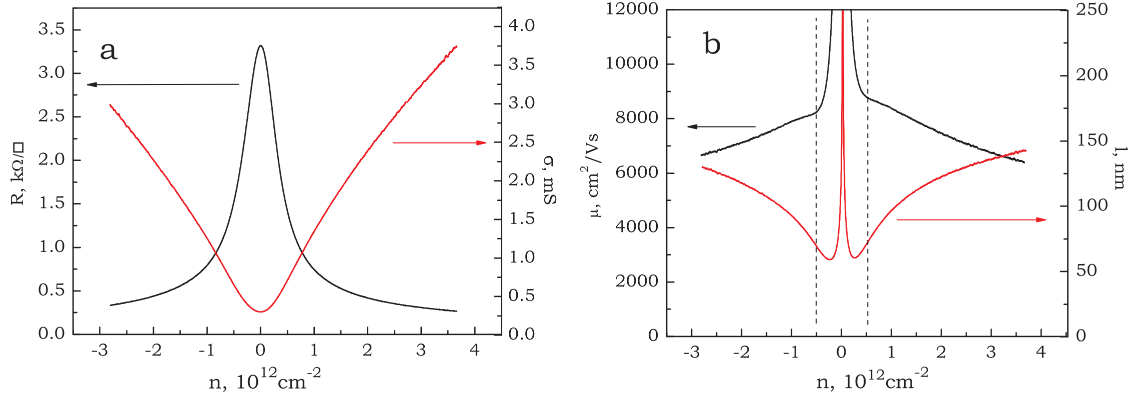

Figure 4.1: Characterization of a graphene sample: a - resistivity (left scale, black) and conductivity (right scale, red) as a function of the carrier concentration, b - carrier mobility (left scale, black) and mean free path (right scale, red) as a function of the carrier concentration.

from the electroneutrality point it is indeed close to linear, which for some time has been accepted to be due to the charged impurities in SiO_2 (see [24] and refs therein). Also this curve is almost perfectly symmetric, which is the case for most of our samples, with a slight hysteresis between two sweeping directions.

The carrier mobility shown in Fig.4.1b was calculated using the Drude formula. At small gate voltages the sample becomes inhomogeneous and breaks into a system of charge puddles. The mobility in this region (labeled as dashed lines) has a divergency due to the finite sample resistance and generally cannot be estimated using the Drude rule. One can see that outside it is slightly decreasing with increasing concentration from $8.5 \cdot 10^3$ to $6.5 \cdot 10^3$ cm^2/Vs.

The mean free path can be found using the Einstein equation

$$\sigma = e^2 D g(E_{\mathrm{F}}), \tag{4.1}$$

where the diffusion coefficient $D = v_{\mathrm{F}} l/2$ and $g(E_{\mathrm{F}})$ is the DOS of carriers in graphene (Eq.1.27). Thus

$$\sigma = \frac{2e^2}{h}(k_{\mathrm{F}} l). \tag{4.2}$$

A simple equation which gives l away from NP is then

$$l\,[\mathrm{m}] = \frac{\sigma}{\sqrt{\pi n}}\frac{h}{2e^2} = 2.72 \cdot 10^{-4}\frac{\sigma\,[\mathrm{S}]}{\sqrt{V_g\,[\mathrm{V}]}}. \tag{4.3}$$

As one can see, the mean free path changes almost by a factor of two (Fig.4.1b),

increasing at high concentrations.

4.4 Annealing and Doping Samples Statistics

After the fabrication process, the electroneutrality point is usually shifted to +10-20 V. In order to remove the fabrication residue discussed in Chapter 2 we anneal the samples at 140-150° C in a He or vacuum environment. We found that 140° C is the optimal temperature and a hotter annealing decreases the sample mobility or makes the sample less homogeneous. During the annealing process we monitor the sample resistance and stop when it saturates (usually 1-4 hours).

As a result of annealing the resistance peak shifts to the left. Typically, we find the peak close to zero (with a small negative offset), independent of the initial air exposure level. The shift of the peak is often accompanied by an increase in mobility by 1-2 times, indicating that fabrication impurities also contribute to scattering. Figure 4.2a illustrates the effect of annealing (optical image of the sample is shown in the inset). The sample consist of two parts - attached single and bilayer graphene flakes, likely deposited from one monocristalline graphite piece. The picture is shown in artificially enhanced colours so that the difference is clearly visible, orange contours show the contact design. The peaks corresponding to the single layer are shown as the black lines, the bilayer with red and the arrows indicate the direction of the shift.

For the single layer the peak moves close to zero but still has a few Volts shift in the negative direction. For the bilayer the shift is similar, but the EN point has a small negative offset compared to the single layer, which was also seen by the Manchester group [78]. One can also compare the peak shapes for the mono- and bilayer flakes, since they were extracted from the same crystal and have been under identical conditions prior to measurement. Away from the electroneutrality point the bilayer always demonstrates a bigger resistance for a given concentration, although naively it should be the opposite, since the bilayer is more robust and less affected by the environment. The observed behaviour can be argued to be a consequence of the peculiar graphene band structure.

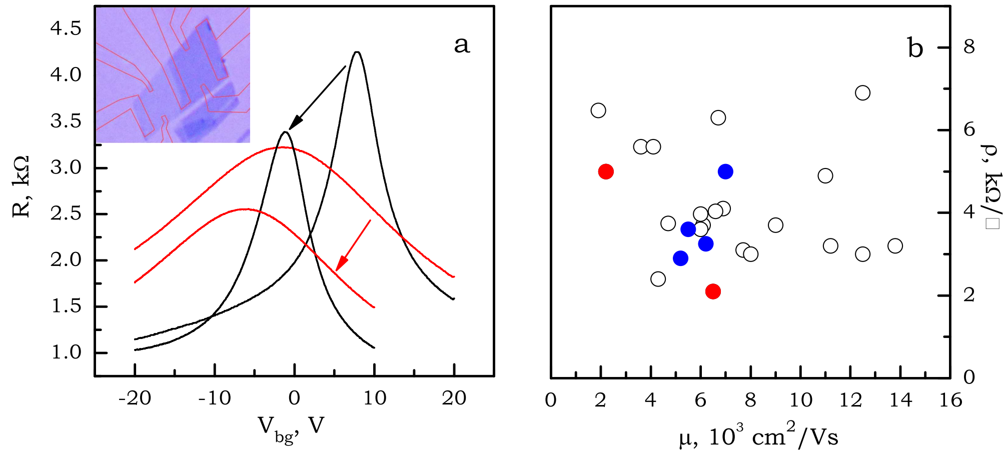

Figure 4.2: (a) Effect of annealing on the $R(V_{\rm bg})$ dependence of single and bilayer graphene samples. Inset shows optical image of the sample. (b) Statistical results on the graphene mobilities plotted against peak values of the sheet resistance. Black circles denote standard fabrication technique, blue dots – flakes deposited in dry argon, red dots – lithography-free technique.

The effect of annealing on the peak height is not always the same. Firstly, we see that samples become more homogeneous, i.e. the 'local' Dirac point position in energy for different regions in the sample approaches the same value, and the peak becomes narrower and higher. Secondly, since the scattering is decreased the resistance also decreases in the whole range of gate voltage and at the EN point as well.

If an annealed sample is exposed again to atmospheric conditions, the peak will move towards positive gate voltages, and for significant exposure times (typically more that 5 hours) will shift even further (to $\sim 30-40$ V) than the initial not-annealed position. We attribute this effect to a different 'atmospheric' doping, since now this process does not induce the contamination layer seen by AFM on a freshly made sample. As a result of the atmospheric exposure we often detect a decrease in the mobility, but this effect in most cases is reversible and the sample can be cleaned by subsequent annealing.

Our experiments show that graphene samples placed in a humid helium atmosphere also exhibit a positive shift of the EN point. The rate of the peak drift depends on the relative humidity and generally agrees with the atmospheric level of doping. A more detailed study of doping effects was made by the Manchester

group [79].

Another type of annealing, done in Ar/H_2 mixture at $\sim 400°$ C, was also investigated during this project. The effect of this annealing was checked on 4 samples. We have found no significant change in the mobility. However, this method is still useful for surface studies (to remove contaminations), and was successfully used by other graphene groups (e.g. [51]).

Fig.4.2b shows statistics on the graphene samples made by the author during the third year of the project. The presented results corresponds to ~25 samples, measured straight after annealing at room temperature in clean He^4. Most of the samples are multi-terminal and were fabricated using different methods of substrate cleaning, different sources of graphite material and other fabrication conditions. The mobility was measured at the concentration $\sim 1.5 \cdot 10^{12}$ cm^{-2} and varies from 2000 to 15000 cm^2/Vs. The highest mobility reached during this project was 20-22$\cdot 10^3$ cm^2/Vs (more detailed data on these samples will be presented later in this chapter). Similar values of the mobility for graphene on SiO_2 were observed by other groups in this field [22, 80, 81].

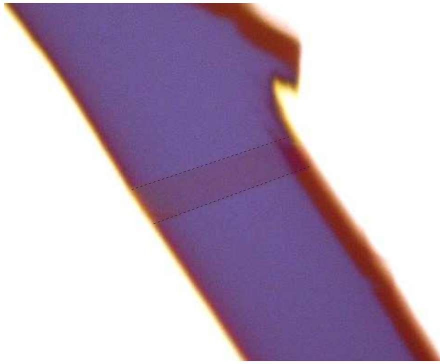

Figure 4.3: Lithography-free graphene device. Flake lenth is ~20 μm.

One can see that there is no correlation between the peak height and the carrier mobility, similar to the published results of the Manchester group [82]. However our average peak values of 4-5 kΩ are systematically lower than the suggested universal value of $h/4e^2$ [82]. We also see no direct impact of different substrate fabrication methods on the device mobility and peak height. Thus, the blue dots in Fig.4.2b show samples deposited in a glove-box in a dry argon environment and the red dots denote the lithography-free device fabrication technique.

In the lithography-free fabrication method, an 18 μm gold wire is manually positioned across a graphene flake and used as an evaporation mask for conventional Cr/Au contacts. After metalization the gold wire is removed. An optical photo of such a sample is given in Fig.4.3. Although we can only fabricate two-terminal samples using this method, and the thick gold wire introduces a shadow due to the

difference in the Au and Cr source positions, we can generally conclude the following:

- Before annealing, lithography-free samples demonstrate a significant shift of the EN point to $V^{\text{off}} \sim 30 - 50$ V, since the atmospheric exposure time during fabrication is about 2-3 hours. This is much longer than that involved in the conventional fabrication approach, where the exposure time usually does not exceed 30 min.
- Annealing at 150° C for 6 hours shifts the EN point towards zero V_{bg}, but there is still a positive value of V^{off} ~10-30 V left after annealing. We attribute this residual doping to the substrate interaction and dopants (e.g. water), captured between SiO_2 and graphene, and absence of the fabrication residue. (As was mentioned earlier, typical graphene samples fabricated with EBL indicate negative residual doping $V^{\text{off}} \sim -10$ after annealing. The value of this shift, however, does not correlate with the sample mobility.)
- A lithography-free sample, placed in a humid He^4 environment exhibits a positive peak drift with a magnitude similar to conventional samples.
- Mobility for the lithography-free samples is similar to the EBL ones. Therefore, the contacts fabrication procedure in the conventional fabrication approach does not introduce significant carrier scattering.

4.5 Review of scattering mechanisms

According to Matthiessen's rule the classical resistivity of the system can be viewed as a sum of different contributions [22]:

$$R_{\text{class}} = R_{\text{ci}} + R_{\text{sr}} + R_{\text{mg}} + R_{\text{ap}} + R_{\text{op}} \tag{4.4}$$

The first term R_{ci} is due to the scattering by charged impurities discussed in the first chapter. This term is inversely proportional to the carrier concentration [15] and has a weak temperature dependence [83]:

$$R_{\text{ci}} = \frac{h}{e^2}\frac{1.3}{\kappa^2}\frac{n_i}{n}\left[1 + f(T, E_{\text{F}})\right], \tag{4.5}$$

where κ is the dielectric constant of the environment, n_i is proportional to the density of charged impurities. The second term in the brackets comes from the Fermi-Dirac distribution function, and takes into account the fact that the Fermi energy can be comparable to the temperature.

The second contribution in Eq.4.4 is due to short-range scattering on atomic-scale defects and surface corrugations [22]. This term is energy and temperature independent [18]. The first two terms have been used to explain the experimental low-temperature dependence $\sigma(n)$ [22].

The third term was proposed by F. Guinea [19] and arises due to the fact, that vacancies, cracks, deep substrate impurities and corrugations [21] give rise to bound states at the Dirac point, also called midgap states. The associated resistivity term is

$$R_{\mathrm{mg}} = \frac{h}{2e^2}\frac{n_{\mathrm{mg}}}{n}\ \ln^{-2}(\sqrt{n\pi}R_0), \tag{4.6}$$

where n_{mg} is proportional to the concentration of midgap states and R_0 is a vacancy radius. This mechanism was used as an alternative explanation [19] of the observed $\sigma(n)$ and the value of the resistivity peak.

The next term is coming from the acoustic phonons in graphene. It is independent of carrier density and can be written as a linear function of the temperature [84]:

$$R_{\mathrm{ap}} = \frac{h}{e^2}\frac{E_D^2 k_{\mathrm{B}}T}{2\hbar^2 v_{\mathrm{F}}^2\rho}\left(\frac{1}{v_l^2}+\frac{1}{v_t^2}\right), \tag{4.7}$$

where $E_D = 9$ eV is the deformation potential constant, $v_l = 2.1\cdot 10^6$ cm/s and $v_t = 7\cdot 10^5$ cm/s are the longitudinal and transverse sound velocities and $\rho = 6.5\cdot 10^{-8}$ g/cm^2 is the areal density of the graphene sheet.

The last term represents electron scattering on the surface optical phonons from the substrate and becomes significant at high temperature (above 200 K) [22]:

$$R_{\mathrm{op}}\,[\Omega] = 0.607\cdot\frac{h}{e^2}V_{\mathrm{bg}}^{-1.04}\left(\frac{1}{e^{0.059/k_{\mathrm{B}}T}-1}+\frac{6.5}{e^{0.155/k_{\mathrm{B}}T}-1}\right). \tag{4.8}$$

It was clearly demonstrated [23] that substrate induced contributions $R_{\mathrm{op}}, R_{\mathrm{ci}}$ vanish for suspended graphene flakes and the temperature dependence $R(T)$ is linear according to the acoustic phonon scattering, Eq.4.7.

The total conductivity is then given by the sum of the classical conductivity given above and quantum corrections due to interference effects:

$$\sigma_{\text{tot}} = R_{\text{class}}^{-1} + \delta\sigma^{\text{wl}} + \delta\sigma^{\text{ee}}, \tag{4.9}$$

where σ^{wl} represents weak (anti)localisation effect and σ_{ee} is due to the electron-electron interaction. The temperature dependence of these contributions was not studied experimentally but were predicted as follows. The electron-electron interaction for high temperatures ($kT\tau'/\hbar \ll 1$) was studied theoretically for graphene in [85] and given by:

$$R(T) - R(0) = -\frac{h}{e^2}\frac{T\hbar}{E_f^2\tau'}, \tag{4.10}$$

where τ' is the characteristic scattering time for atomically sharp defects.

The weak (anti)localisation effect gives a logarithmic correction to the conductivity (below 100 K) [16]:

$$\delta\sigma^{\text{wl}}(T) = -\frac{e^2}{\pi h}\left[\ln\left(1 + 2\frac{\tau_\varphi}{\tau_i}\right) - 2\ln\frac{\tau_\varphi/\tau_p}{1 + \tau_\varphi/\tau_\star}\right], \tag{4.11}$$

where τ_φ is the decoherence time, $\tau_\star^{-1} = \tau_i^{-1} + \tau_z^{-1} + \tau_w^{-1}$. The authors discussed different sorts of scattering events, namely when scattering occurs within one valley (or intra-valley, τ_z^{-1}) or between different valleys (inter-valley, τ_i^{-1}). While the first (τ_z) is originating mainly from charged impurity scattering, the second (τ_i) requires a significant change in the quasiparticle momentum and is associated with sharp impurities and lattice defects. They also discussed the effect of deformation of the Dirac cones (described by the time τ_w), which breaks the $\vec{p} \to -\vec{p}$ symmetry and also disturbs the valley symmetry. Considering different relations between these scattering times, one can realize weak localisation (negative correction, $\tau_\varphi > \tau_i,\ \tau_\star$) or weak anti-localisation (positive correction, $\tau_\varphi < \tau_i,\ \tau_\star$) which was demonstrated experimentally [77].

4.6 Temperature dependencies of the conductivity: experimental results

The experimental results obtained for a sample with an average mobility above 10^4 cm^2/Vs are shown in Fig.4.4. Conductivity as a function of the back-gate voltage is given for different temperatures (4.2 to 300 K, see the figure legend for the colour code) and zero magnetic field. The sub-linear shape of the conductance gets more pronounced at higher temperatures, which is typical for our different samples, and consistent with the results of other groups (e.g. [80]).

Since all the contributions summarized above have either no ($R_{\rm sr}$, and $R_{\rm ap}$) or inversely proportional ($R_{\rm op}$, $R_{\rm ci}$, $R_{\rm ee}$) dependence on the carrier density, we have separated these two groups in a similar manner to Morozov et al. [80].

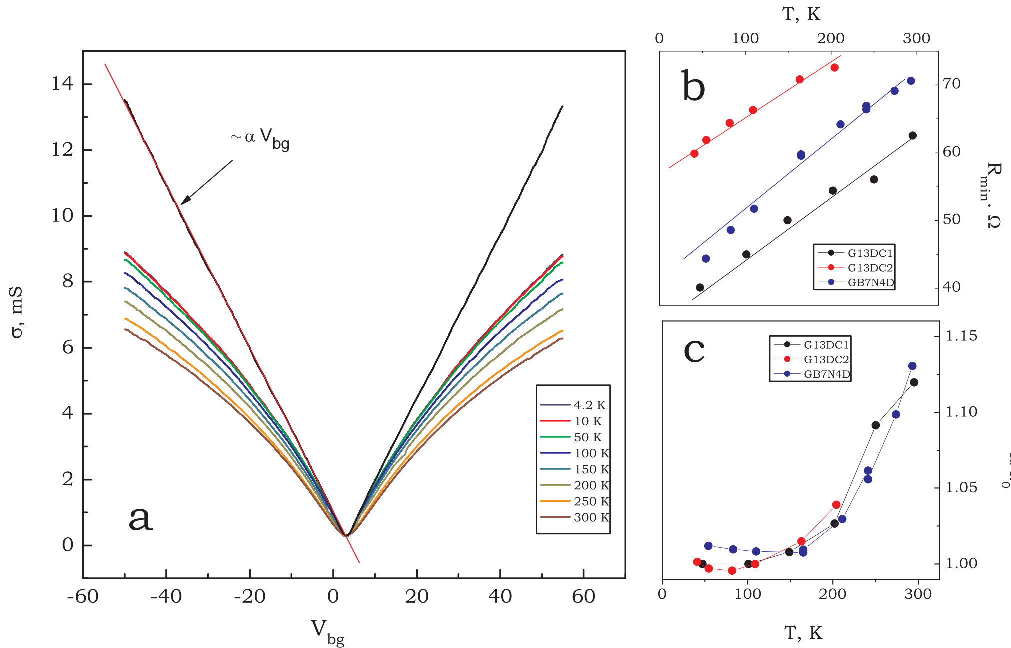

Figure 4.4: (a) Conductance as a function of back-gate voltage for different temperatures, top black curve shows result of the linearization procedure. (b) Extracted values of $R_{\rm min}$ as a function of temperature. (c) Slope α as a function of temperature. Colours denote different samples.

For each temperature we extract from the experimental $R(V_{\rm bg})$ a constant resistance $R_{\rm min}$ so that the conductance becomes linear as a function of density, as shown in Fig.4.4 as the top black curve. The role of $R_{\rm min}$ is played by the two density-independent contributions: $R_{\rm sr}$, and $R_{\rm ap}$. The resulting conductivity becomes perfectly linear as has also been observed in [80].

The density independent contribution $R_{\rm min}$ extracted for each curve in Fig.4.4a is presented in Fig.4.4b, and can be fitted (solid lines) with Eq.4.7 using values of the deformation potential 18 ± 2 eV. This value agrees with the experimental observations in [22], and is close to those for suspended flakes [23]. An offset to the linear behaviour is most likely due to the short range scatterers and is a sample-dependent constant.

We have found that the slope of the linearised $\sigma(V_{\rm bg})$ is also temperature dependent, especially above 200 K. The value of the normalized slope α/α_0 is plotted against temperature in Fig.4.4c. The observed behaviour was earlier attributed to the exponential contribution of the optical phonons [22] and also includes $R_{\rm ci}(T)$. The third contribution in this picture, $\sigma_{\rm ee}$, should give a linear T correction with a negative slope, and is small according to our estimations taking $\tau' = \tau_i$. However, the observed dependence can be determined by the interplay of these three contributions, which can not be simply separated.

At low temperatures the weak (anti)localisation has to be taken into account. The exact calculation of this correction according to Eq.4.11 requires information about the scattering times $\tau_i, \tau_\star$ and the decoherence time $\tau_\phi(T)$. Their values can be found from the measurement of the suppression of the WL effect in a magnetic field as for the sample G13DC2 (corresponding WL measurements can be found in [77]).

Although this section gives a qualitative picture of the scattering phenomena in graphene, it assumes a complicated interplay between different scattering mechanisms and generally disagrees with [24]. At this stage the exact picture of scattering in graphene is unclear and this question needs further experimental and theoretical attention, which lies beyond the scope of this work.

4.7 Transport in high magnetic field

4.7.1 Specifics of high B behaviour in graphene

This section describes the high magnetic field behaviour and starts with a brief introduction to the Shubnikov-de Haas oscillations. In the presence of a magnetic field directed perpendicular to the graphene layer electrons experience a Lorentz

force which causes them to move along circular trajectories between the scattering events. For a sufficiently high magnetic field $\omega_c \tau > 1$ electrons can complete full orbits without being scattered, with quantized values of the orbit diameter. The energy spectrum turns into a system of degenerate Landau levels with the delta-function-like DOS at each level, broadened in the presence of disorder.

For a conventional 2DEG with a parabolic dispersion relation the Landau levels are equidistant in energy: $E_n = (n + 1/2)e\hbar B/m^\star$, $n = 0, 1, 2 \ldots$. For massless fermions completing cyclotron orbits in graphene, Berry's phase contributes to the semi-classical quantization and therefore introduces a half-period shift into the Landau-level pattern, first observed in [86]: $E_n = \sqrt{2e\hbar v_{\mathrm{F}}^2 B(n + 1/2 \pm 1/2)}$, where '$\pm 1/2$' refers to the pseudospin projections. Since $E_n \propto \sqrt{n}$, now the quantisation is equidistant in the concentration and can be directly observed in the measurements of the longitudinal σ_{xx} or transverse σ_{xy} conductivity as a function of either magnetic field or the energy [81, 86].

The longitudinal magnetoresistance for the magnetic fields above 1 T exhibits Shubnikov-de Haas oscillations. At high magnetic field $B \sim 10$ T, R_{xy} demonstrates plateaus and R_{xx} vanishes, which is the hallmark of the Quantum Hall Effect regime. It was earlier demonstrated that the Shubnikov-de Haas oscillations in graphene are similar to the ones for conventional 2DEG systems [87], but with the effective mass $m^\star$ replaced by the cyclotron mass in graphene $m_c = E_F/v_f^2$, which vanishes at low carrier concentration [81, 86]. Also, in contrast with conventional metals, $R_{xx}(B)$ exhibits maxima rather than minima at integer values of the Landau filling factor ν due to the Berry's phase, and therefore [87]

$$\frac{\Delta\rho_{xx}}{\rho_0} \propto \exp\left(-\frac{\pi\,|E_{\mathrm{F}}|}{eBv_{\mathrm{F}}^2\tau_q}\right)\frac{\xi}{\sinh(\xi)}\cos\left(\frac{\pi E_{\mathrm{F}}^2}{\hbar eBv_{\mathrm{F}}^2}\right), \qquad \xi = \frac{2\pi^2 k_{\mathrm{B}}T\,|E_{\mathrm{F}}|}{\hbar eBv_{\mathrm{F}}^2}, \tag{4.12}$$

where τ_q is the quantum lifetime, which reflects a change in the quasiparticle momentum $\vec{k}_{\mathrm{F}}$. These results were also obtained for graphene directly [88].

4.7.2 Experimental observation of resistance in high B

Figure 4.5 shows typical measurements of R_{xx} (a) and R_{xy} (b) for the sample G13DC2 in B-fields up to 6 T. The inset in Fig.4.5b shows $R(V_{\mathrm{bg}})$ for this sam-

ple with three electron concentrations and provides a colour-code for magnetic field dependencies (blue, red, black correspond to $n = 2.02, 2.80, 3.55 \cdot 10^{12}$ cm^{-2}, respectively). The peaks in R_{xx} are equidistant in the inverse B-field, and their period allows one to find the carrier concentration n_{ShdH}. Another way to determine the carrier concentration is to measure the Hall resistance R_{xy} as shown in Fig.4.5b, where the slope is proportional to $1/en_{\text{Hall}}$ for one type of carriers. All three concentrations $n, n_{\text{Hall}}, n_{\text{ShdH}}$ are identical within 5% accuracy (this was also reported in [86]) which suggests that all the carriers are mobile and participate in the charge transport. A larger discrepancy is often observed for n_{Hall} since most of our samples are narrow and the concentration near the metal contacts is affected by their presence [66].

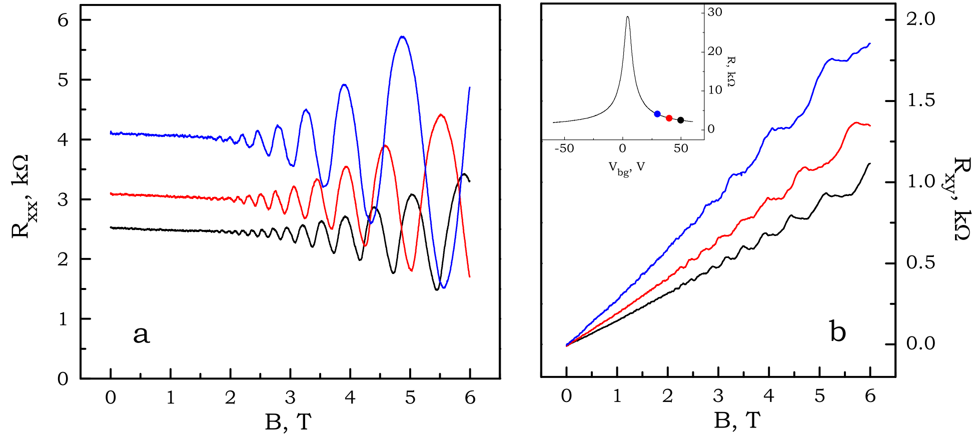

Figure 4.5: Shubnikov-de Haas oscillations (a) and Hall effect (b) as a function of magnetic field for three different concentrations indicated as coloured dots on $R(V_{\text{bg}})$ in the inset of (b). Temperature is 4 K, carrier mobility for the studied range on V_{bg} is $\mu = 12000$ cm^2/Vs.

Analysis of the exponential envelope of the Shubnikov-de Haas oscillations allows one to find the quantum lifetime τ_q. In order to extract τ_q we first remove a small monotonic component so that the oscillations are symmetric, divide it by $\xi/\sinh(\xi)$ and then measure the peak amplitude. According to Eq. 4.12, the logarithm of the peak amplitude plotted against the inversed magnetic field $1/B$ is a linear function with a gradient of $\pi |E_{\text{F}}| / v_{\text{F}}^2 e\tau_q$. Thus, the values of τ_q obtained for the same sample at different temperatures are shown as symbols in Fig.4.6. We observe no obvious temperature dependence in the range from 250 mK to 16 K.

The concentration dependence of τ_q and τ_p provide important information about the nature of the disorder in graphene. The ratio τ_q/τ_p reflects whether the scattering comes from long-range ($\tau_p/\tau_q \gg 1$) or short range ($\tau_p/\tau_q \sim 1$) disorder.

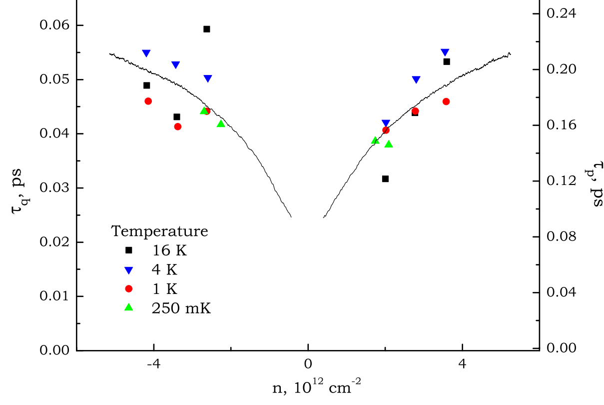

Figure 4.6: Left axis: quantum lifetime as a function of the carrier concentration for different temperatures (corresponded data shown as symbols, see colour-code). Right axis: momentum relaxation time (refers to solid line) calculated from $R(V_{\rm bg})$.

This ratio was studied for two samples with average mobilities around 10^4 and $2 \cdot 10^4$ cm^2/Vs. Fig.4.6 shows both τ_q (left scale) and τ_p (right scale) for the sample with the lower mobility having similar dependence on the carrier concentration. The ratio τ_p/τ_q is $\simeq 4$ for this sample and close to 6 for the sample with higher mobility, which indicates dominant long range scattering.

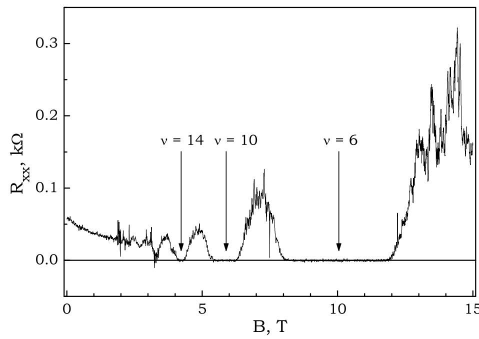

Figure 4.7: R_{xx} as a function of B for $n = 1.5 \cdot 10^{12}$ cm^{-2}, $T = 50$ mK. The filling factor values are found from the position in B of centers of minima in R_{xx}.

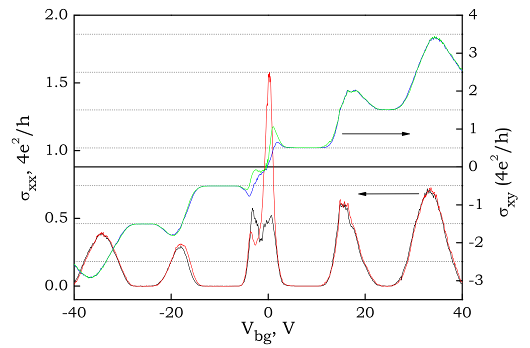

Figure 4.8: The longitudinal (black and red, left axis) and transverse (green and blue, right axis) conductivity as a function of gate voltage, with $T = 5.6$ K $B = 12.5$ T.

Fig.4.7 shows longitudinal resistance at high magnetic fields (up to 15 T) for

the sample with the carrier mobility of $2 \cdot 10^4$ cm^2/Vs. In magnetic fields above 5 T R_{xx} vanishes indicating appearance of QHE regime. Fig.4.8 shows gate voltage dependence of longitudinal and transverse conductivities at magnetic field of 12.5 T. One can see that the presence of a Landau level at zero energy is clear from the peak in σ_{xx} at zero gate voltage which is a unique feature of graphene and can be used as yet another way to confirm whether the flake is single layer thick or not. The conductivities are plotted in units of $4e^2/h$ in order to emphasise the fact that the quantised plateaux in σ_{xy} indeed correspond to half-integer filling factors. Also, as was mentioned earlier, the Landau levels in graphene appear to be equidistant in gate voltage rather than energy.

4.8 Weak Localisation

Similar to the case of conventional 2DEGs, quantum interference of diffusive carrier trajectories which contain loops give rise to a correction to the Drude conductivity. This is valid only if the carrier wave-function does not spontaneously change its phase on such trajectories, in other words the phase braking length L_φ exceeds the mean free path l. Thus, in the absence of a magnetic field a carrier gains the same phase change while traveling clockwise and anti-clockwise along a looped path. This results in constructive interference of these two wave directions and therefore the carrier is effectively being delayed on such looped trajectories so that the total resistance rises. In graphene, such interference is destructive due to the Berry phase and so the correction should have the opposite sign and is called anti-localisation correction.

However, due to 'warping' (distortion) of the conical dispersion relation [16] and also corrugations of the graphene sheet [89] weak anti-localisation is suppressed. In addition, due to the presence of short-range disorder, elastic scattering can occur not only inside one valley, but between two valleys which results in breaking of the chirality and restores the weak localisation effect [16].

A magnetic field suppresses this effect and the theory of quantum interference [16] predicts the following magnetoresistance in graphene:

$$\Delta\sigma(B) = \frac{e^2}{\pi h}\left[F\left(\frac{\tau_B^{-1}}{\tau_\varphi^{-1}}\right) - F\left(\frac{\tau_B^{-1}}{\tau_\varphi^{-1} + 2\tau_i^{-1}}\right) - 2F\left(\frac{\tau_B^{-1}}{\tau_\varphi^{-1} + \tau_\star^{-1}}\right)\right]. \qquad (4.13)$$

Here $F(x) = \ln(x) + \psi(0.5 + x^{-1})$, $\psi(y)$ is the digamma function, $\tau_B^{-1} = 4eDB/\hbar$, D is the diffusion coefficient and the scattering times τ_i, $\tau_\star$ were introduced in section 4.5.

Depending on the ratio between these scattering times and the decoherence time, the weak localisation correction (Eq.4.13) can have either a positive or negative sign. This effect was studied in detail on the samples produced by the author and published in Refs. [73–75, 77]. Since major contributions in the experimental measurements and data analysis was done by other members of quantum interaction group at Exeter, the author refers the reader to these articles.

4.9 Conclusion

This chapter describes the general characterisation studies of graphene, such as the dependence of resistance on concentration, temperature and magnetic field. It is shown that variations in the fabrication process, such as using different substrate cleaning methods, environmental graphene deposition and lithography-free fabrication technique makes either no difference or a small change in carrier mobility. We also address the question of carrier scattering in graphene and discuss the possibility of remote charged impurities being the dominant source of scattering. Studies of the quantum lifetime extracted from the Shubnikov-de Haas oscillations also confirms that scattering in graphene has a long-range character rather than shot-range character.

Chapter 5

Suspended bridge fabrication

5.1 Introduction

Graphene-based devices with a controllable spacial modulation of carrier concentration are an attractive object for transport studies. Such modulation can be achieved using local metal gates, separated from the current carrying region by a layer of insulating material. A top gate placed above a graphene sheet attracts charged carriers in graphene, therefore creating a local region of a different concentration. Tuning the electric potential on the top and back gates, it is possible to increase or deplete the local concentration, or even reverse the sign of charge carriers under the top gate relative to the rest of the graphene sheet. In the latter case, different physical phenomena can arise in charge transport, depending on the ratio between the mean free path l, size of the inversed concentration region l_{pnp} and the size of individual p-n and n-p junctions $l_{\mathrm{pn}}, l_{\mathrm{np}}$ (see chapter 6). Making devices in which the size of the locally-gated region is comparable with the mean free path of carriers is an intriguing technological task since l is ~ 100 nm for 'standard' graphene devices. This chapter is focused on the fabrication of top-gated structures and will start with a short review of the current activity in this field.

The first attempt to create a top-gated graphene device was published in April 2007 [90] and a significant drop in the carrier mobility was reported. This drop in mobility was induced by the evaporation of SiO_2 onto the graphene surface aimed to create a dielectric layer. Following this, experiments by Stanford [91], Harvard [92] and Columbia [93] groups were dedicated to the study of top-gated samples

with different dielectric layers separating the gates and graphene sheet: crosslinked PMMA, HSQ/HfO_2 bilayer and three-layered NO_2/TMA/Al_2O_3, respectively. In order to achieve $l \geq 100$ nm under the gate, which requires high μ, we choose to develop a dielectric-free approach using suspended metal gates [94].

An approach selected in this work uses the idea of having no material between the top gate and graphene, i.e. using suspended metal gates. Keeping the top surface of graphene clean, this approach gives an ultimate mobility dictated by the scattering mechanisms discussed earlier (chapter 4), without introducing any extra deposits on top. This is important since, for instance, the crosslinked PMMA used in [91] limits the mobility to $2 \cdot 10^3$ cm^{2}V^{-1}s^{-1}, which is at least 5 times less than the mobility of typical graphene Hall-bar samples without a dielectric layer.

The technique of air bridges has been in use for experimental sample fabrication for more than 10 years [95]. Since PMMA resist is used for the contact fabrication in our samples, the optimal choice for the gate suspension would be the same resist (in order to avoid any extra compounds in the processing). Currently, two different approaches have been used with PMMA, both utilising the idea of creating a specific resist profile with further metalization and lift-off. The first utilises a low acceleration voltage EBL and relies on different depth of electron penetration [96, 97] in resist. The second, and more convenient, is based on a multilayer resist approach, where a spatial variation of the EBL dose allows one to selectively remove resists with different sensitivities [98]. Although this method is well established nowadays, the specific task we had was to create narrow ($\sim$ 100 nm) and long (several micrometers) bridges, which most of previous papers had not addressed.

5.2 General technique

The approach based on a multilayer resist system was selected for the creation of suspended nanobridges over a graphene flake. This method involves the selective development of different layers of resist, such as two different MW of PMMA or a combination of PMMA and its copolymers.

The simplest way, which we chose, uses two different MW of PMMA (Fig.5.1a): a bottom layer of less-sensitive (or 'hard') resist and a top layer of more-sensitive (or 'soft') resist. Careful selection of the exposure doses allows removal of both the

layers for the creation of pillars and only the top layer for the span of the bridge.

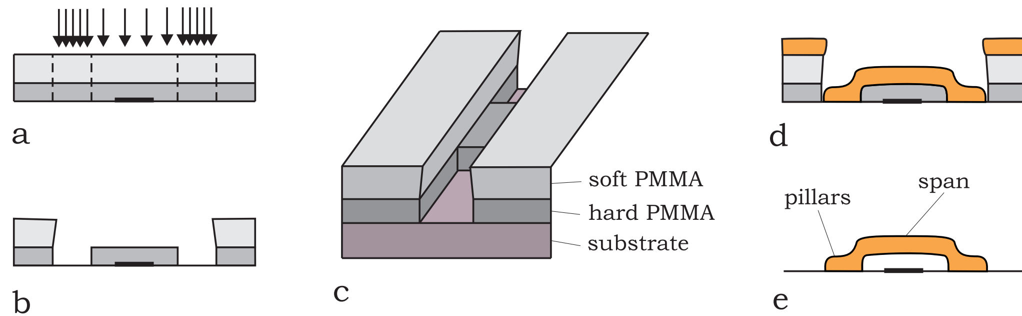

Figure 5.1: Stages of suspended gate fabrication: a – electron beam exposure, b,c – resist development, d – metalization and e – lift-off.

The resulting developed resist profile is shown in Fig.5.1b (2D) and Fig.5.1c (3D). After the evaporation of Cr/Au bilayer (typically 5/250 nm), the whole surface is covered with a metal film (Fig.5.1d). If the thickness of the bottom resist layer is smaller than metal thickness, the span and pillars will be linked together. However, the thickness of the top resist layer has to be at least twice bigger than the metal thickness so as to sufficiently separate the bridge parts and the rest of the metal film. This is important on the last stage of the fabrication - lift-off, because the bridge can be pulled away with the metal film if they are strongly attached to each other.

Metal bridges with a span length of up to 3 micrometers and 100 nm wide were created. These bridges are mechanically stable and can sustain liquid (IPA) surface tension when being dried and even a short (several seconds) ultrasound treatment. The load on the bridge with a voltage applied (100 V) can reach 1 μN (from estimation for the electrostatic force), and, the longest of them (3 μm) can actually collapse at voltages $\sim$50 V. Thus, the flakes used for top-gate experiments must be less than 2 μm wide, so that they fit under the span and are not affected by the side pillars.

5.3 EBL and resist

5.3.1 Focusing and exposure

Normally, EBL involves exposure of three rectangular areas – two pillars and a span – with a constant dose within each rectangle. The narrowest bridges are 100 nm

wide and are comparable with the electron spot size ∼15 nm, so focusing of the beam becomes an important issue. Because the PMMA surface is perfectly flat and the location markers seen through PMMA are smeared, there are no features with a good contrast near the graphene sample that can be used to adjust the focus on. The sample holder in the EBL machine is not perfectly flat, so focus and astigmatism changes as a function of x,y-coordinates, even on a polished silica wafer. Thus we employed the so-called contamination lithography [54] to create a spot near the sample location and focus the electron beam using this spot, repeating this procedure until the spot size reaches 15-20 nm.

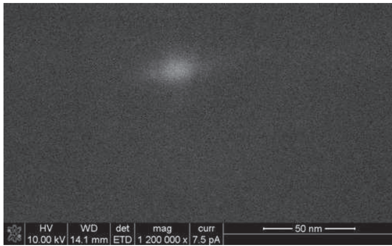

Figure 5.2: Contamination spot grown using 20 second point-like exposure.

Electron beam exposure at one point on a substrate can cause an accumulation of hydrocarbons and other contaminants from the chamber atmosphere at this local point [54]. This process requires a high dose ∼1 C/cm^2 and depends on the chamber pressure, so often it was necessary to introduce a low pressure of a hydrocarbon gas ($C_{10}H_8$, $\sim 5 \cdot 10^{-5}$ mbar) in order to make the growth possible. Such a spot can be seen in SEM as shown in Fig.5.2, smeared with the same beam size as drawn.

After the focusing procedure, the exposure of the bridges takes a few seconds. Ohmic contacts can be exposed straight after, using the same dose as for pillars but corrected for the proximity effect. Thus, the whole structure is made in one EBL load similar to the conventional samples discussed in chapter 3.

5.3.2 Resist intermixing

When two resist layers are spun on top of each other, every new layer spilled on the surface of a pre-baked bottom layer partially dissolves it. This problem of interlayer mixing is a general problem arising when using multilayer resist. For instance, a 75 nm thick layer can be washed away completely during the spin of subsequent layer cast in anisole. As a result, there is no clear boundary between the two layers, such that the bottom surface of the resulting bridge span becomes rough.

The table in Fig. 5.3 shows the dissolution rates of PMMA films in different

Solvent	Soak time (min)	Rate ± 15% (nm/min)
Chlorobenzene	0.5	140
MIBK	1.0	25
Xylenes	5.0	10
Orthoxylene	15.0	5
MIBK:IPA (1:3)	15.0	No det. change

Figure 5.3: PMMA dissolution rates, taken from [99].

solvents under the normal conditions [99]. According to this table, methyl isobutyl ketone (MIBK) was selected as a solvent for PMMA and P(MMA-MAA). For resist preparation, powder of polymer (purchased from Sigma-Aldrich Corp.) was mixed with MIBK according to a required mass ratio and stirred for 5 hours at T$\sim$ 60° C and then filtered through a 100 nm grid filter to avoid particle contamination. The resulting resist was used as well as the standard mixture for the creation of contacts and suspended gates. According to [99] the amount which can be dissolved using MIBK as a solvent does not exceed 5 nm for a quick spinning procedure. This number is a good estimate for the span's bottom surface roughness.

5.4 Undercut profile and dose selection

It was found that, using two layers of resist (Fig.5.4a) it is only possible to create bridges with a 10 kV energy beam. Higher energies are less affected by the forward scattering and create almost vertical walls in the resist, and therefore a small source misalignment during metal evaporation, or an edge defect, lead to the creation of weak joints between the bridge and metal film. For contacts this is not important and one can forcedly remove the top film, but the span of the bridge is too weak for that.

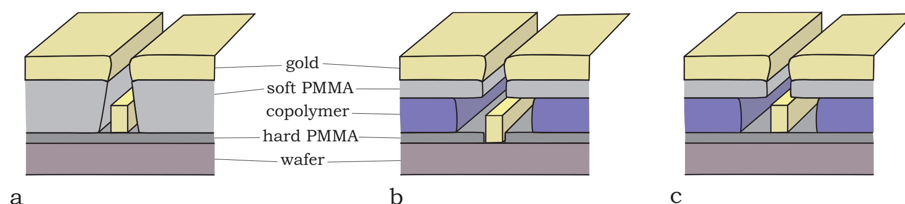

Figure 5.4: Undercut profile for different resist configurations. Bilayer (a) (span) and triple layer (b) (pillar), (c) (span) resist techniques.

To overcome this problem a second configuration depicted for the pillars (Fig.5.4b) and span (Fig.5.4c) was used. It is a three-layered resist configuration with a thick P(MMA-MAA) booster. The bottom hard resist plays the same role - its thickness defines the bridge clearance. The next copolymer layer provides a good undercut profile for the future lift-off. Since it requires a few times smaller exposure dose, it will be overexposed. Finally, the top layer (soft PMMA) is the imaging layer, i.e. it works as an evaporation mask. The bottom layer was cast in anisole and the top two in MIBK as explained above.

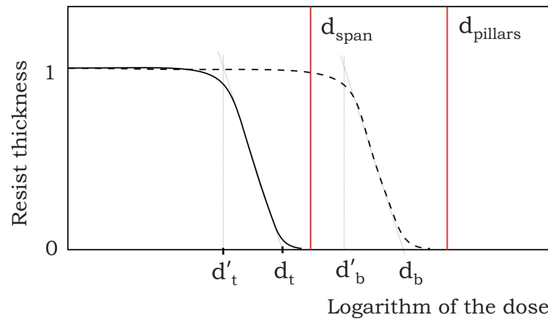

Figure 5.5: Developed resist thickness against the exposure dose for the two different resist layers. Red lines d_{span} and $d_{pillars}$ illustrate a correct exposure doses for the different regions of suspended bridge.

For the top and bottom layers PMMA molecular weights of 120K and 950K were used. Despite an order of magnitude difference in the chain length, the sensitivity of these layers, d_t and d_b, differs only by a few percent. Selection of the correct span dose can be illustrated schematically in Fig.5.5. It is higher than d_t (so it dissolves the top layer) and below the threshold dose d'_b for the bottom layer (so it stays untouched). The pillars dose selection is less strict and should be selected higher that d_b.

In order to find the correct dose for the exposure the following test was done. Together with a set of experimental samples a few bare substrates were coated with resist. These wafers reproduce the same resist conditions and could be used for the dose test. A set of suspended bridges is then exposed on the test wafers with different lateral sizes and span doses, which are then developed and evaporated. The correct doses found from this test were then applied to the actual graphene samples.

The distance between the bottom of the span and the wafer surface was measured using SEM (Fig.5.6) and is shown in Fig.5.7 as a function of the span dose. Indeed, the clearance of the span is almost equal to the thickness of the bottom resist layer. Let us consider in detail 75 nm wide span exposure shown as the red curve in Fig.5.7. The optimal shape of the bridge is seen in the SEM image in Fig.5.6b, which develops for a small range of exposure doses (170-200 μAs/cm^2) and is stable within

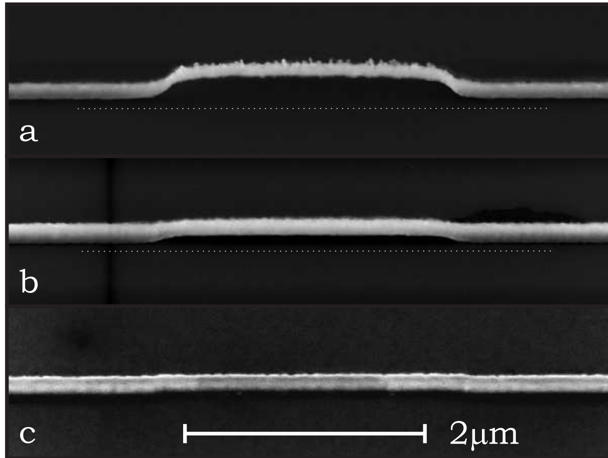

Figure 5.6: SEM image of three different bridges made with 45° tilt to the surface. Image (b) shows the optimal span dose, whilst (c) and (a) are overexposed and underexposed cases, respectively.

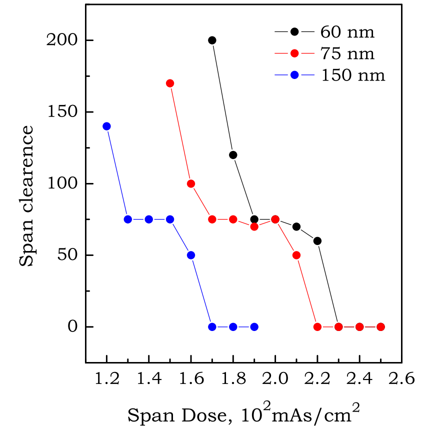

Figure 5.7: Bridge clearance as a function of the span dose. Three curves show 60, 75 and 150 nm wide patterns resulting in 90, 105 and 150 nm real span width, respectively.

this range. An increase of the dose further leads to a quick collapse of the clearance distance, resulting in the shape shown in Fig.5.6c, where the whole structure is lying on the surface. Another unstable configuration is seen in Fig.5.6a, and occurs when the top layer is not sufficiently exposed and does not dissolve completely during development. Consequently, the clearance for this bridge is bigger and its shape becomes unstable. The pillars were exposed with 300 μAs/cm^2.

All these cases can be seen in Fig.5.7 where the plateau denotes case (b), underexposed and overexposed cases (a) and (c) correspond to the quick clearance change away from the plateau. Changing the line size will also change the described picture due to the presence of the proximity effect. Thus, the exposure time should be smaller for wider patterns (150 nm, blue curve) and bigger for the narrower patterns (60 nm, black).

The sizes 60, 75 and 150 nm are the widths of the EBL pattern. The real size of the span will be biased because of the finite beam size and secondary electron exposure, and it appears to be 25-30 nm wider than the pattern size. Therefore, these bridges are actually 90, 105 and 180 nm wide. It was found that 90 nm ones tend to bend and fall on one side, presumably due to the liquid tension forces during the drying procedure and generally are not reproducible. This lack of reproducibility

comes from a difference in the PMMA coating and EBL stability, giving a dose variation sufficiently large to miss the plateau in Fig.5.7. Therefore, the smallest span width selected for fabrication of the samples was 105 nm.

The final resist configuration used for experimental samples was the following: 70-200 nm of PMMA 950K (in anisole), 450 nm of copolymer P(MMA-MAA) 1.6 (in MIBK) and top 75 nm of PMMA 120K (in MIBK) as the imaging layer. This triple layer was developed in IPA:MIBK:EMK (30:10:1) solution for 20 seconds in an ultrasound bath. The latter was important for a good washing of the developed trench in the resist, since the aspect ratio width/height for this trench is $\sim$1/6 (assuming 100 nm bridge width and 600 nm total resist thickness).

5.5 Way forward

In order to further improve the dose contrast $d_t/d_{b'}$ needed for the separate layer development, we have employed a technique wherein a thin gold layer is placed between the soft and hard PMMA layers. This gold film reduces the transmission of electrons, resulting in a smaller dose gained by the bottom layer. The region of 'good' doses (the width of the plateaus in Fig.5.7) will then expand, depending on the thickness of the gold. During development this extra layer can be selectively etched using liquid I/KI aqueous gold etcher.

We have fabricated metal bridges using the explained technique with a 30 nm gold interlayer. To avoid three separate steps in development, one mixed developer was used made of I/KI aqueous gold etcher and IPA with 6:4 water:IPA ratio [65]. Adding isopropanol to an aqueous solution makes the mixture and PMMA surface wettable and therefore the solution can reach the bottom of narrow PMMA profile.

It was found that, indeed, the dose layer contrast is improved and precise dose control becomes less important for the bridges wider than 150-200 nm. However 150 nm was the width limit and all the bridges narrower than that came off in lift-off. Later tests indicate that intermediate gold layer was not etched completely and bridge span was linked with it. Increasing the gold etching time and rate did not help to overcome the size limitation, so this technique is only good for the wide bridges.

To obtain narrow gates and approach the mean free path size a different method

of fabrication can be used. Following the same idea of suspension, a carbon nanotube seems to be a good candidate for a span region due to its unique mechanical properties: high stiffness, small diameter and big length. Because most single wall carbon nanotubes (SWCN) are semiconductors, and therefore useless as a gate, small diameter multiwall carbon nanotubes (MWCN) were selected for this application. Most of them are metallic and therefore will be at an equipotential along their length when a gate voltage is applied with respect to the flake.

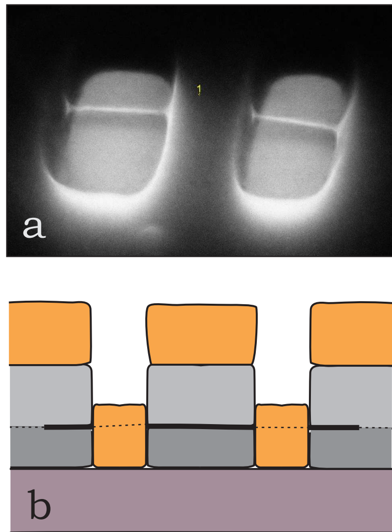

Figure 5.8: Nanotube suspension: a nanotube embedded into resist (a), illustration for metal clamping (b).

In order to make a suspended nanotube, a powder nanotube material with average diameter 15 nm and length 5 μm was diluted in ethanol by ultrasonic treatment. The nanotubes were then deposited from the solution onto a resist-coated wafer. Single nanotubes as well as bunches of twisted nanotubes can be found on the surface using SEM or AFM after drying. A second layer of resist is then spun onto the surface, gripping the nanotubes in place. Two EBL windows in the resist, open over such an embedded nanotube, are shown in Fig.5.8a. The surface is tilted so that one can see a suspended nanotube where PMMA is removed, held by the rest of resist. The metal, evaporated on top of this structure with a thickness larger than that of the bottom resist layer, will clamp the nanotube as shown in Fig.5.8b. Two resist layers are shown as dark and light gray colour blocks, the metal is yellow and the nanotube is the thick black line. Finally, lift-off will remove the resist and excess metal, leaving a suspended nanotube clamped between two metal pillars.

In order to use this nanotube as a gate, it should be placed across a graphene flake with contacts. This stage can be done using micromanipulation with an AFM tip. During our preliminary test it was found that the PMMA surface is too soft for the manipulations and needs to be coated with a thin film of a firm material to make controllable movements possible. The TAFM image in Fig.5.9a shows a graphene device with four contacts. It is covered with a 50 nm thick PMMA layer and 20 nm

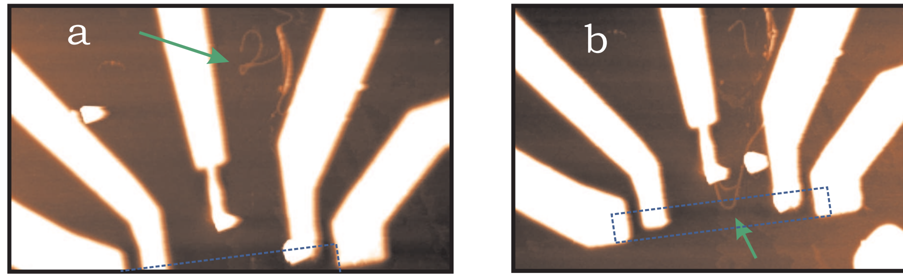

Figure 5.9: MWCN manipulation on a graphene sample. Initial (a) and final (b) positions of the nanotube (highlighted with the green arrow) imaged with TAFM.

thick gold film so that a thin flake is not visible under the coating, but its edges are marked as a blue dotted line. On the first image one can also see a curved MWCN highlighted by a green arrow. Using a series of consecutive pushes, it was moved on top of the flake, close to a specially prepared fifth ‘gate contact’.

Although we have not launched the fabrication of the nanotube-gated samples yet, the preliminary tests done by the author shows promising results and relatively low time consumption for the realization of ‘carbon-carbon’ transistor structures.

5.6 Conclusion

I have created metal air bridges with specific sizes down to 100 nm wide and 3 μm long. The clearance of the bridge can be tuned by varying the thickness of the bottom resist. These bridges were precisely positioned (accuracy 50 nm) over narrow graphene flakes together with the usual metallic contacts. The bridges are mechanically stable and can be used for top gates, allowing for the gate voltages to be of up to 50 V.

The multilayer resist techniques we employed were improved by putting an extra metal layer between the two PMMA layers. However this modification was found to only be useful for the ‘wide’ bridges > 150 nm.

The possibility of creating a suspended nanotube gate was studied. Preliminary results show that it is realizable and requires further time investment.

Chapter 6

Transport in top-gated structures

6.1 Transmission through a single p-n junction

The first theoretical paper published on graphene p-n junctions [100] was dedicated to a p-n-p structure with infinitely sharp p-n and n-p interfaces. The authors built an analogy of the so-called Klein paradox in particle physics for the massless fermions in graphene. Matching the solution of the Dirac equation on different sides of the junctions, the authors of [100] derived an analytical expression for the transmission coefficient through the p-n-p structure.

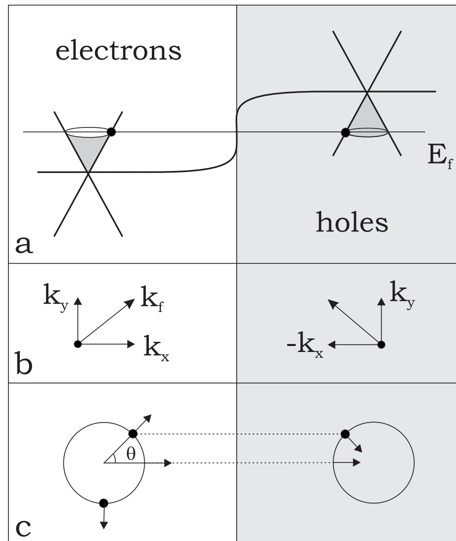

Figure 6.1: Illustration of chiral tunneling through a sharp p-n junction (see text).

The transmission was found to be highly anisotropic, with perfect transmission of electrons impinging on the junction at normal incidence. Remarkably, such behaviour is unique to graphene, and does not occur in bilayer graphene or conventional 2DEGs.

This "chiral tunneling" of the massless fermions in graphene can be explained using conservation of isospin. Let us consider an electron approaching a p-n interface from the left with an angle of incidence θ. It can be imagined in the k-space as a point on a circle of constant energy $E_F = const$, with wavevec-

tor components $k_y = k_{\mathrm{F}} \sin\theta$ and $k_x = k_{\mathrm{F}} \cos\theta$. This electron tunnels through the interface and emerges on the right hand side as a hole (Fig.6.1a). To maintain the current flow, this hole appears with an opposite projection $k'_x = -k_x$. The momentum tangential to the interface should be conserved, so $k'_y = k_y$ (Fig.6.1b). The isospin for the left region can be represented as a unit vector codirectional to $\vec{k_{\mathrm{F}}}$ and for the right region opposite to $\vec{k_{\mathrm{F}}}$ (Fig.6.1c). Thus, there is only one point where the isospins matches perfectly: $\theta = 0$. For other $\theta \neq 0$ transmission is determined by matching of the isospin states (can be found from the corresponding matrix element) and is given by $\omega(\theta) = \cos^2\theta$ [101].

The electron wavelength λ_{F} in our experiments is usually around a few tens of nanometers, while the size of the locally gated region is larger than 100 nm. This suggests that the p-n and n-p junctions in our case can not be treated as infinitely sharp compared to λ_{F}. The authors in [101] examined the case of a single smooth junction for which $2k_{\mathrm{F}}t > 1$ (where $2t$ is the length of the junction) and derived the transmission probability as follows:

$$\omega(\theta) = e^{-\pi\hbar v_{\mathrm{F}} k_{\mathrm{F}}^2 \sin^2\theta / F}, \tag{6.1}$$

where F/e is the electric field in the junction. This decay of transmission is much stronger than for the case of a sharp interface and can be explained as follows:

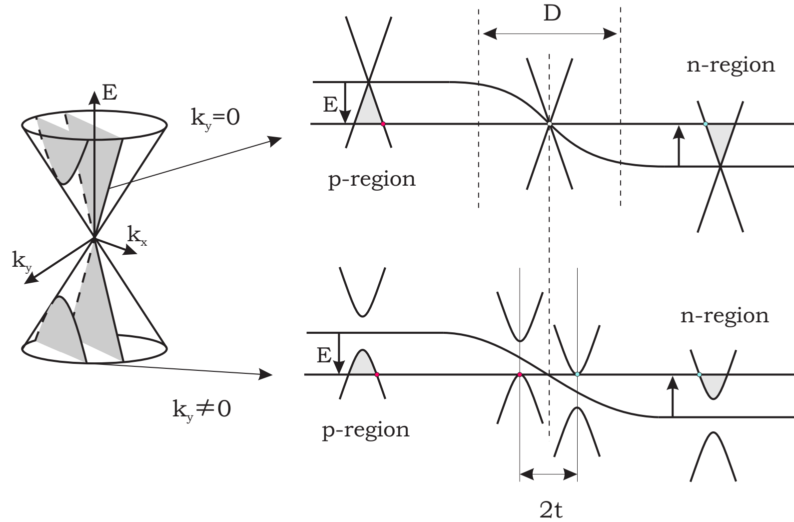

Figure 6.2: Tunneling through a smooth p-n junction.

An electron with nonzero k_y has the kinetic energy $E = \hbar v_{\mathrm{F}} \sqrt{k_x^2 + k_y^2}$. Conservation of the parallel component of momentum k_y leads to the situation when there

is no state available for it in a close proximity to the junction, since it would require having $E < \hbar v_{\mathrm{F}} k_y$. The distance $2t$ is then defined as the classically inaccessible region which requires electrons to tunnel along it. Assuming that the electric field F is linear near the interface, $t = \hbar v_{\mathrm{F}} k_{\mathrm{F}} \sin\theta / F$. Thus, the tunneling probability $\omega(\theta)$ depends exponentially on the tunneling distance and is given by Eq.6.1.

Such a transport gap strongly depends on the incidence angle and vanishes for $\theta = 0$. Moreover, due to the isospin conservation which prohibits backscattering of the chiral particles, normal incidence leads to the perfect transmission of electrons in the absence of isospin flipping mechanisms. The critical angle of transmission can be estimated using Eq.6.1 as

$$\theta_c \simeq (F/\pi\hbar v_{\mathrm{F}} k_{\mathrm{F}}^2)^{1/2}. \tag{6.2}$$

The conductance of a single p-n junction can be derived using the Landauer model as a sum of the current carrying modes [101]:

$$R_{\mathrm{pn}}^{-1} = \frac{4e^2}{h} \sum_n \omega(k_y) \approx \frac{4e^2}{h} \frac{W k_{\mathrm{F}}}{2\pi} \int_{-\pi/2}^{\pi/2} \omega(\theta) \cos\theta d\theta = \frac{2e^2}{\pi h} W \sqrt{\frac{F}{\hbar v_{\mathrm{F}}}}. \tag{6.3}$$

For the correct estimation of the resistance of a p-n junction one needs to know the value of the electric field F. In order to find it, the authors in [102] calculated the charge density profile across a graphene p-n junction induced by a half-infinite top gate. They have demonstrated that the electric field F at the p-n boundary is significantly larger than in the rest of the barrier due to the lack of charge screening at low densities, compared to the naive estimation $F = \hbar v_{\mathrm{F}} k_{\mathrm{F}}/D$ where D is the geometrical size of the locally gated region (shown in Fig.6.2). The method of calculation used in our work considers the realistic potential profile over the junction and gives a value of F in agreement with [102].

6.2 Characteristic lengths of a p-n-p structure, effects of disorder

Transport in real graphene p-n junctions can be significantly affected by disorder. Let us consider a top-gated graphene structure with a gate voltage applied such that a p-n-p (or n-p-n) configuration is achieved. There are several characteristic lengths which are important here: the mean free path of charge carriers l, electron wavelength λ_F, size of a single p-n junction l_{pn} and the size of the region with inverse concentration l_{pnp}. As will be demonstrated later, in our structures $\lambda_F < l_{pn}$ and therefore we treat our p-n junctions as smooth.

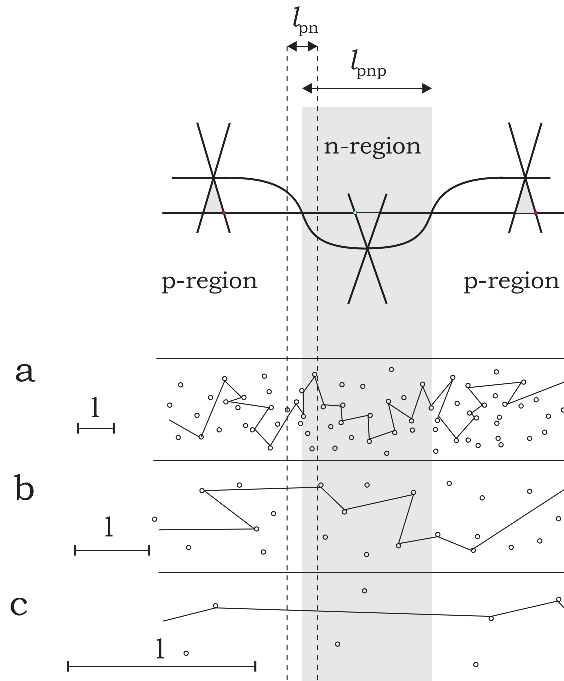

Figure 6.3: Illustration for different transport regimes inside p-n-p structure: from (a) fully diffusive to (c) fully ballistic.

There are three different transport regimes which can be realized experimentally:

1. $l \leq l_{pn}$: in a highly disordered system the transport is purely diffusive [103]. This regime (referred to as diffusive) is illustrated in a naive picture in Fig.6.3a where a semiclassical trajectory shows scattering of a quasiparticle through a p-n-p structure.

2. $l_{pn} < l < l_{pnp}$: in this regime transport through a single junction is ballistic, i.e. there is an extra resistance associated with each p-n junction from Eq.6.3. Since the two junctions are separated by a diffusive region, they can be treated as

independent and the total resistance is $R = R_{\rm diff} + 2R_{\rm pn}$.

3. $l > l_{\rm pnp}$: in this regime the carriers that pass through the first junction have a high chance of reaching the second without being scattered. For ideally parallel boundaries, carriers with $\theta = 0$ will transmit through the whole structure while ones with the large θ will be 'filtered' by the first junction. Therefore the total resistance of this structure should be smaller than $2R_{\rm pn}$ and determined by a transmission probability ω squared (Eq.6.1). However due to the large-scale disorder (i.e. charge inhomogeneity 'puddles') and the high angle-selectivity of the transmission, this regime is most likely disturbed by the two boundaries not being exactly straight and parallel to each other.

The striking difference of the third regime arises for the intermediate values of $0 < \theta < \theta_c$ where the partial transparency of the interfaces leads to multiple scattering events inside the locally gated region. This regime is analogous to Fabry-Perot interference in optics, where a light wave experiences multiple reflections between two semitransparent mirrors.

The phase gained by a quasiparticle bouncing between two p-n interfaces is [104]

$$\Delta\varphi = 2\varphi_{\rm WKB} + \varphi_1 + \varphi_2, \tag{6.4}$$

where $\varphi_{\rm WKB} = (1/\hbar)\int_1^2 p_x(x)dx$ is the semiclassical phase and φ_1, φ_2 are the back-reflection phases. The total transmission through a Fabry-Perot structure $\omega_{\rm pnp}$ is a periodic function of $\Delta\varphi$ [104]:

$$\omega_{\rm pnp} = \frac{\omega_{\rm pn}\omega_{\rm np}}{\left|1 - \sqrt{r_{\rm pn}r_{\rm np}}e^{i\Delta\varphi}\right|^2}, \tag{6.5}$$

where $\omega_{\rm pn}$, $r_{\rm pn}$, $\omega_{\rm np}$, $r_{\rm np}$ are the transmission and reflection coefficients for the first and second interfaces, respectively. The authors in [104] have calculated $\omega_{\rm pnp}$ using a parabolic model $U(x) = ax^2 - \varepsilon$ for the shape of the potential under the top gate. Their results are shown in Fig.6.4. The left part of the figure demonstrates the dependence of $\omega_{\rm pnp}$ on the dimensionless depth of the potential in the middle of the top-gated region $\varepsilon/\varepsilon_\star$ and the transverse momentum $p_y/p_\star$.

Integration over the current carrying modes gives the total conductance and is plotted as the resistance $R/R_\star$ against $\varepsilon/\varepsilon_\star$ on the right of Fig.6.4. The parameters $R_\star, \varepsilon_\star, p_\star$ are geometry dependent and will be calculated in the experimental analysis

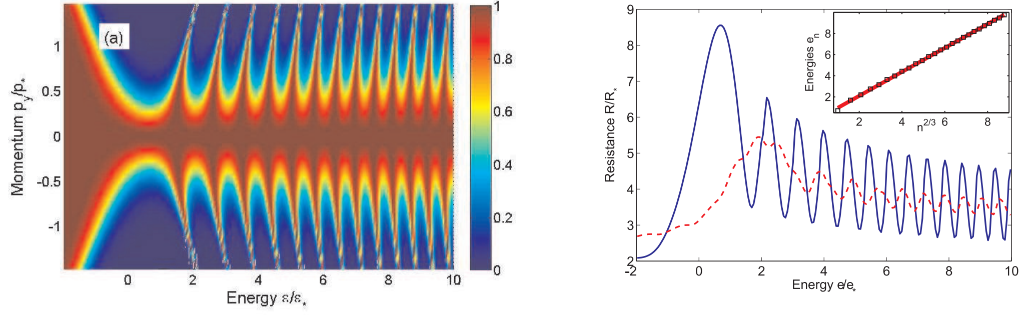

Figure 6.4: Oscillations in (a) transmission coefficient and (b) resistance as a function of the potential depth under the top gate from [104]. Inset shows scaling of the peak positions as a function of $n^{2/3}$, where n is the peak number.

section later.

These calculations predict that the phenomena of multiple reflections in graphene ballistic p-n-p structures can be clearly seen as oscillations of the resistance. These oscillations appear as a function of the top-gate voltage, which tunes the depth of the potential ε and also the size of p-n-p structure, as will be seen from the electrostatic modeling later. The effect of disorder is also studied in [104] and does not destroy the oscillations completely, but results in a decrease of the oscillation amplitude (red dashed line in Fig.6.4).

6.3 Experimental results: overview

The experimental results reported here are based on low-temperature measurements of four top-gated samples. Samples were fabricated and measured by the author except for device S3 which was measured by Alexander Mayorov. (We actually tested more samples and they generally followed the tendency observed in the 4 samples discussed here.) The logic of the experiment was to observe the different regimes of transport described in the previous section by selecting samples with different mobilities and different top gate sizes. The experiments involving samples S1, S2, S3 have been published [94], while the results of the last one, S4, have not.

Prior to the measurements, samples S1,2,3 were annealed at 140° C in helium. All devices exhibit standard behaviour (described in chapter 4) when controlled by the back gate, with a slight offset of the electroneutrality point $V_{\mathrm{bg}}^{\mathrm{off}}$. Fig.6.5a shows sample S2, imaged by SEM, tilted at 45° to the normal so that the gap under the bridge is clearly visible. Lateral sizes of the studied samples were determined by

SEM, sample S1 was also checked with AFM to confirm the monolayer thickness.

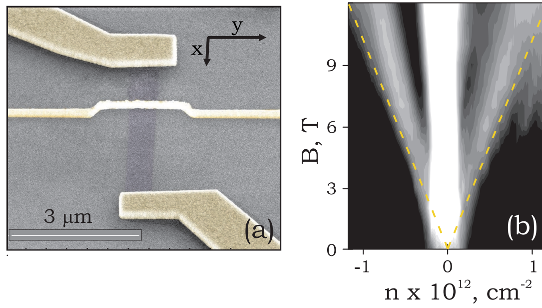

Figure 6.5: Sample S2: (a) SEM image and (b) resistance in high magnetic field (see text)

Transport measurements in high magnetic field also confirm the samples are monolayers, as shown in Fig.6.5b for sample S2. The figure shows a grey-scale of the positions of the maxima in two-terminal resistance as a function of carrier density and magnetic field. They coincide with dotted lines corresponding to the shift of the lowest Landau levels expected for a single layer of graphene (for details see [105]). The geometrical dimensions of our samples are summarized in table 6.1. Sample 4 was not annealed and therefore demonstrates a noticeable initial doping V^{off} and a lower Dirac-point resistance as explained in chapter 3.

Fixing $V_{\mathrm{bg}} = V_{\mathrm{bg}}^{\mathrm{off}}$ will induce the high resistance regime, when the flake as a whole is electroneutral. Applying then a top gate voltage leads to the appearance of a carrier concentration locally near the gate and a drop in the total resistance as shown in Fig.6.6, solid black curve. This happens independently of the sign of V_{tg}, due to the electron-hole symmetry in graphene.

With a finite density of electrons introduced over the whole sample by the back gate, a positive top-gate voltage will add more electrons locally (smaller total resistance) while a negative voltage will deplete electron concentration locally (higher total resistance) and eventually attract holes under the top gate. The change of the polarity of charge occurs near a sharp kink in the resistance, Fig.6.6, coloured lines.

Property	S1	S2	S3	S4
Flake width, W (μm)	0.24	0.6	0.15	0.45
Flake length, L (μm)	5	4.3	1.45	2.7
Top gate length, a (nm)	170	170	110	100
Top gate clearance, h (nm)	140	210	130	75
Top gate thickness, b (nm)	250	250	250	220
Top/bottom gate efficiency	0.35	0.24	0.4	1.05
Intrinsic doping, $V_{\mathrm{bg}}^{\mathrm{off}}$ (V)	0	1.1	1.7	8
Peak resistance, R_{peak} (k$\Omega/\square$)	6.9	4.9	6.3	3.7

Table 6.1: Summary of measured samples.

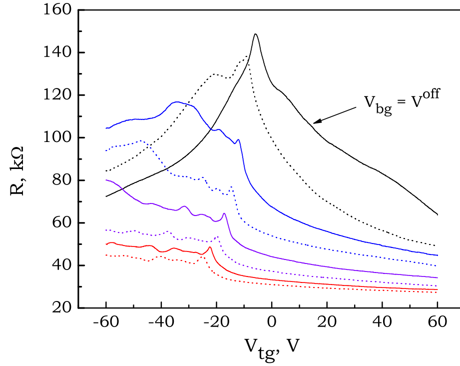

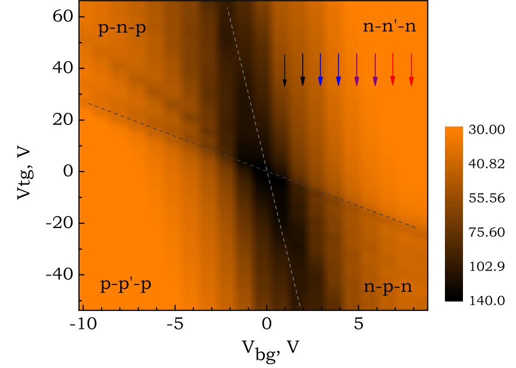

Figure 6.6: Top-gate dependence of the resistance for different values of $V_{\rm bg} = V_{\rm bg}^{\rm off} + i[{\rm V}]$, where i = 1...9, from top to bottom.

Figure 6.7: Colour-scale plot of the resistance as a function of $V_{\rm tg}$ and $V_{\rm bg}$ (sample S1). Coloured arrows refer to the line sweeps in Fig.6.6.

This kink separates $(\rm n-n'-n)$ and $(\rm n-p'-n)$ structures and can be better presented on a colour-scale map, Fig.6.7, where the total resistance is plotted as a function of both $V_{\rm tg}$ and $V_{\rm bg}$. The thick black vertical band indicates the electroneutrality point in the bulk of the flake and the thin inclined line (also highlighted as a dashed line) shows the change of type of carriers under the top gate. These two lines break the colour-scale into four distinct regions: $(\rm n-n'-n)$, $(\rm n-p'-n)$, $(\rm p-p'-p)$ and $(\rm p-n'-p)$. The slope $dV_{\rm bg}/dV_{\rm tg}$ of the steep line gives the efficiency of top gate control with respect to that of the back gate. The efficiency is determined by the top gate clearance and usually is 1 or less in our samples (exact values are given in Table 6.1). The behaviour described here corresponds to sample S1, but is typical for all of our top-gated samples.

6.4 Electrostatic modeling

In order to calculate the flake resistance for any combination of top- and back-gate voltages we have performed electrostatic modeling, taking into account the peculiar graphene DOS. (The main contribution to the development of this method was done by Alexander Mayorov, and his model was used by the author later on.)

The general idea of the calculations is the following. Assuming that the flake is homogeneous and its lateral dimensions are known, we can measure resistivity $\rho(V_{\rm bg})$

and convert it to $\rho(\phi)$, where ϕ is the electric potential. The relation between ϕ and $V_{\rm bg}$ can be found using the capacitance between the flake and back-gate, $\phi = 31\sqrt{V_{\rm bg}({\rm V})}$ [mV]. Calculations of the distribution of the electric potential along the flake $\phi(x)$ with a top-gate voltage applied will allow one to obtain the total resistance from the integral over the sample length L:

$$R_{\rm tot} = \frac{1}{W}\int_{-L/2}^{L/2} \rho(\phi(x))dx \qquad (6.6)$$

for each particular pair $(V_{\rm bg}, V_{\rm tg})$. Since the 'calibration' $\rho(\phi)$ is obtained from the whole flake, this model gives the diffusive resistance $R_{\rm tot}$, without taking the p-n junctions into account.

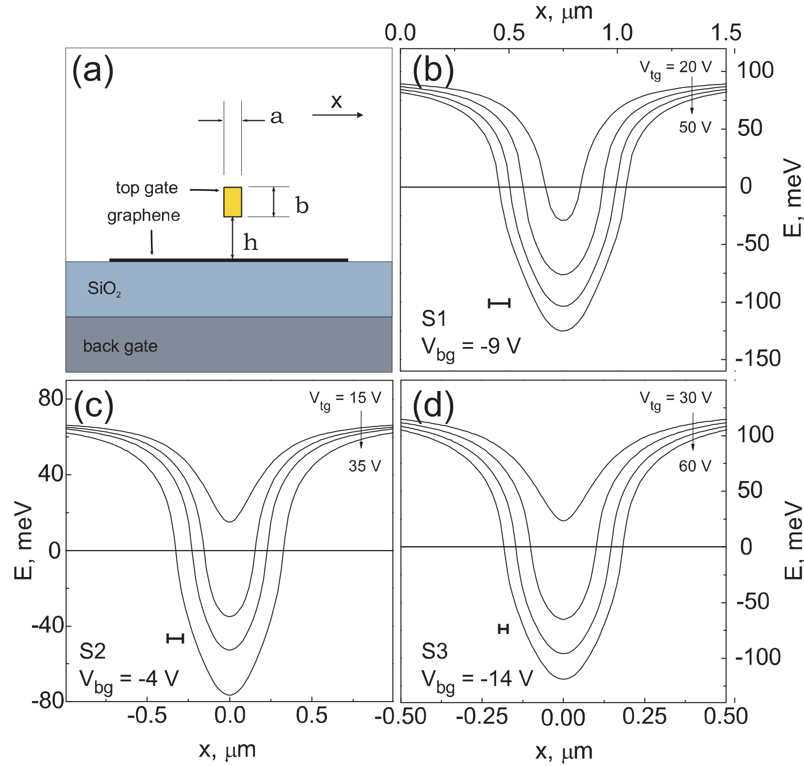

Figure 6.8: Electrostatic modeling reported in [94]: (a) Geometry of top gated structure used in the calculations, (b,c,d) potential profile along the flakes S1,S2,S3 at fixed $V_{\rm bg}$ and different $V_{\rm tg}$. Bold bars indicate the mean free path length.

In order to find $\phi(x)$ we have solved the 2D (x-z) Laplace equation, $\Delta(\phi) = 0$, using a numerical FEMLAB environment. The geometry of the problem is shown in Fig.6.8a, where x is the direction of current flow and z is perpendicular to the flake surface. The cross-section of the suspended gate is shown as a yellow rectangle with sizes a, b, h and the flake as a thick black line.

We have used the constant potentials corresponding to $(V_{\rm bg}, V_{\rm tg})$ as boundary conditions along the gate surfaces. The graphene is modeled as a line with a surface charge density determined by the carrier concentration $\text{sgn}(\phi)n(x)$, which causes the normal component of the displacement field to have a discontinuity on the graphene flake: $\Delta D_n = \text{sgn}(\phi)en(x)$. It is allowed for the surface charge to redistribute itself in a self-consistent way over the flake. The carrier concentration $n(x)$ (at zero temperature) was calculated using the linear density of states in graphene:

$$n(x) = \int_0^{E_{\rm F}} \nu(E)dE = \int_0^{E_{\rm F}} \frac{g_s g_v |E|}{2\pi\hbar^2 v_{\rm F}^2} dE = \frac{e^2\phi^2(x)}{\pi\hbar^2 v_{\rm F}^2}. \tag{6.7}$$

Examples of the calculation of $\phi(x)$ are given in Fig.6.8(b,c,d) for samples S1, S2, S3 according to their real dimensions given in table 6.1. The black lines show the position of the Dirac point counted from the Fermi level taken as $E_{\rm F} = 0$. Here $V_{\rm bg}$ is kept constant and $V_{\rm tg}$ changed in steps (values are given on the images). One can see that, indeed, there is a rapid change of the potential in the vicinity of p-n (n-p) interfaces corresponding to the electric field $F = (0.8 - 2.4) \cdot 10^6$ eV/m, in agreement with theoretical predictions for nonlinear screening [102].

6.5 Diffusive and ballistic regimes of a single p-n interface

The back-gate voltage dependencies for samples S1, S2, S3 are shown in Fig.6.9a. The symbols highlight the values of $V_{\rm bg}$ (bulk concentration $\sim 5 \cdot 10^{11}$ cm^{-2}), which were kept constant during the top-gate voltage sweeps shown in Fig.6.9b,c,d for samples S1, S2 and S3, respectively. Similarly to the dependencies shown before, resistance decreases with adding more holes and increases with depleting the locally gated region. Then the system enters the bipolar mode for high enough $V_{\rm tg}$ and shows reproducible fluctuations of resistance (discussed later) with the average value indicated by the dashed line.

Open circles show the results of the calculations. The only fitting parameter was the distance between the graphene and the metal bridge, h, and it was found that $h = 140$, 210, 130 nm for samples S1, S2 and S3, respectively. The obtained values lie within 10% of those expected from the fabrication process and agree with the

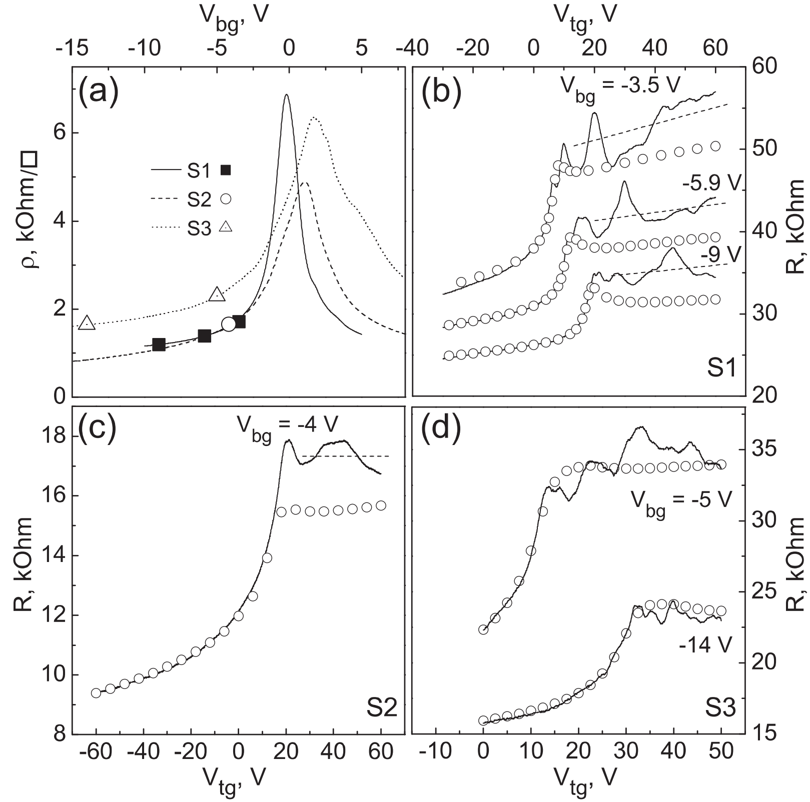

Figure 6.9: (a) Resistivity of samples S1, S2 and S3 as a function of V_{bg}, at $T = 50$ K and $V_{\mathrm{tg}} = 0$. (b,c,d) The resistance of samples S1, S2 and S3, respectively, as a function of V_{tg} (values of V_{bg} shown as symbols in (a)). The empty circles show the result of the modeling assuming diffusive transport of carriers.

observed efficiencies of the top gates (table 6.1).

One can see that before the creation of p-n-p junctions the resistance is well described by the diffusive model for all three samples, Fig.6.9b,c,d. For large values of V_{tg}, in the bipolar regime, samples S1 and S2 demonstrate noticeably larger values of resistance than those expected from the modeling, while sample S3, which has the lowest mobility, shows good agreement over the whole range of V_{tg}, Fig.6.9d.

To explain these observations, we have found the characteristic lengths of p-n junctions and compared them with the mean free path for the three samples. As an estimation for the length of a p-n junction we have used a tunneling distance $2t$ corresponding to twice the critical incidence-angle. The values of θ_c in the three samples varies over the range $20 - 30°$, calculated according to Eq. 6.2, with the electric field F obtained from modeling. The tunneling distance was estimated to be $2t_c \simeq 40$ nm.

The mean free path l has been found using $R(V_{\mathrm{bg}})$ of a uniform sample at $V_{\mathrm{tg}} = 0$, Fig.6.9a, and the relation $\sigma = 2e^2(k_{\mathrm{F}}l)/h$. The value of l weakly depends on the

concentration and can be estimated as $l \simeq 100, 75$ and 45 nm, respectively, for samples S1, S2 and S3. Thus, for samples S1 and S2 l is approximately twice the p-n junction size $2t_c$, while for S3 $l \simeq 2t_c$. This can explain the agreement of $R(V_{\mathrm{tg}})$ with the diffusive model for S3 and suggests the ballistic nature of p-n junctions in S1 and S2.

To clarify the diffusive model mismatch, ΔR, observed for S1 and S2 we have estimated the expected resistance R_{pn} of a ballistic p-n junction. Here we first assume that the p-n interfaces are smooth, $2k_{\mathrm{F}}t \gg 1$, and we use the calculated value of the electric field F for the each particular configuration. The tunneling probability is then calculated according to Eq.6.1 and placed into the equation for the resistance 6.3. We have found that using summation over modes rather than integration is more appropriate in our case, since for instance the narrowest sample S3 has only 3 modes. The value of the Fermi wavevector k_{F} in these calculations is taken at a distance $l/2$ from the p-n interface, where l is the mean free path found above. However, the result is hardly changed if the value of l is varied by two times either way, since it only determines the number of considered modes further away from the transmission threshold $\omega(\theta_c)$. The obtained values are $R_{\mathrm{pn}} = 5$ and 2 kΩ for S1 (at $V_{\mathrm{bg}} = -9$ V, $V_{\mathrm{tg}} = 40$ V) and S2 (at $V_{\mathrm{bg}} = -4$ V, $V_{\mathrm{tg}} = 30$ V), respectively.

The mismatch ΔR^{ex} between the experiment and the diffusive fit can be measured from Fig.6.9(b,c) as 5 and 2 kΩ for S1 and S2, respectively. We believe that this mismatch is due to the ballistic regime in the p-n and n-p junctions, separated by the diffusive n-region. To prove this, we represent this mismatch as $\Delta R = 2(R_{\mathrm{pn}} - R^D_{\mathrm{pn}})$, where R^D_{pn} is the resistance of the diffusive p-n junction of length l. The latter was included into the diffusive model fit and thus has to be subtracted. It can be found as $R^D_{\mathrm{pn}} = 2$ and 0.6 kΩ for S1 and S2, respectively. The estimated values are $\Delta R = 6$ and 2.8 kΩ for S1 and S2 and are close to the experimentally observed ΔR^{ex}. Thus, taking $2R^D_{\mathrm{pn}}$ out from the full diffusive resistance and substituting it with the estimated $2R_{\mathrm{pn}}$ for the ballistic p-n junctions, we eliminate the observed mismatch. This result is in agreement with the ratio of l and $2t$ discussed earlier and therefore proves that p-n junctions in S1 and S2 are ballistic.

Since the Fermi wavelength at a distance $l/2$ from the interface is quite small, $2k_{\mathrm{F}}t \simeq 2$, the applicability of the smooth p-n junction approximation cannot be fully justified for our samples. To examine this problem $\omega(\theta)$ was calculated directly using

numerical methods (by F.Guinea, A.Mayorov, according to [106]) and compared to that from Eq.6.2. The difference in R_{pn} was demonstrated to be less than 5 %, which is beyond our experimental accuracy.

6.6 Fully ballistic regime of the p-n-p structure

The fourth sample S4 had a mean free path ranging from 80 to 140 nm in the used range of V_{tg}, (on average, $\mu = 8000$ cm^{2}V^{-1}s^{-1}). The top gate was placed much closer to the sample, with a clearance of 75 nm and a length in the current direction of 100 nm. The characteristics of this device are given in Table 6.1.

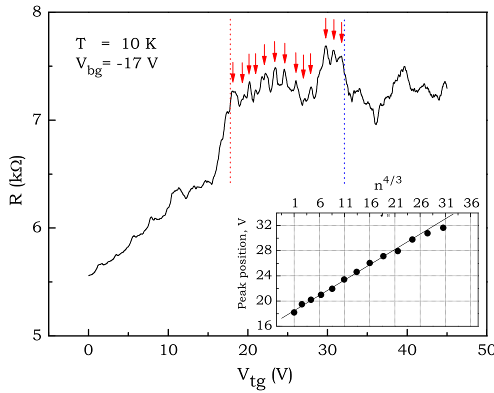

Figure 6.10: Resistance as a function of V_{tg} showing an oscillatory behaviour for a small values of l_{pnp} in the range of V_{tg} between 19 and 32 V.

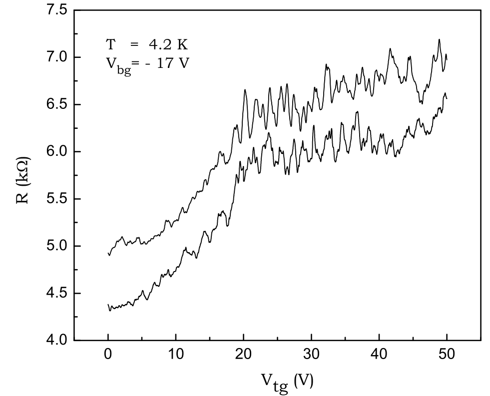

Figure 6.11: The oscillations at 4.2 K: reproducibility test for a different mesoscopic realization, curves shifted by 0.5 kΩ.

Figure 6.10 shows the top-gate voltage dependence for $V_{\mathrm{bg}} = -17$ V (counted from $V_{\mathrm{bg}}^{\mathrm{off}}$). At the onset of the bipolar regime we have observed reproducible oscillations of the resistance, which can be seen at different values of V_{bg}. The red arrows highlight more than 10 oscillations, which are analysed in the inset in Fig.6.10, where the peak positions in V_{tg} are plotted against their numbers n to the power 4/3. The resulting plot exhibits a dependence close to linear, as predicted by [104].

The dependence $R(V_{\mathrm{tg}})$ in Fig.6.10 have been measured at 10 K, while Fig.6.11 represents the oscillations at 4.2 K. Two curves are plotted with a shift of 0.5 kΩ and were measured on different cool-downs (separated by a few-day interval), in order to create a different pattern of the mesoscopic fluctuations. Similar effect can

be produced by sweeping either of the gate voltages up to high values (presumably due to a change in the impurity configuration around graphene). Thus, two curves in Fig.6.12 correspond to different $V_{\rm tg}$ sweeping directions. One can see that the oscillations appear on top of different mesoscopic patterns.

At lower temperatures (Fig.6.11) the oscillations are more pronounced, but there is also a significant contribution of the mesoscopic fluctuations, which makes the oscillations hardly visible at $T \simeq 300$ mK. At high temperatures ~ 20 K the oscillations decay and completely disappear at 30 K as shown in Fig.6.13.

The back-gate voltage values given in the figures are relative to $V_{\rm bg}^{\rm off}$. We have found that the flake is not homogeneous at $V_{\rm tg} = 0$ and therefore the value of $V^{\rm off}$ needs to be determined locally for the region near the top-gate, using a combination of $V_{\rm tg}$ and $V_{\rm bg}$. In order to do this one needs to plot a colour-scale dependence of the resistance on $V_{\rm tg}$, $V_{\rm bg}$ as shown in Fig.6.7 and determine the crossing point $(V_{\rm tg}^{\rm off}, V_{\rm bg}^{\rm off})$ between the four regions. The observed inhomogeneity was probably due to the samples not having been annealed.

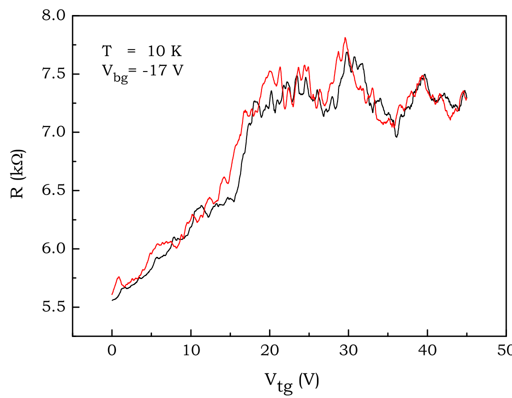

Figure 6.12: Reproducibility test for the dependence shown in Fig.6.10. Black and red curves denote different sweep directions.

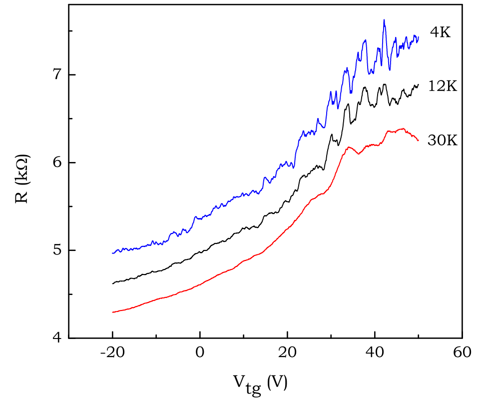

Figure 6.13: Temperature dependence of the oscillations. The curves are shifted by 0.5 kΩ.

As was mentioned earlier, the theoretical paper dedicated to these oscillations [104] is based on the model of the parabolic potential profile under the top gate. In order to justify the use of predictions of [104] we have calculated the potential profile shown in Fig.6.14(a) for the experimental conditions of Fig.6.10. The curves show the potential profile along the flake for each pair of $(V_{\rm tg}, V_{\rm bg})$, with a constant

back-gate $V_{\text{bg}} = -17$ V and $V_{\text{tg}} = (2i + 9)$ V, where $i = 0 \ldots 25$.

Since the oscillations can be seen in a limited range of top-gate voltages, we studied two particular dependencies, shown as red and blue in Fig.6.14. The corresponding values of V_{tg} are shown by the red and blue dashed lines in Fig.6.10 and denote the borders of the oscillation region. The selected dependencies can indeed be neatly approximated using the parabolic function: $U(x) = ax^2 - \varepsilon$, with the results shown in Fig.6.10(c). Careful study of the potential depth ε and the length of the middle p region l_{npn} as a function of V_{tg} reveals that they both almost exactly follow the square root dependence. The latter is illustrated in Fig.6.10(b), where the open circles show the values of l_{npn} (left axis), the filled circles show ε (right axis) and the green lines are square root fits. According to the fit, the potential depth is then given by

$$\varepsilon(V_{\text{tg}})\ [\text{meV}] = 29\sqrt{V_{\text{tg}}\ [\text{V}] - 18.5}. \tag{6.8}$$

This equation resembles the one for the back-gate:

$$\varepsilon(V_{\text{bg}})\ [\text{meV}] = 31\sqrt{V_{\text{bg}}\ [\text{V}] - V^{\text{off}}} \tag{6.9}$$

and confirms the efficiency of 1 for this gate geometry.

At high enough V_{tg} the oscillations disappear since the middle region extends and eventually becomes diffusive when $l_{\text{npn}} \gg l$. The value of l_{npn} corresponding to the experimentally observed vanishing of the oscillations at $V_{\text{tg}} \simeq 31$ V determined from our modeling is $l_{\text{npn}} \simeq 230$ nm. This can be understood assuming an exponential decay of the oscillation amplitude, with the characteristic length close to the mean free path $l \simeq 110$ nm.

Now we turn to the direct comparison of our results and theoretical expectations. The authors in [104] have expressed their results using dimensionless values $\varepsilon/\varepsilon^\star$, $R/R^\star$, $k_y/k^\star$ with $\varepsilon^\star$, $R^\star$, $k^\star$ calculated using only one parameter: the parabolic coefficient a of the potential profile. This coefficient obtained from our modeling equals 10, with a slight variation of 10% over our range of V_{tg}. The resulting coefficients are:

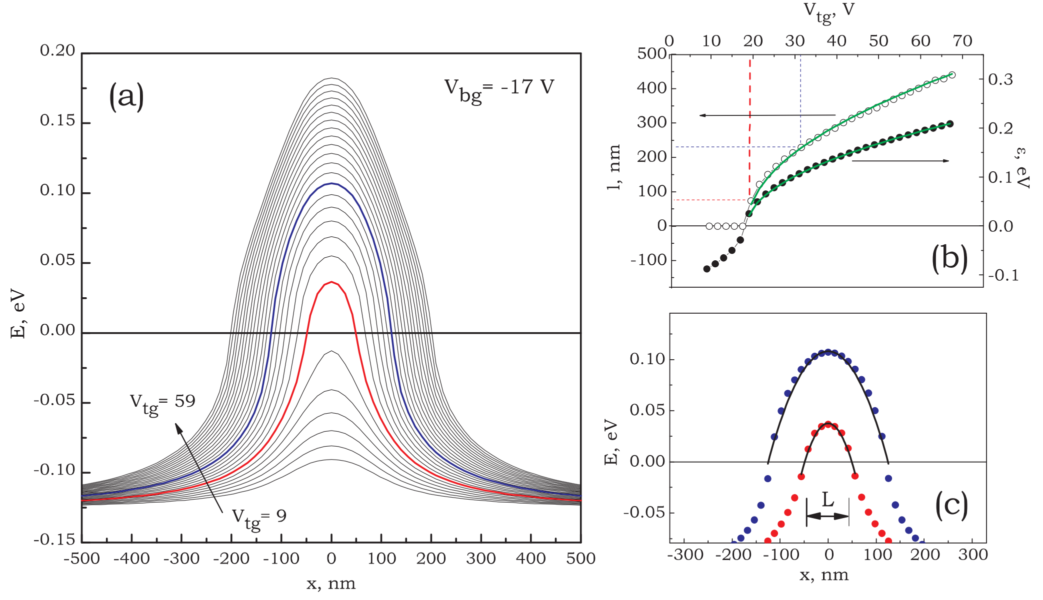

Figure 6.14: Results of electrostatic modeling for sample S4: (a) potential profile along the flake calculated for different top-gate voltages; (b) dependence of $l_{\rm pnp}$ and the potential depth ε on the top-gate voltage; (c) the parabolic fit for the potential shape (see text).

$$\varepsilon_\star \simeq 17.6\,\mathrm{meV}, \quad k_\star \simeq 2.7 \cdot 10^7\,\mathrm{m}^{-1}, \quad R_\star \simeq 0.54\,\mathrm{k}\Omega, \quad B_\star \simeq 0.38\,\mathrm{T}. \qquad (6.10)$$

According to Fig.6.4 the range of k_y contributing to the oscillations is quite narrow: $(1 \pm 0.5)k_\star$. With the size of quantization $\Delta k_y \simeq 0.6 \cdot 10^7$ m^{-1} there are only 3-4 modes participating in the multiple reflection process in sample S4.

We have measured the positions of the peaks in $V_{\rm tg}^n$ and converted them to the energy ε^n using Eq.6.8. We plot our results (black dots) in a similar manner along with the predicted values (red dots and the line, [104]) - as $\varepsilon^n/\varepsilon^\star$ against the peak number $n^{2/3}$, Fig.6.15. For the fitting we use only one parameter – the threshold of the p-n-p regime – and the plotted values correspond to $V_{\rm tg}^{\rm off} = 18.37$ V. The same values (within 1 V) can be obtained from the resistance in Fig.6.10 and the modeling results in Fig.6.14(b).

We see a good matching of the experimental results with the discussed theory for the peak positions. Another quantity we have to compare is the amplitude of the oscillations, which is predicted to be $\sim (2-3) \cdot R_\star$. As one can see from the experimental dependence Fig.6.11 for T=4.2 K the amplitude of the oscillations is $\sim R_\star$ and is at least twice smaller than expected. This can be explained by the

presence of disorder.

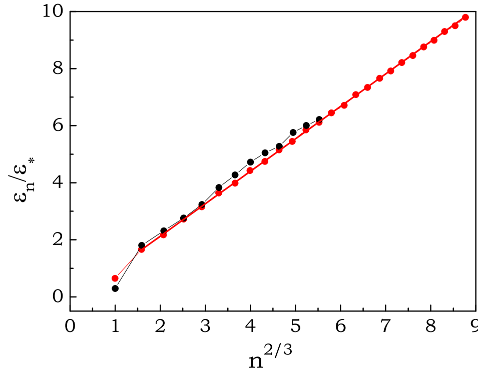

Figure 6.15: Comparison of the observed peak positions (black dots) with the theoretically predicted values (red dots and line) [104].

There are at least three mechanisms which can be responsible for this. Firstly, as discussed in [104], the large scale potential fluctuations seen in graphene [12] can significantly suppress the oscillations down to values below $R_\star$. Secondly, edge effects [6] for the 500 nm wide flake can decrease the effective width of the region contributing to the oscillations. And, lastly, the presence of scattering centers inside the middle region will also cause a decrease in the amplitude. A combination of these mechanisms is also responsible for the fact that at some V_{bg} we see only few oscillations, or a superposition of a few sets with slightly different periods and smaller amplitudes (e.g. Fig.6.13).

6.7 Transport through p-n-p structure in magnetic field

The magnetoresistance predicted for the ballistic p-n-p regime is yet another signature of Fabry-Perot interference. Because the magnetic field changes the shape of electron trajectories and their back-reflection phases φ_1, φ_2, the total phase gained by a quasiparticle bouncing between p-n interfaces will be magnetic field dependent. As was shown in [104], the oscillations in a small increasing magnetic field ($B \sim B_\star$) should gradually drift in the positive direction of V_{tg}, reaching a half-period shift at $B \sim 0.5B_\star = 200$ mT. (This estimation was made for a p-n-p structure without edges, and may look different in a narrow sample. Due to the classical Hall effect there is an electric field perpendicular to the current direction, which can change the physical picture used in [104].) Regardless of that, we have measured the magnetic field dependencies presented below.

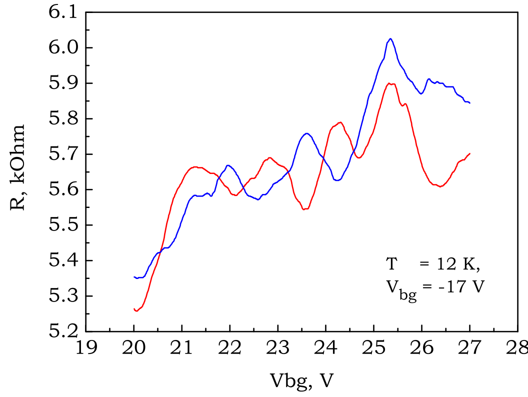

Figure 6.16: Shift of the oscillations in magnetic field: red curve $B = 0$, blue $B = 300$ mT.

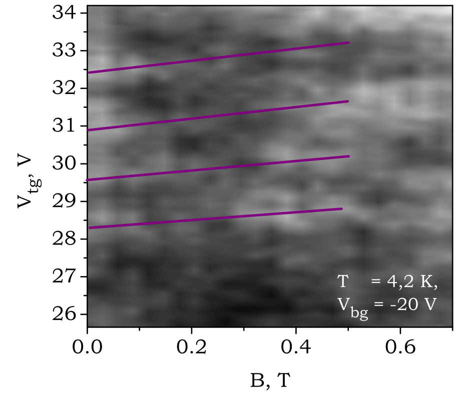

Figure 6.17: Grey-scale plot of resistance as a function of V_{tg} and B showing a shift of the oscillations.

A few oscillations measured (for the same back gate voltage $V_{bg} = -17$ V) in zero magnetic field (black) and $B \simeq 300$ mT (red) are shown in Fig.6.16. One can see the half-period shift of the oscillations occurs at ∼1.5 times higher magnetic field compared to the predicted value. Figure 6.17 is a grey-scale plot of the resistance as a function of both the top-gate voltage and magnetic field at $V_{bg} = -17$ V. One can see that the corresponding shift is seen again at a higher field of $\sim 300 - 400$ mT.

It was found that at lower temperatures it is difficult to measure this effect due to the mesoscopic fluctuations, which are changing at a characteristic field ~ 100 mT and often make the shift of the oscillations not obvious. Another problem occurs when the top gate voltage is swept over a large range (more than 10 V), as this can cause a hysteresis that exceeds the shift we are trying to detect. The reported experimental observations of the shift are the best we have so far and the effect may require further investigation.

We have also studied the magnetoresistance over a larger range of the magnetic field. Figure 6.18 presents $R(B)$ up to 1.5 T for three different distributions of the flake potential. The black circles are the magnetoresistance in the region of V_{tg} prior to the formation of a p-n-p junction, i.e. the carriers are holes with a inhomogeneous distribution along the flake. The red circles plot the magnetoresistance over the region of V_{tg} where a ballistic p-n-p junction is formed, $l_{pnp} < l$. The blue circles are for $l_{pnp} > 2l$, where the two p-n, n-p interfaces can be treated as independent.

The average magnetoresistance in a small magnetic field is determined by the weak localisation effect. We have applied a fitting procedure explained in [74] to show a qualitative agreement with the WL theory for graphene [16]. The fits are valid for $B \leq 100$ nm and are shown in Fig.6.18 as solid lines (for the fit details see Chapter 4). Although the potential profile is not taken into account, the extracted values of the dephasing length L_ϕ are close to those seen in the narrow samples [74] and lie within $\sim 0.4 - 1.5$ μm.

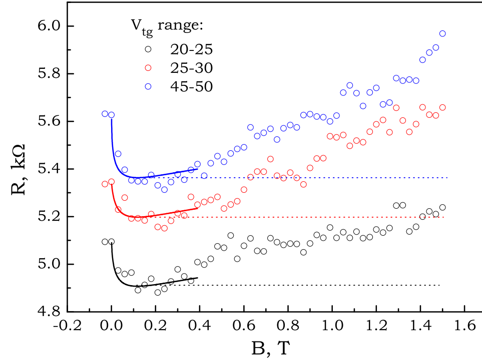

Figure 6.18: Magnetoresistance up to 1.5 T for three different regions on the R(V_{tg}). Solid lines are the weak localisation fits.

The magnetic field dependence in the intermediate field region, before the formation of the Shubnikov-de Haas oscillations at $B \sim 2$ T, can be influenced by two positive contributions. The first arises for a geometrical reason, due to the fact that the sample has a rectangular shape. Its contribution to the resistivity for a uniform concentration is

$$\frac{\Delta\rho}{\rho} = g(\mu B)^2, \tag{6.11}$$

where the coefficient $g = 0.1$ is determined by the length and width of the flake and $\mu \simeq 8000$ cm^2/Vs is the mobility.

Another contribution to the magnetoresistance predicted in the bipolar regime arises due to the change in the tunneling probability through a single p-n interface ω_{pn} in magnetic field. The conductance of a single p-n junction is given as [107]

$$G(B < B_{\star\star}) = G(0)\left(1 - \frac{B^2}{B_{\star\star}^2}\right)^{3/4}, \tag{6.12}$$

where G(0) is the conductance of a p-n junction in the absence of magnetic field and the factor $B_{\star\star} \simeq 3$ T for this sample.

The estimation for $R_{\rm pn}$ using the methods explained in the previous paragraph gives 1 kΩ. At a magnetic field of 1.5 T the second contribution is 20% of $R_{\rm pn}$ and for the full p-n-p structure reaches ~ 400 Ω. However the positive magnetoresistance

observed experimentally ($\sim 500\ \Omega$) is a superposition of the two. Exact separation of them is complicated and requires calculations of the geometrical term in the bipolar regime, which have not been done in the scope of this work.

6.8 Conclusion

We have performed an experimental study of top-gated graphene devices. Using different combinations of the top gate size and mean free path of carriers we have realized experimentally three distinct regimes of transport: fully diffusive ($l < l_{\mathrm{pn}}$), partially ballistic ($l_{\mathrm{pn}} < l < l_{\mathrm{pnp}}$) and fully ballistic ($l > l_{\mathrm{pnp}}$). For the second and third regime, we have observed an increase of the resistance compared to diffusive modeling we did. This increase is shown to be due to the formation of ballistic p-n junctions and is in good agreement with the corresponding estimations. In the fully ballistic regime we have observed a Fabry-Perot-like interference effect predicted earlier in [104], and have demonstrated qualitative agreement of our results with those predictions. We have also discussed the magnetic field dependence of the resistance in the field region of 0-2 T.

Chapter 7

Further developments and suggestions

This chapter is a review of several directions which seem to be promising for the future development of graphene transistor structures. Unlike device-specific plans given in previous chapters here I would like to consider graphene technology in general.

While the room temperature mobility of graphene is remarkably high, it is still far from the conventional 2DEG systems below 4 K. In addition, graphene mobility is significantly lower than that of bulk graphite [22], therefore there is still room for improvements. The current limit most likely due to a consequence of the early stages of the technological process (exfoliation and transfer onto a substrate), since it was demonstrated in this thesis that lithography and further processing does not affect sample quality significantly. Therefore, one of the directions for future work is modification of the fabrication process in order to create better quality devices and achieve the ballistic transport regime in graphene.

At the moment, the best way to get a high mobility devices is the suspension of graphene flakes with a subsequent current annealing [23], however due to the low mechanical stability, which leads to a small device success rate, suspension is a difficult and time consuming technique. Instead, changing substrates, using different procedures of the layer splitting and vacuum graphene deposition can be very helpful techniques for understanding of the current limitation of mobility in graphene.

The second major direction in graphene device fabrication is dedicated to the

large scale growth of graphene films using CVD technique. Indeed, Ni which was previously used as a catalyst for CNT growth, was reported to be a good substrate for graphene and few-layer graphite growth [108]. While this method is not self-limiting and results in a polycrystalline graphite film with 5-10 % single layer coverage, recent development by the Texas University group demonstrates a self-limiting CVD process on copper surface. The authors in [109] claim more than 90% graphene coverage and mobility of 4-5$\cdot 10^3$ cm^{-2}/Vs while such a film can cover a few centimeter big substrate. Developing this fabrication method is yet another direction which may help us to achive macroscopic sample sizes and therefore gives less demanding technology of device fabrication.

The last direction I wold like to propose is chemical modification of graphene which leads to the formation of a gap: hydrogenation, oxidation, fluoridation. Since graphene is a zero gap semiconductor, a transistor made of graphene does not demonstrate a significant on/off resistance difference and therefore cannot be used in the same way as conventional semiconductor devices. Recent work done by the Manchester group [110] shows that graphene can be reversibly transformed into a new semiconductor material with a gap called graphane. Such hydrogenation of graphene can be simply done in hydrogen plasma. The fact that graphene's surface can be easily accessed by various chemicals opens many interesting possibilities of changing its transport properties.

Bibliography

[1] D. R. Lide, ed., *Handbook of chemistry and physics* (CRC Press, USA, 1994).

[2] V. P. Gusynin, S. G. Sharapov, J. P. Carbotte, *International Journal of Mod. Phys.* **21**.

[3] J. C. Slonczewski, P. R. Weiss, *Phys. Rev.* **109**, 272 (1958).

[4] G. Giovannetti, P. A. Khomyakov, G. Brocks, P. J. Kelly, J. van den Brink, *Phys. Rev. B* **76**, 073103 (2007).

[5] P. R. Wallace, *Phys. Rev.* **71**, 622 (1947).

[6] A. H. C. Neto, F. Guinea, N. M. R. Peres, K. S. Novoselov, A. K. Geim, *arXiv:0709.1163* .

[7] G. W. Semenoff, *Phys. Rev. Lett.* **53**, 2449 (1984).

[8] Y. A. Sitenko, N. D. Vlasii, *arXiv:0706.2756* .

[9] M. V. Berry, *Proc. Roy. Soc.* p. 45 (1984).

[10] C. Kittel, *Introduction to solid state physics* (John Wiley & Sons, Canada, 1996).

[11] K. S. Novoselov, *et al.*, *Science* **306**, 666 (2004).

[12] J. Martin, *et al.*, *Nature Physics* **4**, 144 (2008).

[13] T. Mueller, F. Xia, M. Freitag, J. Tsang, P. Avouris, *arXiv:0902.1479* .

[14] T. Ando, T. Nakanishi, R. Saito, *J. Phys. Soc. Jpn.* **67**, 2857 (1998).

[15] T. Ando, *J. Phys. Soc. Jpn* **75**, 074716 (2006).

[16] E. McCann, *et al.*, *Phys. Rev. Lett.* **97**, 146805 (2006).

[17] F. V. Tikhonenko, A. A. Kozikov, A. K. Savchenko, R. V. Gorbachev, *arXiv:0903.4489* .

[18] N. H. Shon, T. Ando, *J. Phys. Soc. Jpn.* **67**, 2421 (1998).

[19] T. Stauber, N. M. R. Peres, F. Guinea, *Phys. Rev. B 76* **76**, 205423 (2007).

[20] S. Fratini, F. Guinea, *Phys. Rev. B* **77**, 195415 (2008).

[21] F. Guinea, M. I. Katsnelson, M. A. H. Vozmediano, *Phys. Rev. B* **77**, 075422 (2008).

[22] J. H. Chen, *et al.*, *arXiv:0812.2504* .

[23] K. I. Bolotin, *et al.*, *Solid State Communications* **146**, 351 (2008).

[24] T. M. Mohiuddin, *et al.*, *arXiv:0802.2389* .

[25] O. Leenaerts, B. Partoens, F. M. Peeters, *arXiv:0710.1757* .

[26] T. O. Wehling, M. I. Katsnelson, A. I. Lichtenstein, *Appl. Phys. Lett.* **93**, 202110 (2008).

[27] *IDB Technologies Ltd* (web address: http://www.idbtechnologies.co.uk).

[28] *UniversityWafer* (web address: http://www.universitywafer.com).

[29] E. F. Vansant, P. Voort, K. C. Vrancken, *Characterization and Chemical Modification of the Silica Surface* (Published by Elsevier, 1995).

[30] *article: "Piranha solution", from Wikipedia, the free encyclopedia* (http://en.wikipedia.org/wiki/Piranha_solution).

[31] I. M. P. Aarts, A. C. R. Pipino, J. P. M. Hoefnagels, W. M. M. Kessels, M. C. M. van de Sanden, *Phys. Rev. Lett.* **95**, 166104 (2005).

[32] V. Albert, *et al.*, *Langmuir* **23**, 9699 (2007).

[33] A. S. Fialkov, *Carbon, carbon based intercalated compounds and composites* (Published by Aspect Press, Russia, 1997).

[34] K. S. Novoselov, *et al.*, *Science* **306**, 666 (2004).

[35] Y. Zhang, Y.-W. Tan, H. L. Stormer, P. Kim, *Nature* **438**, 201 (2005).

[36] A. Lakhtakia, *Nanometer structures: theory, modeling, and simulation* (Published by SPIE Press, 2004).

[37] M. Luna, J. Colchero, A. M. Baro, *J. Phys. Chem. B* **103**, 9576 (1999).

[38] D. Feller, K. D. Jordan, *J. Phys. Chem. A* **104**, 9971 (2000).

[39] R. H. Savage, D. L. Schaefer, *J. Appl. Phys.* **27**, 136 (1956).

[40] R. D. Arnell, D. G. Teer, *Nature* **218**, 1155 (1968).

[41] J. K. Lancaster, J. R. Pritchard, *J. Phys. D: Appl. Phys.* **14**, 747 (1981).

[42] M. P. S. a. E. U. Written by Chris Wright .

[43] D. S. L. Abergel, A. Russell, V. I. Fal'ko, *Appl. Phys. Lett.* **91**, 063125 (2007).

[44] P. Blake, *et al.*, *Appl. Phys. Lett.* **91**, 063124 (2007).

[45] P. Nemes-Incze, Z. Osvath, K. Kamaras, L. P. Biro, *CARBON* **46**, 1435 (2008).

[46] K. S. Novoselov, *et al.*, *PNAS* **102**, 10451 (2005).

[47] N. D. Mermin, *Phys. Rev.* **176**, 250 (1968).

[48] A. Fasolino, J. H. Los, M. I. Katsnelson, *Nature Mater.* **6**, 858 (2007).

[49] J. C. Meyer, *et al.*, *Nature* **446**, 60 (2007).

[50] E. Stolyarova, *et al.*, *Proc Natl Acad Sci U S A* **104**.

[51] M. Ishigami, J. H. Chen, W. G. Cullen, M. S. Fuhrer, E. D. Williams, *NanoLetters* **7**, 1643 (2007).

[52] V. Geringer, *et al.*, *Phys. Rev. Lett.* **102**, 076102 (2009).

[53] Z. Cui, *Micro-nanofabrication: Technologies and Applications* (Published by Birkhauser, 2005).

[54] P. R.-C. (Ed.), *Volume 1: Handbook of Microlithography* (SPIE Publications, 1997).

[55] C. Y. C. (Ed.), S. M. S. (Ed.), *VLSI Technology* (Published by Mcgraw-Hill College, 1996).

[56] D. F. Kyser, N. S. Viswanathan, *J. Vac. Sci. & Technol.* **12**, 1305 (1975).

[57] J. N. H. (Ed.), *Handbook of VLSI Microlithography* (Published by William Andrew Inc., 2001).

[58] S. J. Moss, A. L. (Ed.), *Chemistry of the Semiconductor Industry* (Published by Birkhauser, 1987).

[59] J. S. Greeneich, *J. Electrochem. Soc.* **122**, 970 (1975).

[60] M. D. Ferry, *J. Vac. Sci. Tech. B* **14**.

[61] T. Tada, T. Kanayama, *Jpn. J. Appl. Phys.* **34**, 6947 (1995).

[62] H. Hiraoka, *IBM J. Res. Dev.* **21**, 121 (1977).

[63] *MicroChem Corp.,* (web address: http://www.microchem.com/).

[64] B. Maile, *J. Vac. Sci. Tech. B* **11**.

[65] S. Yasin, D. G. Hasko, H. Ahmed, *Microelectronic Engineering* **61**.

[66] P. Blake, *et al.*, *Proceedings of Graphene Week conference (Trieste, Aug 2008)* .

[67] T. Mueller, F. Xia, M. Freitag, J. Tsang, P. Avouris, *arXiv:0902.1479* .

[68] S. J. Sque, R. Jones, P. R. Briddon, *Phys. Stat. Sol. (a)* **204**, 3078 (2007).

[69] X. Liu, J. B. Oostinga, A. F. Morpurgo, L. M. K. Vandersypen, *arXiv:0812.4038* .

[70] J. Moser, A. Barreiro, A. Bachtold, *Appl. Phys. Lett.* **91**, 163513 (2007).

[71] L. Weng, L. Zhang, Y. P. Chen, L. P. Rokhinson, *Appl. Phys. Lett.* **93**, 093107 (2008).

[72] X. Du, I. Skachko, A. Barker, E. Y. Andrei, *Nature Nanotechnology* **3**, 491 (2008).

[73] R. V. Gorbachev, F. V. Tikhonenko, A. S. Mayorov, D. W. Horsell, A. K. Savchenko, *Phys. Rev. Lett.* **98**, 176805 (2007).

[74] F. V. Tikhonenko, D. W. Horsell, R. V. Gorbachev, A. K. Savchenko, *Phys. Rev. Lett.* **100**, 056802 (2008).

[75] R. V. Gorbachev, F. V. Tikhonenko, A. S. Mayorov, D. W. Horsell, A. K. Savchenko, *Physica E* **40**.

[76] K. Kechedzhi, *et al.*, *Phys. Rev. Lett.* **102**, 066801 (2009).

[77] F. V. Tikhonenko, A. A. Kozikov, A. K. Savchenko, R. V. Gorbachev, *arXiv:0903.4489* .

[78] K. S. Novoselov, *et al.*, *Nature Physics* **2**, 177 (2006).

[79] F. Schedin, *et al.*, *Nature Mater.* **6**, 652 (2007).

[80] S. V. Morozov, *et al.*, *Phys. Rev. Lett.* **100**, 016602 (2008).

[81] Y. Zhang, Y.-W. Tan, H. L. Stormer, P. Kim, *Nature* **438**, 201 (2005).

[82] A. K. Geim, K. S. Novoselov, *Nature Materials* **6**, 183 (2007).

[83] E. H. Hwang, S. D. Sarma, *Phys. Rev. B* **79**, 165404 (2009).

[84] W. Xu, F. M. Peeters, T. C. Lu, *Phys. Rev. B* **79**, 073403 (2009).

[85] V. V. Cheianov, V. I. Fal'ko, *Phys. Rev. Lett.* **97**, 226801 (2006).

[86] K. S. Novoselov, *et al.*, *Nature* **438**, 197 (2005).

[87] A. Isihara, L. Smrcka, *J. Phys. C: Solid State Phys* **19**, 6777 (1986).

[88] V. P. Gusynin, S. G. Sharapov, *Phys. Rev. B* **71**, 125124 (2005).

[89] S. V. Morozov, *et al.*, *Phys. Rev. Lett.* **97**, 016801 (2006).

[90] M. C. Lemme, T. J. Echtermeyer, M. Baus, H. Kurz, *IEEE Electron Device Letters* **28**.

[91] B. Huard, *et al.*, *Phys. Rev. Lett.* **98**, 236803 (2007).

[92] J. R. Williams, L. DiCarlo, C. M. Marcus, *Science* **317**, 638 (2007).

[93] B. Ozyilmaz, P. Jarillo-Herrero, D. Efetov, P. Kim, *Appl. Phys. Lett.* **91**, 192107 (2007).

[94] R. V. Gorbachev, A. S. Mayorov, A. K. Savchenko, D. W. Horsell, F. Guinea, *Nano Lett.* **8**, 1995 (2008).

[95] T. Borzenko, C. Gould, G. Schmidt, L. W. Molenkamp, *Appl. Phys. Lett.* **65**, 2326 (1994).

[96] T. Borzenko, C. Gould, G. Schmidt, L. W. Molenkamp, *Microelectronic Engineering* **75**, 210 (2004).

[97] E. Girgis, J. Liu, M. L. Benkhedar, *Appl. Phys. Lett.* **88**, 202103 (2006).

[98] Y. Feng, *et al.*, *J. Vac. Sci. Technol. A* **18**.

[99] M. J. Rooks, C. C. Eugster, J. A. del Alamo, G. L. Snider, E. L. Hu, *J. Vac. Sci. Technol B* **9**.

[100] M. I. Katsnelson, K. S. Novoselov, A. K. Geim, *Nature Phys.* **2**, 620 (2006).

[101] V. Cheianov, V. Fal'ko, *Phys. Rev. B* **74**, 041403 (2006).

[102] L. M. Zhang, M. M. Fogler, *Phys. Rev. Lett.* **100**, 116804 (2008).

[103] M. Fogler, L. Glazman, D. Novikov, B. Shklovskii, *Phys. Rev. B* **77**, 075420 (2008).

[104] A. V. Shytov, M. S. Rudner, L. S. Levitov, *Phys. Rev. Lett.* **101**, 156804 (2008).

[105] J. R. Williams, D. A. Abanin, L. DiCarlo, L. S. Levitov, C. M. Marcus, *arXiv:0810.3397* .

[106] E. Louis, J. A. Verges, F. Guinea, G. Chiappe, *Phys. Rev. B* **75**, 085440 (2007).

[107] A. V. Shytov, N. Gu, L. S. Levitov, *arXiv:0708.3081* .

[108] A. Reina, *et al.*, *Nano Lett.* **9**, 30 (2009).

[109] X. Li, *et al.*, *Science* **324**, 1312 (2009).

[110] D. C. Elias, *et al.*, *Science* **323**, 610 (2009).

Appendix A

Inserts

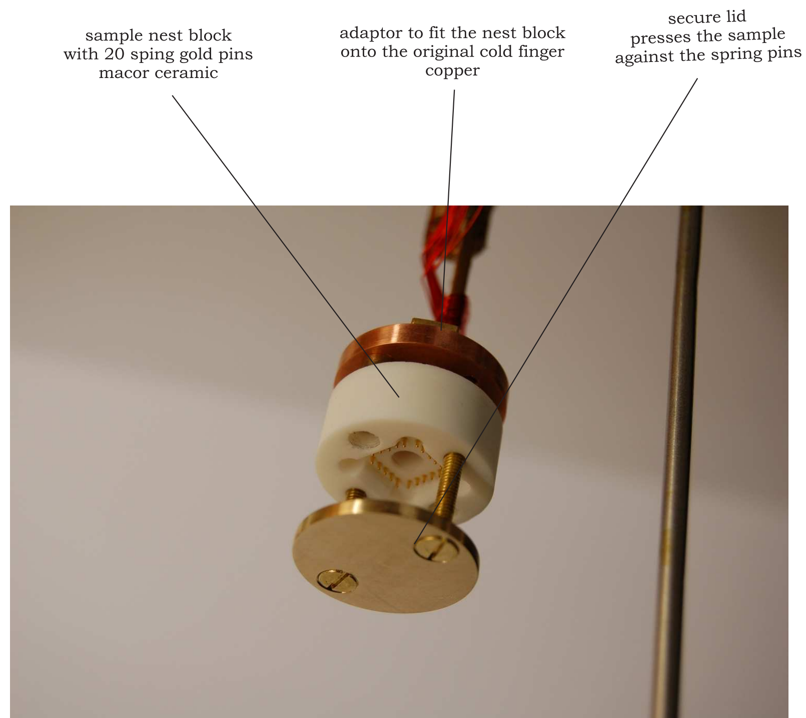

Figure A.1: Modification done to Heliox VL criostat cold-finger. Allows quick and reliable connection of the sample packages to the cryostat wires.

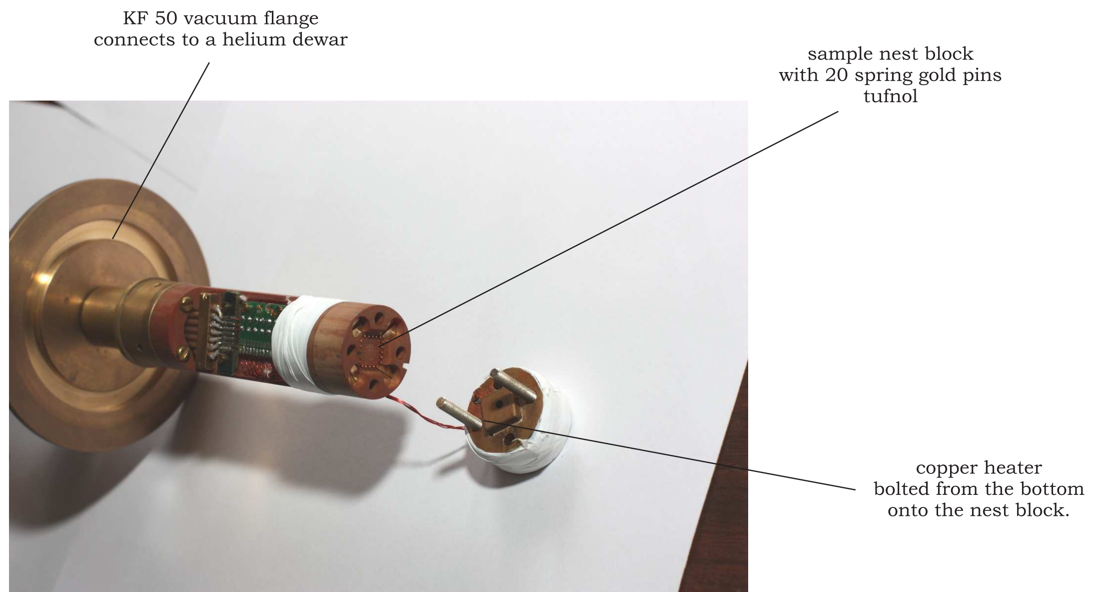

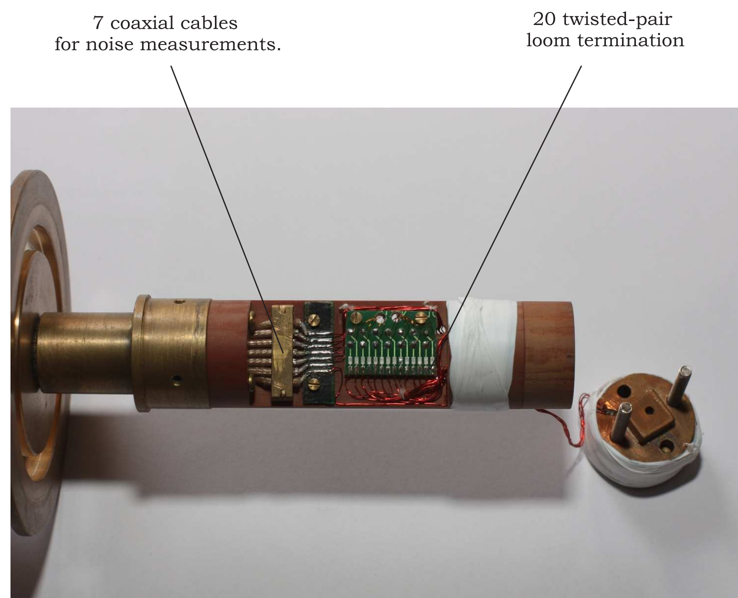

Figure A.2: Low temperature part of the experimental insert used for characterisation study of graphene samples and annealing in a transport dewar.

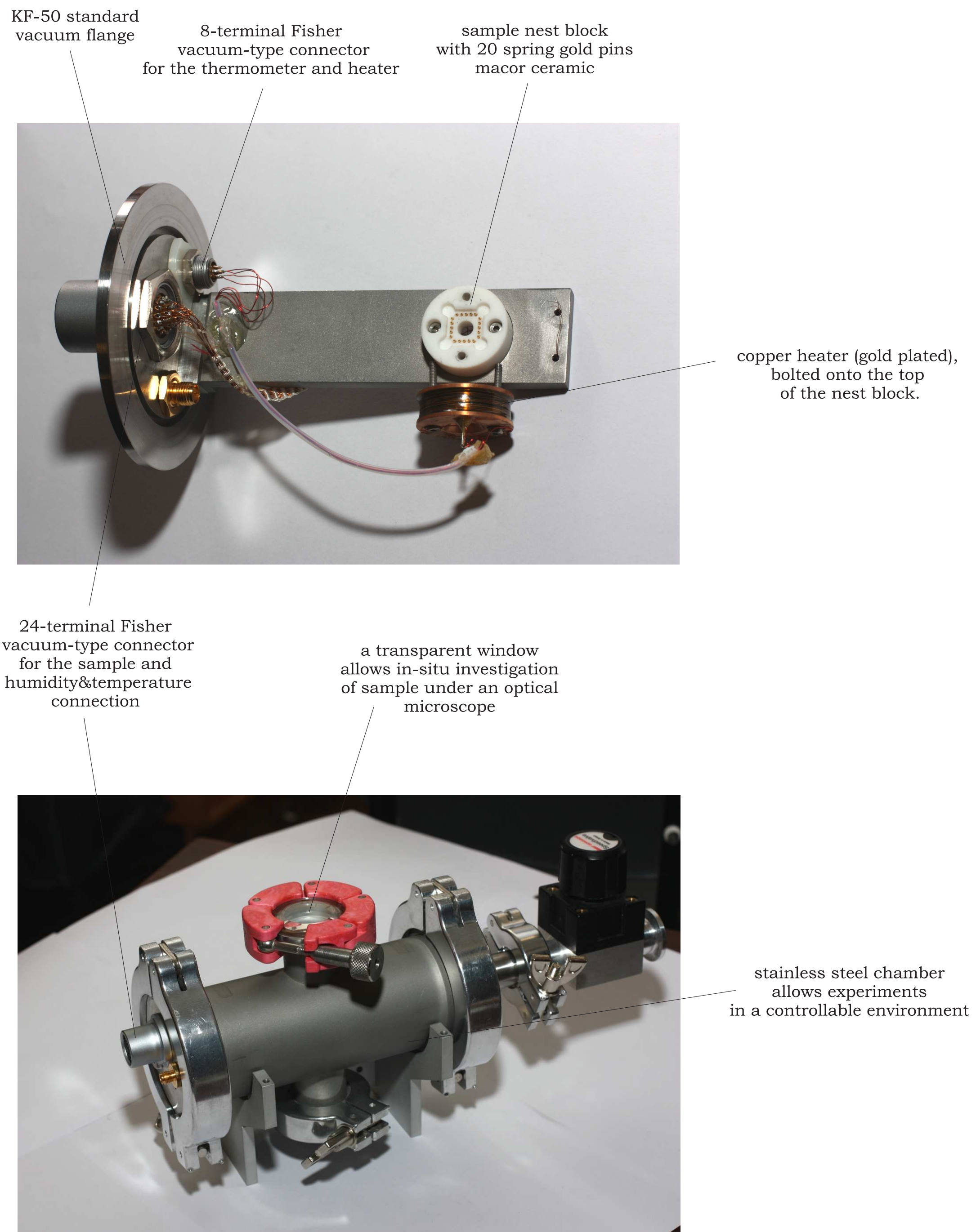

Figure A.3: Environmental chamber for doping experiments. Insert with the sample nest, heater and environmental gauges (top) and a chamber body with transparent optical window, gas inlet and pumping port.